Development and Application of a Time-Of-Flight Mass Spectrometer with a Cryogenic Detector for the Spectrometry of Heavy Biomolecules

Stefan Rutzinger

MAX-PLANCK-GESELLSCHAFT

TECHNISCHE UNIVERSITÄT MÜNCHEN

Max-Planck-Institut
für Physik
(Werner-Heisenberg-Institut)

Development and Application of a Time-Of-Flight Mass Spectrometer with a Cryogenic Detector for the Spectrometry of Heavy Biomolecules

Stefan Rutzinger

Vollständiger Abdruck der von der Fakultät für Physik der Technischen Universität München zur Erlangung des akademischen Grades eines

Doktors der Naturwissenschaften

genehmigten Dissertation.

Vorsitzender: Univ.-Prof. Dr. M. Lindner

Prüfer der Dissertation:

1. Hon.-Prof. Dr. N. Schmitz
2. Univ.-Prof. Dr. L. Oberauer

Die Dissertation wurde am 01.07.2003 bei der Technischen Universität München eingereicht und durch die Fakultät für Physik am 29.09.2003 angenommen.

Übersicht

Die Flugzeit-Massenspektrometrie ist ein wichtiges Analyse-Instrument in der Proteinforschung. Sie wird eingesetzt, um Proteine eines Organismus zu identifizieren, zu quantifizieren und zu analysieren. Weiter findet sie Anwendung in verschiedenen anderen Bereichen, in denen Makromoleküle untersucht werden, wie z.B. der Polymer-Forschung.

Derzeit erhältliche Flugzeit-Massenspektrometer (TOF-MS) sind mit Ionisationsdetektoren ausgestattet. Deren zugänglicher Massenbereich ist nach oben beschränkt, da ihre Ionisationseffizienz mit zunehmender Molekülmasse (sinkende Molekülgeschwindigkeit) abnimmt. Um große Moleküle dennoch messen zu könnnen, müssen diese vor der Messung geeignet zerkleinert (fragmentiert) werden. Das ist nicht immer möglich oder sinnvoll. Deshalb ist eine Erweiterung des Messbereichs zu Massen über mehrere 100.000 Atommassen wünschenswert.

Um die Massenbeschränkung von TOF-MS zu umgehen, kann ein anderer Detektortyp eingesetzt werden. Bolometrische oder kalorimetrische Detektoren registrieren jedes auftreffende Molekül unabhängig von dessen Ionisationswirkung. Als weiteren Vorteil liefern diese Detektoren zusätzliche Energie-Information.

Im Rahmen dieser Arbeit, die angegliedert ist an ein Teilprojekt des deutschen "BMBF Leitprojekt-Verbund Proteom-Analyse des Menschen", wurde ein neuartiger Detektortyp basierend auf supraleitenden Phasenübergangs-Thermometern (SPT) entwickelt. In ihren bisherigen Anwendungen haben diese Detektoren Signale, die für die Verwendung in der Massenspektrometrie zu langsam sind. Ihre Geschwindigkeit ist durch Wärmekapazitäten und interne Ausgleichsvorgänge bestimmt und kann durch geeignete Verkleinerung des Detektors wesentlich verbessert werden. Der Schwerpunkt der Detektorentwicklung lag daher in der Verkürzung der Signal-Anstiegszeit, um eine hohe Zeit- und damit Massenauflösung zu erreichen.

Für den Betrieb des SPT bei Temperaturen um $\sim 100\,\mathrm{mK}$ musste ein modifiziertes MS gebaut werden, an das ein adiabatischer Entmagnetisierungs-Kryostat angeschlossen werden kann. Insbesondere wurde das MS mit einem Stickstoff-gekühlten Ionenreflektor ausgestattet, um die Wärmestrahlungslast auf den Kryodetektor zu minimieren. Der Kryostat besitzt einen Helium-gekühlten Rüssel, über den die Moleküle aus dem angeschlossenen Spektrometer auf den Detektor treffen.

Im Rahmen dieser Arbeit wurden verschiedene Detektor-Geometrien und -Grössen getestet. Hierbei stellte sich heraus, daß für die Zeitauflösung des Detektors die Geometrie von Trägersubstrat und Thermometer-Film gegenüber den absoluten Dimensionen des Detektors eine sehr untergeordnete Rolle spielen: Ein kleines flaches Trägersubstrat mit einem einfachen, eine Fläche des Substrats bedeckenden, Thermometer-Film lieferte die schnellsten Signale. Anders strukturierte Thermometer-Filme wiesen jedoch unwesentlich schlechtere Eigenschaften auf.

Die beste bisher gemessene Zeitauflösung eines Kryodetektors lag bei $\Delta t = 1.1\,\mu\mathrm{s}$ bei einer Signal-Anstiegszeit von $\tau_{rise} = 1.3\,\mu\mathrm{s}$. Dabei war die Zeitauflösung durch ein unerwartet schlechtes Signal-zu-Rausch-Verhältnis beschränkt. In einer Verdünnungsreihe konnte Insulin bei einem Probenvolumen von 1 amol noch sicher nachgewiesen werden. Das schwerste nachgewiesene Protein war Immuno-Globulin G mit einer Massenzahl von ca. 150.000.

Summary

Time-of-flight mass spectrometry is an important instrument for the investigation of proteins. It is used for the identification, quantification and analysis of the proteins of an organism. Furthermore it has its application in several other fields that deal with macro molecules such as the investigation of polymers.

Currently available time-of-flight mass spectrometers (TOF-MS) are supplied with ionisation detectors. Their accessible mass range has an upper limit since the ionisation efficiency decreases with increasing molecule mass (decreasing molecule velocity). To be able to measure high-mass molecules nevertheless, they need to be fragmented (digested). This is not possible or reasonable in every case. Therefore an extension of the mass range of TOF-MS to masses above several 100000 atomic mass units is desirable.

To avoid this limitation of TOF-MS, another type of detector may be used. Bolometers as well as calorimeters detect every molecule hitting the detector independently of the molecule's ionisation behaviour. Additionally these detectors provide extra energy information.

In the current work, which is part of the "German Human Proteome Project", a new type of detector is developed, based on superconducting-phase-transition-thermometers (SPT). In previous applications these detectors have signals which are too slow as to be used in mass spectrometry. Their speed is given by heat capacities and inner relaxation processes and may significantly be improved by making the detectors smaller. Therefore the main focus in the development of the new detectors was a reduction of the signal rise times to achieve a high time- and thus mass resolution.

For the operation of the SPT at temperatures around $\sim 100\,\mathrm{mK}$ a modified MS had to be built which can be connected to an adiabatic demagnetisation refrigerator. In particular, the MS was fitted with an ion reflector which was cooled by liquid nitrogen to minimise the thermal radiation load on the cryogenic detector. The cryostat has a snout cooled by liquid helium, through which the molecules coming from the MS reach the detector.

Within the scope of this work different detector geometries and sizes were tested. Thereby it was found out that in terms of time resolution the geometry of the detector plays a minor roll compared to the absolute dimensions of the detector: a small, flat carrier substrate with a simple SPT-film totally covering one plane of the substrate, showed the fastest rise time. Thermometer films structured differently had marginally worse properties, though.

The best time resolution of a cryogenic detector up to now was $\Delta t = 1.1\,\mu\mathrm{s}$ with a signal rise time of $\tau_{rise} = 1.3\,\mu\mathrm{s}$. Hereby the time resolution was limited by an unexpectedly poor signal-to-noise ratio. The presence of a sample volume of only 1 atomole of insulin could be proven in a dilution test series. The protein with the highest atomic weight detectable up to now was Immuno-globulin G with a mass number of ~ 150000.

Contents

Chapter 1

Introduction

In the year 1990 a project was started to investigate all genes on every chromosome in the human body, the U.S. Human Genome Project [Bro00]. It is an international project with more than 18 countries and many U.S. scientific institutes taking part in it. Initially the project was scheduled to run for 15 years until the full decryption of the human DNA sequence, with many open questions about how to sequence the $30000-35000$ genes in the given time and how to store the huge amount of data. But computation and technology developed even faster than expected, and during the first year of this Ph.D., in 2000, the completion of the first "working draft" of the human DNA sequence was already announced [Pre00] and shortly after published [IHG01]. The fine-sequencing is now expected to be finished in 2003, only 13 years after the start of the project.

Besides and through the nearly finished Human Genome Project the investigation of the human proteome became more and more interesting in medical research. The proteome is the sum of all proteins being active in an organism at a certain time. With the genome being the "program" which controls how an organism is build up, the proteins in this organism are the substances actually reading this program, decoding it, and building up and keeping the organism running. The genome controls how and when certain proteins are built, but the proteins run the organism.

The genome is fixed during the whole life of an organism, but its proteome changes with its development. It changes with age, environmental conditions, nutrition, contact with other life forms like bacteria, and with the health status of the organism. In the huge amount of estimated 300000 proteins in the human body, the major challenge in proteome research is to find out the function of distinct proteins, and to isolate key proteins or protein patterns which are responsible for certain functions or malfunctions of the organism (phenotype).

This protein search is still in a very beginning state. Commercial machines have just become available in the past year, and these devices are still in heavy evolution. Similar to the Human Genome Project, many national and international projects were started for a systematic investigation of the human proteome.

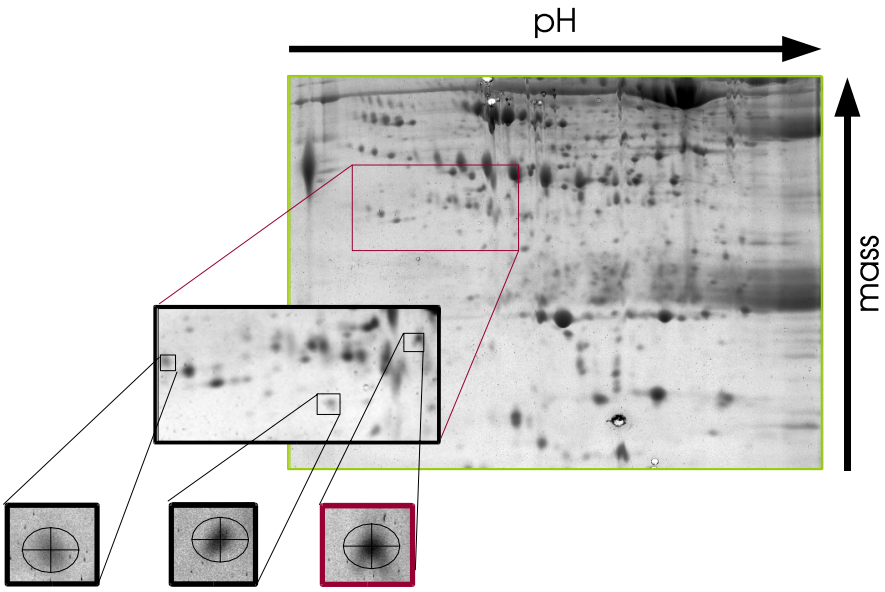

Figure 1.1: Typical 2D-GEL protein pattern. Protein spots of interest are stamped out and further analysed in TOF-MS. The displayed GEL is from human synovial fluid of a patient with rheumatoid arthritis. (pH $4-7$, GEL 12.5% mass, Sypro Ruby stain)

PROTEOM, the "BMBF Leitprojekt zur Proteom-Analyse des Menschen" (The German Human Proteome Project) of the German Federal Ministry of Education and Research, is one of them.

In almost all methods currently used for protein identification mass spectrometry (MS) is involved, since it is easy to separate proteins or their fragments by mass. Yet due to their large number it is impossible to invent chemical detection reactions, e. g. with antibodies, for every protein of interest. Neither would it be possible to apply all these detection reactions to a certain protein in question in finite time.

One investigation method is to combine MS with a preceeding 2D-GEL electrophoresis. In 2D-GEL electrophoresis a sample liquid containing a complex protein mixture, for example taken in-vivo from a living organism, is coarsely arranged to a first protein spectrum. The proteins are sorted on a carrier sheet, in one direction by a pH gradient by their isoelectric point, and in the perpendicular direction by their mass. Certain patterns in the GEL represent the state of certain functional groups in the sample. Spots of special interest in this spectrum can then be picked out and further investigated by MS [Eck97]. Figure 1.1 shows such a 2D-GEL of human synovial fluid as an example. The horizontal axis represents the pH gradient, the vertical axis the protein mass.

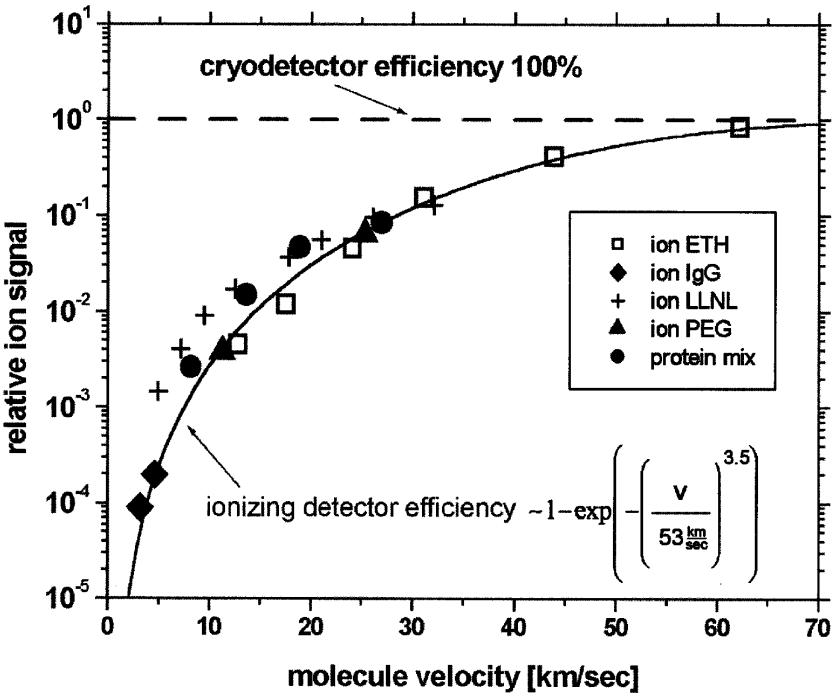

Figure 1.2: Detection efficiency of ionisation detectors (measured: marks, calculated: solid line) and cryogenic detectors (theoretical, dashed line) versus particle velocity. Figure taken from [Twe01].

Several types of mass spectrometers are in use for protein analysis. One frequently used is the Time-Of-Flight Mass Spectrometer (TOF-MS), where the ionised proteins are accelerated in a constant electric field, then fly a fixed distance before their flight time is measured with a detector. Since the ions all acquire the same kinetic energy per charge in the electric field, their velocity and time-of-flight differs according to their mass. State of the art detectors in TOF-MS are usually ionisation detectors, like Micro-Channel-Plates (MCP). They detect charged particles in motion by their capability to induce an initial ionisation in the detector. This requires the particles to hit the detector with a minimum velocity. In a TOF-MS, for particles with higher mass which have lower velocities, the detection efficiency of such ionisation detectors rapidly decreases as shown in figure 1.2.

For their identification in TOF-MS proteins usually are first digested with enzymes to peptides and short amino acid chains of masses of approximately $100-10000$ Dalton (Da, $1\,\mathrm{Da} = 1\,\mathrm{amu}$). They can be detected easily by ionisation detectors if they are accelerated to energies of $10-40\,\mathrm{keV}$. Due to the limitation of the acceleration voltage the limit in detectable mass is at about $100\,\mathrm{kDa}$. The measurement of intact, undigested proteins is only possible for lighter specimens. Currently the accessible mass range of TOF-MS can be enlarged significantly

if another type of ion source is used, the Electro-Spray-Ionisation (ESI) source. Within an ESI source the proband molecules are multiply charged and thus are accelerated to a multiplicity of their usual velocity. Measurement of molecules up to the MDa mass range is possible. The disadvantage of the ESI method is that the charge states of the proband molecules are not well-defined and so an ESI mass spectrum always shows a large diversity of peaks, each belonging to one charge state, and it is not always easy to interpret ESI mass spectra [Fue95].

So the demand for a detector with a detection efficiency independent of the ionisation probability, or the charge of the proband molecule in general, as shown by the dashed line in figure 1.2, is evident. This requirement can be fulfilled by low-temperature calorimetric detectors. The cryogenic calorimeter used in this work consists of an absorber crystal and a superconducting thermometer film. Energy deposited in the absorber crystal by impinging molecules leads to a temperature rise, which is detected by the superconducting phase transition thermometer (SPT). Cryogenic calorimeters are operated at temperatures typically below 150 mK. The low temperatures are necessary to achieve heat capacities low enough so that particles with energies of $10 - 40$ keV produce a measurable temperature rise.

The use of cryogenic detectors for the mass spectrometry of biopolymers was first suggested by D. Twerenbold and demonstrated by his group at Neuchatel University, Switzerland in the year 1996 [Twe96, Twe96a]. Applicability of these cryogenic detectors, which are of a different type (tunnel junctions) than the ones developed in our group, has been proven in the meanwhile [Boo97, Twe01, Ull00, Wes99]. Cryogenic detectors of several types have already been used or suggested for use in biomolecule TOF-MS. Overviews are given in [Fra99] or, more recently, in [Fra00].

Cryogenic calorimeters are used for example for the search for weakly interacting massive particles (WIMPs), e. g. in the CRESST experiment [Sis97, Ang02, Fra94], and others [Nav01, Per01]. They are being developed for the GNO (Gallium Neutrino Observatory) [Alt97] for the search for solar neutrinos, or for X-ray spectroscopy [Ang01, Ben03, Bru00, Por01] . An energy resolution of up to 4.5 eV for 5.89 keV X-ray has been measured [Ber01], and the detection of single optical photons with cryogenic calorimeters has been reported [Cab98].

The time resolution of MCP detectors is in the order of some ns, which allows to resolve fractions of atomic masses, i.e. isotopes. For large mass proteins, such a high time resolution is not required any more. On the one hand molecule flight times t become higher and thus a given detector time resolution Δt leads to a lower relative error $\Delta t/t$. On the other hand for large proteins the natural isotope distribution in the proteins already leads to a mass uncertainty between chemically identical proteins (natural isotope mass-broadening). For example the natural isotope distribution in a 66 kDa molecule will broaden its time-of-flight

distribution to about 130 ns in a typical TOF-MS [Leh96][1].

The massive detectors developed in the same group for the CRESST experiment have a signal rise time (10% → 90% of amplitude) in the order of 1 ms, which is by far too slow for TOF-MS. So the main focus of the detector development of this work was to achieve a sufficiently high time resolution. A time resolution of $\sim 0.1\,\mu$s may be reached with a signal rise time of $1\,\mu$s: Assuming a reasonable signal to noise ratio it should be possible to determine the signal onset time (particle impact time) with a precision of $0.1\,\mu$s. Besides the detector development it was also necessary to set up a special TOF-MS which prevents room temperature thermal radiation from the spectrometer to reach the cryogenic detector. Room temperature thermal radiation would heat up the detector above its operating temperature and introduce unacceptable levels of infrared photon shot noise.

A TOF-MS for measuring masses above 100 kDa is useful for applications other than protein analysis as well. Any type of heavy molecule that can be accelerated to a suitable particle beam is a potential candidate to be measured in this spectrometer. It would as well be of interest to investigate whole functional cell groups, like for example ribosomes.

Another application of TOF-MS is the analysis of polymers. The monomers they are built of are easily accessible with present TOF mass spectrometers. The polymers however may form chains of arbitrary length which may be too heavy to be measured by conventional mass spectrometers. Nevertheless structure and mass analysis of polymers is an important tool in the development of new materials. A TOF-MS with enlarged mass range to above 1 MDa would as well be very useful for these investigations.

[1] As calculated in sec. 3.2.5

Chapter 2

Detector Concept

Time-of-Flight Mass Spectrometers (TOF-MS) consist of three main components: an ion source, a flight-time analyser (flight tube), and a detector to register the arrival time of the molecules. The source in the mass spectrometer used in this work is a Matrix Assisted Laser Desorption/Ionisation (MALDI) source. In a MALDI source the proband molecules, embedded in a light absorbing matrix, are first evaporated and ionised by a pulsed laser beam and then accelerated in an electric field. The accelerated molecules travel through the analyser to convert the initial velocity distribution due to their different masses into a flight time distribution. Finally, the arrival times of the molecules are measured with a time resolving detector.

The goal of this work was to develop a TOF-MS with a new kind of detector which allows to enhance the accessible mass range of MALDI-TOF Mass Spectrometers to masses far above 100 kDa. The new detector is a cryogenic calorimeter and uses a superconducting phase transition thermometer (SPT). It operates in the temperature range around 100 mK. The detector is installed in a cryostat which has a suitable entrance hole to let the sample molecules enter the cryogenic chamber.

In the following section a model describing the signal formation in cryogenic detectors is presented. It includes a discussion of the thermal properties of the components involved. Then a closer discussion of the processes responsible for the time resolution of such devices is given.

2.1 Superconducting Phase Transition Thermometers

Several types of cryogenic particle detectors have been developed in the past years [Boo97, Cab96]. One of them is a cryogenic calorimeter using an SPT to measure the energy deposited in an absorber volume. The full energy is measured irrespectively of the type of interaction, in particular absorption of X-ray or

optical photons, nuclear recoils in the volume, or impact of macroscopic particles on the absorber surface.

Cryogenic calorimeters consist of three main parts as sketched in figure 2.1: An absorber, an SPT film as sensor, and a thermal link to a heat reservoir provided by a cryostat. Typically it is operated at temperatures below 150 mK, to reduce the heat capacity.

In the absorber interactions take place which deposit energy. Absorber material and shape is chosen to optimise the detection of the desired type of events. Besides dielectrics it is as well possible to use superconductors, semiconductors or metals as absorber materials. Metals however have a very high heat capacity due to the contribution of the conduction electrons.

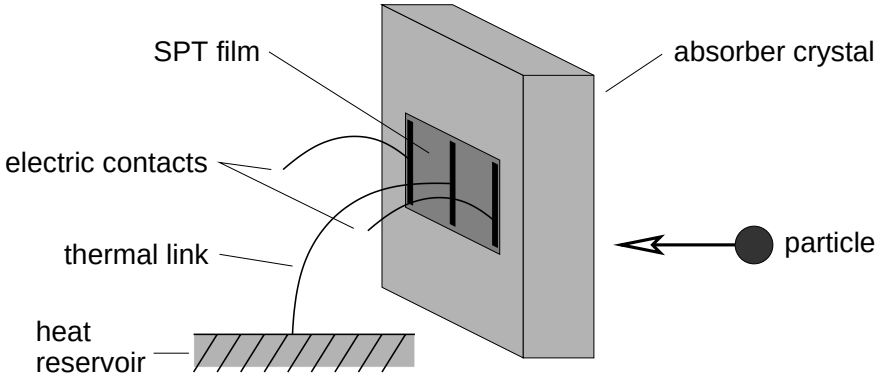

Figure 2.1: Sketch of a cryogenic calorimeter

Particle interactions in the absorber create non-thermal phonons. They are collected in the thermometer film and thermalise there. The thermometer film is an evaporated film of a superconducting material with a transition temperature between 10 mK and 150 mK. Mostly a multilayer film of Iridium and Gold was used, taking advantage of the proximity effect which allows to tune the transition temperature by changing the thickness ratio of the particular Iridium and Gold films [Nag94, Hoe98].

The temperature of the SPT is controlled such that it is in its transition between the normal-conducting and the superconducting state. As shown in figure 2.2, in this region the resistance change with temperature $\mathrm{d}R/\mathrm{d}T$ is very high. Thus, a small temperature change ΔT leads to a large change ΔR in resistance which allows to measure temperature changes of $\sim \mu$K. The change in resistance can be read out electrically.

The detector is coupled to a heat bath by a defined thermal link. The heat bath stabilises the operating temperature of the detector. If the detector is heated up by the deposition of energy, the energy flows to the heat bath via this link and the temperature of the detector relaxes to its operating temperature.

The detector signals show a fast signal rise. It starts when the absorber is hit and ends as soon as all the energy deposited in the absorber is collected in the

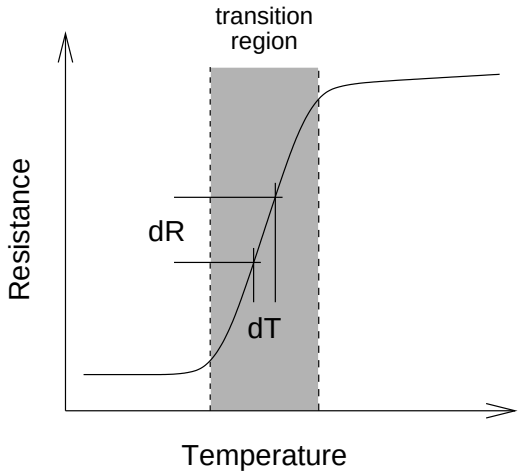

Figure 2.2: Resistance curve of an SPT superconducting film in the normal-conducting to superconducting transition region. $\frac{\mathrm{d}R}{\mathrm{d}T}$ becomes highest inside the transition.

thermometer film. The temperature of the SPT decreases on a longer timescale given by the thermal relaxation of the detector to the heat bath. All processes can be described in time by exponential laws. Figure 2.3 shows such a detector pulse with a model curve using exponential functions to describe the signal evolution. To detect the impact time of an interaction in the absorber, the point in time of the signal onset, which is the intersection of the zero base-line with the signal rise curve, needs to be detected with the highest possible precision.

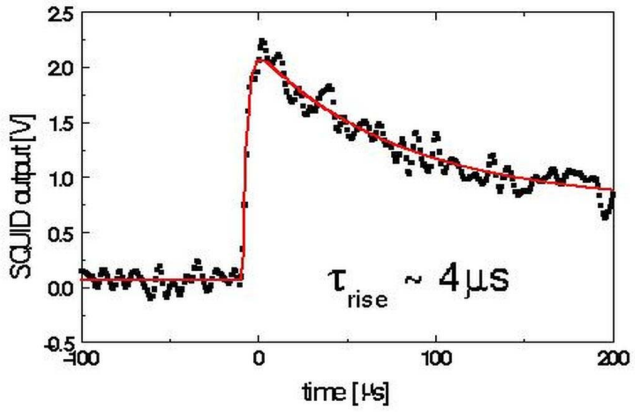

Figure 2.3: A detector pulse (dots: measurement data) with a fit curve (continuous line) using exponential functions.

For this it is necessary to build a detector with a short signal rise time, resulting in a steep intersection angle between base-line and signal curve. Additionally

one needs a high signal amplitude to minimise the time-shift produced by the amplitude noise. With a reasonable signal amplitude (signal-to-noise ratio) it should be possible to determine the signal onset time with a precision of about 1/10 of the exponential rise time constant. This means a rise time of $\tau_{rise} \approx 1.0\,\mu s$ is necessary to achieve the intended time resolution of $\Delta t = 0.1\,\mu$s.

2.2 A Detector Model

The theoretical understanding of cryogenic calorimeters as described in the previous section is based on a model description published first by Pröbst et al. [Pro95]. It accounts for the thermal couplings inside the calorimeter, and the energy flow and relaxation processes.

2.2.1 Heat Flow Equations

A scheme of all components relevant for the thermal processes in the calorimeter is shown in figure 2.4. The model describes the detector as a system of thermally coupled subsystems: The phonon system of the absorber crystal, the phonon system of the superconducting thermometer film, the electron system of the superconducting thermometer film, a heat sink with infinite heat capacity (heat bath), and distinct thermal couplings between these components. In this discussion the absorber crystal is treated as dielectric with only the phonon system carrying thermal energy. The discussion can be extended to other absorber materials [Cho00].

The phonon system of the absorber crystal has the temperature T_a and the heat capacity C_a. It couples thermally to the phonon system of the superconducting film, evaporated onto it, with the Kapitza coupling G_K. Additionally, via the mechanical mounting of the detector, the absorber crystal is as well coupled directly to the heat bath by a parasitic coupling G_{ab}.

The phonon system of the SPT film is coupled to the electron system by the electron-phonon coupling G_{ep}. Since the heat capacity of the phonon system in the thermometer film is very small compared to C_a and the heat capacity of the electron system C_e in the interesting temperature range, it will be neglected. The coupling of the absorber crystal to the electron system in the superconducting thermometer film thus is given as

$$G_{ea} = \left(\frac{1}{G_K} + \frac{1}{G_{ep}}\right)^{-1}. \tag{2.1}$$

The electron system of the thermometer has the temperature T_e. It is directly connected to the heat sink at temperature T_b by the thermal coupling G_{eb}.

An energy deposition ΔE in the absorber crystal creates high-energetic non-thermal optical phonons. They decay by inelastic scattering processes, as will

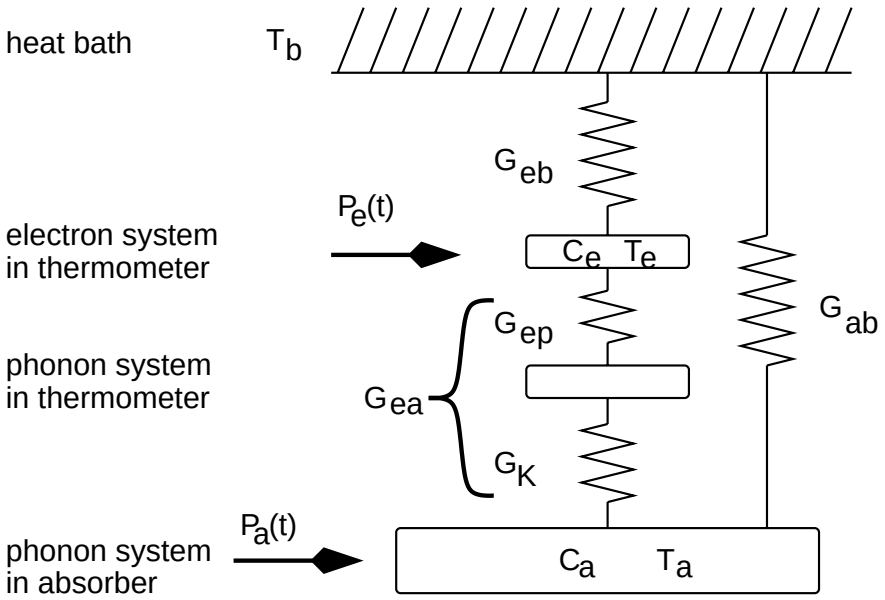

Figure 2.4: Thermal model of the calorimeter detector. $P_a(t)$ and $P_e(t)$ are the power input in the absorber crystal and the electron system of the thermometer film by non-thermal phonons.

be described in sec. 2.2.3. In the timescale of interest of $< 100\,\mu$s the mean phonon frequency in sapphire is still above $> 600\,$GHz and the phonons are not thermalised. These non-thermal phonons are effectively absorbed by the free electrons of the thermometer film causing a power flow $P_e(t)$ into the film. By this process the non-thermal phonon density decays exponentially and so does $P_e(t)$.

Additionally, concurring inelastic phonon decay can take place in the absorber crystal. It causes the energy of the non-thermal phonons to be thermalised, leading to a power flow $P_a(t)$ into the absorber. A fraction ϵ of the initial energy is deposited in the thermometer film, a fraction $(1-\epsilon)$ in the absorber crystal. $P_e(t)$ and $P_a(t)$ can then be written as

$$P_e(t) = \Theta(t) P_0 e^{-t/\tau_n}, \quad P_a(t) = \frac{1-\epsilon}{\epsilon} P_e(t)\,, \tag{2.2}$$

with the step-function $\Theta(t)$, the time constant for the decay of the non-thermal phonons τ_n and the initial power $P_0 = \epsilon \Delta E/\tau_n$. The life time of the population of the non-thermal phonons τ_n is given by

$$\tau_n = (\frac{1}{\tau_{film}} + \frac{1}{\tau_{crystal}})^{-1} \tag{2.3}$$

where τ_{film} is the phonon collection time of the thermometer film and $\tau_{crystal}$ is the life time of non-thermal phonons in the absorber without a thermometer film attached.

In clean crystals, $\tau_{crystal}$ is dominated by surface scattering. In this work detectors with small absorbers ($< 100\,\mathrm{mm}^3$) and large-area thermometer films ($5 - 10\,\mathrm{mm}^2$) are used. A large fraction of the absorber surface is covered by the thermometer film. Since the probability of an inelastic surface scattering is negligible compared to the probability of absorption in the detector film, τ_n can be approximated by

$$\tau_n \approx \tau_{film} = \frac{\tau_{coll}}{\bar{\eta}}\,, \qquad \tau_{coll} = \frac{2V_a}{A < v_\perp \alpha >}\,. \tag{2.4}$$

$\bar{\eta}$ is the probability for a non-thermal phonon that enters the thermometer to be absorbed by free electrons in the thermometer film. τ_{coll} is the ideal collection time of non-thermal absorber phonons in the thermometer film for $\bar{\eta} = 1$. V_a is the absorber volume, A is the area of the absorber crystal covered with the SPT film, $v_\perp$ the phonon group velocity normal to the absorber-thermometer interface, α the transmission probability, and $< \ldots >$ the average over all modes and wave vectors of phonons incident from the absorber onto the absorber-thermometer surface. A more detailed discussion of eqn. (2.4) will be given in sec. 2.2.3.

The thermodynamic system depicted in figure 2.4 is described by two coupled equations for the temperatures T_e and T_a:

$$C_e \frac{\mathrm{d}T_e}{\mathrm{d}t} + (T_e - T_a)G_{ea} + (T_e - T_b)G_{eb} = P_e(t) \tag{2.5}$$

$$C_a \frac{\mathrm{d}T_a}{\mathrm{d}t} + (T_a - T_e)G_{ea} + (T_a - T_b)G_{ab} = P_a(t)\,. \tag{2.6}$$

With the initial condition $T_a(t \le t_0) = T_e(t \le t_0) = T_b$, the thermometer signal $\Delta T_e = T_e(t) - T_b$ is given by the solution

$$\Delta T_e = \Theta(t - t_0)\left[A_n\left(e^{-\frac{t-t_0}{\tau_{in}}} - e^{-\frac{t-t_0}{\tau_n}}\right) + A_t\left(e^{-\frac{t-t_0}{\tau_t}} - e^{-\frac{t-t_0}{\tau_n}}\right)\right] \tag{2.7}$$

with the time constants

$$\tau_{in} = \frac{1}{\nu_{in}} = \frac{2}{a + \sqrt{a^2 - 4b}} \qquad \tau_t = \frac{1}{\nu_t} = \frac{2}{a - \sqrt{a^2 - 4b}} \tag{2.8}$$

$$a = \frac{G_{ea} + G_{eb}}{C_e} + \frac{G_{ea} + G_{ab}}{C_a} \qquad b = \frac{G_{ea}G_{eb} + G_{ea}G_{ab} + G_{eb}G_{ab}}{C_e C_a} \tag{2.9}$$

and the amplitudes

$$A_n = \frac{P_0(\nu_{in} - \frac{G_{ab}}{C_a})}{\epsilon(\nu_{in} - \nu_t)(\nu_n - \nu_{in})}\left(\frac{\nu_t - \frac{G_{ab}}{C_a}}{G_{eb} - \frac{C_e}{C_a}G_{ab}} - \frac{\epsilon}{C_e}\right) \tag{2.10}$$

$$A_t = \frac{P_0(\nu_t - \frac{G_{ab}}{C_a})}{\epsilon(\nu_{in} - \nu_t)(\nu_n - \nu_t)}\left(\frac{\nu_{in} - \frac{G_{ab}}{C_a}}{G_{eb} - \frac{C_e}{C_a}G_{ab}} - \frac{\epsilon}{C_e}\right)\,. \tag{2.11}$$

τ_{in} and τ_t are the time constants of the homogeneous equations. τ_n is the life time of the non-thermal phonon population introduced by $P_e(t)$ and $P_a(t)$, and $\nu_n = \tau_n^{-1}$. In the case that $C_e \ll C_a$[1] the equations simplify and the physical relevance of τ_{in} and τ_t becomes more visual:

$$\tau_{in} \approx \frac{1}{a} \approx \frac{C_e}{G_{ea} + G_{eb}} \qquad (C_e \ll C_a) \tag{2.12}$$

$$\tau_t \approx \frac{a}{b} = \frac{C_a}{\frac{G_{eb}G_{ea}}{G_{eb}+G_{ea}} + G_{ab}} \qquad (C_e \ll C_a)\,. \tag{2.13}$$

Now it can be seen that τ_{in} represents the intrinsic time constant of the electron system of the thermometer and is responsible for carrying heat out of the electron system via its temperature gradient to the environment. τ_t is the time constant of the thermal relaxation of the phonon system of the absorber through all its thermal couplings.

If $\tau_n \ll \tau_{in}$ then the electron system is quickly heated up by non-thermal phonons. The temperature relaxes more slowly to the heat bath and the absorber crystal, with the time constant τ_{in}. On a longer time scale τ_t the absorber crystal and the thermometer film equilibrate to the temperature of the heat bath. The amplitude of the non-thermal component A_n measures the total absorbed heat. This operating mode is the "calorimetric mode". The signal rise time of the calorimeter is given by the life time of non-thermal phonons $\tau_n \approx \tau_{film}$ of eqn. (2.4).

In the case $\tau_n \gg \tau_{in}$ the detector is operated in "bolometric mode" and the signal rise time is given by τ_{in}. The detectors used for this work are operated as calorimeters.

In the following two sections the heat capacities and the coupling constants used in the thermometer model will be discussed in detail.

2.2.2 Heat Capacities

The heat capacity plays an important role when building temperature sensitive detectors. An amount of energy δE causes a temperature rise $\delta T = \delta E/C$, with the total heat capacity $C = V \cdot c_v$ in a volume V with the specific heat c_v. It is necessary to keep the heat capacity C small for high sensitivity. The relevant contributions to the heat capacity of our cryogenic calorimeters will be discussed.

Dielectrics

Insulators do not contain free conduction electrons, the heat capacity is usually[2] dominated by the phonon systems. In regular crystal lattices at low temperatures

[1] The assumption $C_e \ll C_a$ is only made for illustration. It is not the case for our detectors.

[2] This is not always the case, for example in paramagnetic salts magnetic interaction between unpaired shell electrons may as well develop an enormous heat capacity.

it is described by the Debye model [Deb12] and is

$$C_D = \frac{12\pi^4}{5} N k_B \left(\frac{T}{\theta_D}\right)^3 \qquad (T \ll \theta_D) \tag{2.14}$$

with N the number of atoms, $k_B = 1.38 \cdot 10^{-23}\,\mathrm{J/K}$ Boltzmann's number, T the temperature and $\theta_D = \frac{\hbar v_g}{k_B}\left(6\pi^2 \frac{N}{V}\right)^{\frac{1}{3}}$ the Debye temperature. v_g is the phonon group velocity, V the volume. The Debye model is valid for temperatures well below θ_D and as long as no singularities in the phase space are excited where $v_g \to 0$. These conditions are fulfilled for all materials at the operating temperature of our detectors.

The absorber material Al_2O_3 used in the majority of the investigated detectors has a comparably high Debye temperature $\theta_D(Al_2O_3) = 1040.7\,\mathrm{K}$. Thus, besides having a high group velocity to homogenise spatial temperature distributions quickly, its heat capacity is quite low even for large absorber volumes.

Metals

In Metals, at temperatures below 1 K, the contribution of the electronic heat capacity C_{el} is several orders of magnitude higher than the phononic contribution, and dominates the total heat capacity. It is given by

$$C_{el} = \frac{\pi^2}{2} N_e k_B \cdot \frac{T}{T_F} = \gamma V T \qquad (T \ll T_F)\,. \tag{2.15}$$

Here N_e is the number of electrons, γ is a material constant. The Fermi temperature T_F is defined by the Fermi energy $E_F = k_B T_F$. Fermi temperatures of metals are in the range of $10^4 - 10^5\,\mathrm{K}$.

Superconductors

Since in the superconducting state most of the conduction electrons are bound to Cooper pairs, they do not contribute to the specific heat. The specific heat of superconductors well below their transition temperature T_C is dominated by the Debye specific heat C_D.

However, at the transition temperature the BCS-theory predicts an increase in heat capacity. It is due to the condensation of electrons to Cooper pairs which is a second-order phase transition. At T_C, as long as no external magnetic field is applied, the specific heat is increased to 2.43 times the electronic heat capacity of the normal-conducting case [Ash76].

Near the transition temperature the specific heat of a superconducting film can be approximated by considering the electron gas being partially superconducting. The electrons in the normal-conducting state hold electronical specific heat. The electrons frozen out to cooper pairs, forming the superconducting part, hold the

increased specific heat. A measure for this fractioning is the resistance R_F of the superconductor. The fraction of the film in the superconducting state is approximated by $(1-R_F/R_N)$, with R_N being the normal-conducting resistance. The specific heat for temperatures near the transition temperature T_C can be approximated

$$c \approx c_{el}\frac{R_F}{R_N} + 2.43c_{el}\left(1-\frac{R_F}{R_N}\right) = c_{el} + 1.43c_{el}\left(1-\frac{R_F}{R_N}\right) \quad (T \approx T_C)\,. \quad (2.16)$$

At temperatures below $T_C/2$ the heat capacity of a superconductor can be approximated according to the BCS theory by [Bar57, Cor56]

$$C \approx 1.34\gamma T_C \left(\frac{\Delta}{k_B T}\right)^{\frac{3}{2}} e^{-\frac{\Delta}{k_B T}} \qquad (T \leq \frac{T_C}{2}) \quad (2.17)$$

with the material constant γ of eqn. (2.15) and the superconducting energy gap 2Δ.

2.2.3 Relaxation and Coupling Processes

In the following section the different relaxation and coupling mechanisms occurring in the detector will be discussed. This section completes the description of the cryogenic calorimeter model.

Absorber Crystal

By the absorption of energy in the absorber crystal, initially high-frequency non-thermal, mainly optical, phonons of frequency ω are created. Due to anharmonic terms in the lattice potential these phonons decay quickly via three-phonon processes. These take place under energy and momentum conservation, and lead to a rapid decay to acoustic phonons of about half the Debye frequency ν_D. For sapphire, the Debye frequency is $\nu_D = 21.7\,\mathrm{THz}$.

Acoustic phonons exist in three polarisations, a longitudinal and two transverse modes. Further decay takes place only for longitudinal acoustic phonons. They decay with a rate of

$$\Gamma_{dec} = \gamma_{dec}\omega_D \left(\frac{\omega}{\omega_D}\right)^5 \quad (2.18)$$

into two transverse acoustic phonons [Kaz86]. γ_{dec} is a material constant and $\omega_D = 2\pi\nu_D$. Other decay channels are comparatively well suppressed [Tam95]. The transverse acoustic phonon branch is energetically lowest and no direct further decay is possible[3].

[3] In anisotropic crystals a decay channel to another $\vec{k}$ vector direction exists, but the decay rate via this channel is negligible.

Without other phonon scattering mechanisms, the longitudinal acoustic phonon branches would quickly be de-populated and high-energetic transverse acoustic phonons would persist for a long time. Elastic phonon scattering at lattice defects provides a channel for further decay of transverse acoustic phonons. This is possible for all acoustic phonon modes and allows a conversion of the phonon modes between longitudinal and transverse acoustic phonons. Thereby, while converting down by longitudinal phonon decay, the ratio between longitudinal and transverse phonon modes is maintained according to the density of states. Since the used absorber crystals are very pure and defect-free, the most relevant lattice defect is the mass disorder introduced by different isotopes. For example in sapphire oxygen appears at its natural isotope distribution as ^{16}O, ^{17}O and ^{18}O. The scattering rate caused by isotope scattering is given as [Mar90]:

$$\Gamma_{iso} = \gamma_{iso}\omega_D \left(\frac{\omega}{\omega_D}\right)^4 \tag{2.19}$$

with γ_{iso} a specific constant.

Usually Γ_{iso} is higher than Γ_{dec}. In sapphire, about 10% of the phonons are longitudinal and 90% are transverse acoustic phonons. The effective decay rate for all non-thermal phonons is reduced to about 1/10 of Γ_{dec}.

During the first decay generations the mean-free-path of the phonons enlarges rapidly with decreasing phonon frequencies. This process is commonly referred to as quasi-diffusive propagation. The phonon mean-free-path quickly reaches the length scale of the crystal dimensions. From this point on the phonon propagation usually is of ballistic nature.

Phonon Transmission Across Surfaces

The transmission probability of thermal phonons between two well bonded surfaces can be approximated by the acoustic impedance mismatch between the two solids [And81, Pro95].

The Kapitza conductance g_K is defined as the net energy flow per unit time and unit area between two media 1 and 2 having a temperature gradient ΔT:

$$g_K = \frac{\dot{q}_{1\to2}(T+\Delta T) - \dot{q}_{2\to1}(T)}{\Delta T}\,. \tag{2.20}$$

$\dot{q}_{1\to2}$ and $\dot{q}_{2\to1}$ denominate the energy flux per unit time and unit area carried by phonons from medium 1 into medium 2, and vice versa. If there is no temperature difference $\Delta T = 0$, the two fluxes are equal. $\dot{q}_{1\to2}$ is given by the sum over all phonon wave vectors $\vec{q}$ and phonon modes m in medium 1 with volume V, each carrying the energy $\hbar\omega(\vec{q}, m)$,

$$\dot{q}_{1\to2} = \sum_{\vec{q},m} n(\omega, T)\frac{\hbar\omega(\vec{q}, m)}{V} v_\perp(\hat{q}, m)\alpha(\hat{q}, m)\,. \tag{2.21}$$

$v_\perp(\hat{q}, m)$ is the component of the group velocity normal to the interface, $\hat{q} = \vec{q}/\left|\vec{q}\right|$, and $\alpha(\hat{q}, m)$ is the total transmission probability of an incident phonon in medium 1 to be transmitted to any mode in medium 2. The distribution function $n(\omega, T)$ for phonons is given by the Bose-Einstein distribution,

$$n(\omega, T) = \frac{1}{(e^{\hbar\omega/k_B T} - 1)} \,. \tag{2.22}$$

The sum over all phonon wave vectors $\vec{q}$ can be converted to an integral, and the integration over all $\vec{q}$ can be transformed to an integration over all group velocities $v_\perp > 0$ in the $\vec{q}$ space with $v_p(\hat{q}, m) = \omega/|\vec{q}|$. The integration angle is restricted to $v_\perp > 0$ since only group velocities directed towards the boundary interface contribute to the energy transport. Finally the integral can be split in a thermal energy density $< E/V >$

$$< E/V >= \frac{1}{(2\pi)^3} \int_0^\infty n(\omega)\hbar\omega^3 d\omega \sum_m \int \frac{d\Omega}{v_p^3} \tag{2.23}$$

and a mean phonon transmission probability $< v_\perp \alpha >$

$$< v_\perp \alpha >= \frac{\sum_m \int_{v_\perp > 0} v_\perp \alpha \frac{d\Omega}{v_p^3}}{\sum_m \int_{v_\perp > 0} \frac{d\Omega}{v_p^3}} \,, \tag{2.24}$$

whereby $\dot{q}_{1\to 2}$ becomes:

$$\dot{q}_{1\to 2} =< E/V > \frac{1}{2} < v_\perp \alpha > \,. \tag{2.25}$$

The factor 1/2 results from the integration over group velocities $v_\perp > 0$. Introducing the heat capacity per unit volume C_1/V_1 of medium 1 and calculating $\dot{q}_{2\to 1}$ similarly, the Kapitza coupling (2.20) can be written as

$$g_K = \frac{C_1}{2V_1} < v_\perp \alpha > \,. \tag{2.26}$$

Some interesting interfaces and their Kapitza conductances g_K are given in Table 2.1 [Pro95, private communication]. The Debye temperatures θ_D were calculated for the source media emitting the phonons. They are a byproduct of the calculation of $< v_\perp \alpha >$ and are calculated from the elastic constants.

Electron-Phonon Interaction

In metals electron-phonon scattering allows an energy transfer between the electron system and the phonon system. Electron-phonon scattering takes place also in superconductors at the transition temperature, as a fraction of the electrons is not bound to cooper pairs and can scatter.

transmission from → to	$< v_\perp \alpha >$ [m/s]	$< \alpha >$	g_K/T^3 [kW K^{-4}m^{-2}]	θ_D [K]
$Al_2O_3 \rightarrow$ Ir	2292	0.551	0.387	1040.8
$Al_2O_3 \rightarrow$ Au	3125	0.776	0.528	1040.8
$Al_2O_3 \rightarrow$ W	2550	0.616	0.430	1040.8
Si → Ir	1289	0.366	0.383	647.9
$CaWO_4 \rightarrow$ W[a)]	647.6		1.783	246.6

Table 2.1: Calculated $< v_\perp \alpha >$, $< \alpha >$, Kapitza conductivities g_K and Debye temperatures θ_D of the source medium of selected absorber–thermometer interfaces [Pro95]. [a)]private communication F. Pröbst, MPI of Physics, Munich.

The electron-phonon interaction is described by the Pippard-model [Pip55] for the simple case of a spheric Fermi-surface. Though the model still gives an understanding for metals with complex Fermi-surfaces. For thermalised phonons with small momentum compared to the inverse mean free path of the electrons l_e, $k \cdot l_e \ll 1$, the electron-phonon interaction strongly depends on the temperature [Fra93]:

$$G_{ep} = g_{ep} V \cdot T^n \tag{2.27}$$

$$g_{ep} = \frac{6!1.017 k_B^6}{2\pi^2 \hbar^5} \left(\frac{C_T}{v_T^2} + \frac{C_L}{v_L^2} \right) , \tag{2.28}$$

with the metal volume V, the sound velocities v_L and v_T of the longitudinal and transverse phonons, and C_T and C_L the constants from the Pippard theory. In the Pippard-model, $n = 5$. Experimentally it was found between $n = 4 \ldots 5$ [Rou85, Pro95].

The strong temperature dependence of G_{ep} leads to a thermal decoupling of the phonon and electron system at low temperatures. This has a significant impact on the performance of low-temperature detectors. High-frequency phonons are absorbed well by the free electrons of the thermometer film, and the energy deposited in the absorber is effectively collected in the thermometer. The excited electrons thermalise quickly by electron-electron scattering, the reverse process of electron-phonon scattering is suppressed by the factor $\sim T^{4\ldots5}$. This leads to a strong overheating of the free electrons in the SPT film (hot-electron effect).

For non-thermal phonons with $k \cdot l_e \gg 1$ the situation is different. The absorption lengths $l_L$and l_T can be given for the scattering of longitudinal and transverse phonons. Longitudinal phonons are scattered more effectively than transverse phonons of the same frequency. For typical SPT film thicknesses $d \sim \mathcal{O}$(kÅ) it turns out that usually $l_L \ll d$ and $l_T \gg d$. This means that phonons transmitted in the longitudinal mode are absorbed by the electrons of the film whereas transverse phonons do not interact and are re-transferred into the absorber crystal.

An overall effective absorption probability $\bar{\eta}$ can be defined:

$$\bar{\eta} = \frac{< v_\perp \alpha \eta >}{< v_\perp \alpha >} \tag{2.29}$$

with $\eta = 1$ for all longitudinal phonon modes and $\eta = 0$ for all transverse phonon modes. Thereby it was assumed that the angular distribution of the non-thermal phonons is the same as the angular distribution of the thermal phonons. This is the case because even though the spectral distribution of non-thermal phonons has not thermalised yet, they have experienced many elastic scatterings. Meanwhile their directions were randomised according to the density of states. The absorption probabilities calculated and measured by [Pro95] are around $\bar{\eta} \approx 30\%$.

Absorber-Thermometer Coupling

The energy deposition in the electron system of the SPT by the non-thermal phonons from the absorber, $P_e(t)$ is given by a phonon transmission probability from the absorber to the thermometer film and the electron-phonon interaction in the thermometer film. As discussed above, the absorption of non-thermal phonons can be described by an effective absorption probability $\bar{\eta}$. The phonon transmission probability can be calculated from eqn. (2.25) in analogy to the Kapitza coupling. The average $< v_\perp \alpha >$ for the non-thermal phonons is the same as for the thermal phonons, as explained above. Only the energy density $< E/V >$ has to be replaced by the energy density of the non-thermal phonons. The resulting expression for the phonon collection time is

$$\tau_{film} = \frac{1}{\bar{\eta}} \frac{2V_a}{A < v_\perp \alpha >} \,. \tag{2.30}$$

This is the result already used in eqn. (2.4).

Coupling to the Heat Bath

The SPT films of the cryogenic calorimeters may be coupled to the heat bath in two different ways: Directly via a gold wire or indirectly through the substrate. To reduce the contact resistance between gold wire and thermometer film in the case of direct coupling, a gold pad of about $\sim 1\,\mathrm{mm}^2$ size was sputtered onto the superconducting film. The thermal conductivity κ of the wire is related with its electrical conductivity σ by the Wiedemann-Franz law $\kappa = \sigma \mathcal{L} T$. The electron-bath coupling is

$$G_{eb} = G_{Au} = \mathcal{L} \frac{T}{R} \tag{2.31}$$

where $\mathcal{L} = (\pi k_B/e)^2/3 = 24.5 \cdot 10^{-9}\,\mathrm{W\Omega K^{-2}}$ the Lorenz number, R the electrical resistance of the wire and e the electron charge.

Some of the detectors were thermally coupled – indirectly – via the absorber substrate. This method was used especially for detectors which had certain patterns structured in the SPT film, with no space to add a bond pad for the gold wire. These detectors were thermally coupled just by the absorber-bath coupling G_{ab}. This was possible as our detectors usually have a transition temperature $T_C \sim 100\,\mathrm{mK}$. Compared to transition temperatures $T_C \sim 10\,\mathrm{mK}$ as used in other projects like the CRESST experiment [Ang02], the electron-phonon coupling $G_{ep} \propto T^5$ is about five orders of magnitude higher. The coupling of the absorber to the heat bath was done via a sputtered gold pad on the absorber which was clamped to the heat bath. The relaxation time of the thermometer film was measured to be some $100\,\mu\mathrm{s}$.

2.3 Relaxation Processes Inside the SPT Film

The detector model described in the previous sections assumes a uniform distribution of phonons and electrons in the different detector components. In this model the signal rise time is described by the life time of non-thermal phonons τ_n (eqn. 2.4). In other applications, for example [Ang02, Ben03] aiming for very good energy resolution, the coupling time constants are usually chosen long compared to internal homogenisation times. In detectors aiming for a short signal rise time however, the timescale of homogenisation processes inside the distinct statistical ensembles may become comparable to τ_n.

In general, effects of spatial inhomogeneities reduce the energy resolution and may drastically influence the pulse shape and thus the time resolution of our detectors. The influence of inhomogeneous phonon- and electron distributions on the signal rise time of the cryogenic detectors requires a special investigation. The discussion is divided in two sections. This first section covers homogenisation processes in the SPT film, the section afterwards covers the absorber crystal.

2.3.1 Propagation of Heat in Metal Films

Energy can be deposited uniformly in the SPT film, when the phonons collected from the absorber crystal are also uniformly distributed in the absorber. On the other hand energy can be deposited within a small spot in the SPT film, leading to a local overheating. This happens for example if a particle deposits its energy directly in the SPT film and not in the absorber crystal. It also happens if a local accumulation of non-thermal phonons in the absorber crystal reaches the SPT. This may be the case if the absorber crystal is thin compared to the width of the SPT film. The non-thermal phonons created in the crystal will be absorbed in the film before they distribute uniformly in the absorber. Phonons appearing at the crystal–SPT interface are absorbed with a typical probability of about 50%. The other 50% are reflected and re-reflected at the backside of the crystal. Only

a few reflections will be necessary until the majority of the non-thermal phonons is collected in the SPT. They will not spread much further than a few times the crystal thickness during the collection time, and the electron gas of the SPT film will be heated locally.

The propagation of such a locally overheated spot is of interest for the formation of the detector signal. For 1-dimensional metal films having an electrical resistance R and a heat capacity C, the timescale at which a temperature distribution of the conduction electrons (the phononic heat is neglected) homogenises, is given by:

$$\tau_{el} = \frac{RC}{\mathcal{L}T} \tag{2.32}$$

where T is the temperature of the free electrons. Replacing $R = l/(A\sigma)$ by the electrical conductivity and $C = lAc_{el}$ by the specific heat and the length l and cross section A of the film, one obtains

$$\tau_{el} = \frac{l^2 c_{el}}{\sigma \mathcal{L} T}\,, \tag{2.33}$$

which is the time constant of a diffusive homogenisation process with the thermal diffusion constant $D = \sigma\mathcal{L}T/c_{el} = \kappa/c_{el}$. In the last step the thermal conductivity was replaced using the Wiedemann-Franz law. It is interesting to note that τ_{el} does not depend on the temperature since $c_{el} \propto T$.

Using values of one of the detectors used in this work[4], the homogenisation time of the SPT film was calculated to be $\tau_{el}(CH425C1) = (3\,\mathrm{mm})^2 \cdot 76\,\mu\mathrm{s/mm}^2 = 680\,\mu\mathrm{s}$. This clearly shows that the homogenisation of the film's temperature is much longer than the observed signal rise times $\mathcal{O}(\mu\mathrm{s})$.

2.3.2 Signals from an Inhomogeneously Heated Film

Since the observed signal rise times are much faster than the homogenisation of a temperature distribution inside the SPT film, the detector signal can not be explained by the homogenisation time constant τ_{el}. In the following it will be shown that a detector signal – in other words a resistance change of measurable height – already arises if the hot region, carrying the deposited energy, covers only a small fraction of the total SPT film area.

Non-Thermal Phonon Life Time

Before discussing the signal formation in the SPT film, it shall briefly be shown that the life time of non-thermal phonons (eqn. 2.4) does not change in the case of inhomogeneous phonon collection in the SPT film like in the above mentioned

[4]Detector *CH425C1*, $c_{el} = 308\,\frac{J}{m^3 K^2} \cdot T$, $\sigma = 1.7 \cdot 10^8\,(\Omega m)^{-1}$

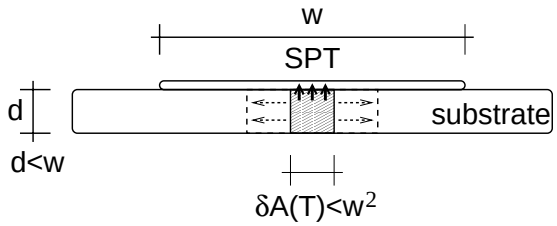

Figure 2.5: Sketch for the explanation of the spatially inhomogeneous phonon collection in the SPT film. The volume $d \cdot \delta A$ in the substrate containing non-thermal phonons spreads out below the SPT film. All phonons are assumed to be absorbed as long as the spot fully lies below the SPT film.

case of a thin absorber crystal with a large-area SPT film on it. This assures that the detector model of sec. 2.2 is still valid in the inhomogeneous case.

Non-thermal phonons created in a point in a thin absorber crystal of thickness d will quickly spread across the whole substrate thickness. Thereafter the cloud of non-thermal phonons spreads out cylindrically in the plane of the crystal. The cylinder's cross section is δA. Meanwhile the phonons will be absorbed in the SPT film. The situation is sketched in figure 2.5. At each point in time the life time of non-thermal phonons τ_n is determined by the volume $d \cdot \delta A$ and the interface area δA of the cylinder containing the non-thermal phonons, and eqn. (2.4) translates into

$$\tau_n = \frac{1}{\bar{\eta}} \frac{2V_a}{A < v_\perp \alpha >} \rightarrow \tau_n = \frac{1}{\bar{\eta}} \frac{2d \cdot \delta A}{\delta A < v_\perp \alpha >} = \frac{1}{\bar{\eta}} \frac{2d}{< v_\perp \alpha >} . \qquad (2.34)$$

Thus τ_n does not depend on the spread of the non-thermal phonons below the thermometer film. This remains valid as long as all phonons are collected during their propagation below the SPT film and none of them escape into parts of the substrate crystal which are not covered by the SPT.

This result shows that the life time of non-thermal phonons τ_n is not affected by inhomogeneous phonon- and energy absorption in the SPT film.

Signal Formation

The measurement signal of a cryogenic calorimeter is the current change caused by the resistance change $\Delta R(t)$ of the SPT film. A uniform deposition of energy ΔE in the whole SPT film leads to a uniform temperature rise ΔT which, operating the SPT in its superconducting–to–normal-conducting transition, leads to a resistance change ΔR. With a simple consideration it can be seen that ΔR is approximately the same if ΔE is deposited uniformly and the film resistance is changed uniformly, or if ΔE is deposited in a single film element increasing its

resistance δR to $\delta R + \Delta R$. Hereby it is assumed that the resistance change is proportional to the deposited energy, $\Delta R \propto \Delta T \propto \Delta E$.

Let the SPT film be split in a serial network of resistor elements δR. Then it is clear that the total resistance change of the network is ΔR no matter whether the resistance of one element is increased by ΔR or if the resistance of n elements is increased to $\Delta R/n$. The same is true for a parallel network of resistor elements δR, but in the approximation that the resistance change of a single element is small, $\Delta R^2 \ll \delta R^2$ [5].

The consideration is an approximation only, since the two-dimensional SPT film is a not isolated network of parallel and serial resistors. Additionally, the assumption $\Delta R \propto \Delta T$, in real-life SPT films, is fulfilled only for very small resistance changes compared to the normal-conducting film resistance.

However it may be useful for films which are heated locally on a spot in the order of $\approx 1\,\mathrm{mm}$ diameter, caused for example by to the collection of an inhomogeneous phonon distribution from the absorber. Then ΔT and ΔR are small and the model shows that such a detector may develop a resistance change in the SPT film which can be very similar to that of a homogeneously heated film.

In conclusion, the detector signal rise $\Delta R(t)$ is, even in the case of inhomogeneous phonon collection, given by the life time of non-thermal phonons τ_n of eqn. (2.4). Neither does τ_n depend on the propagation of non-thermal phonons in the substrate crystal, nor does the film resistance change ΔR strongly depend on the spatial absorption of the deposited energy ΔE.

2.3.3 Direct Particle Impact onto the SPT Film

In this work the detectors were used not only in the conventional way, using the substrate as the absorber. In some measurements the molecules were shot directly onto the thermometer film. No obvious influence on the time resolution of the detector was observed. However, the heating of the detector due to infrared radiation absorption could be reduced since the SPT film has a higher reflectivity than the sapphire crystal.

It needs to be shown that the detector model of sec. 2.2 remains valid in the limit of instantaneous energy deposition in the SPT film. However a new description of the signal rise is necessary. It is discussed subsequently. While discussing the energy propagation in the SPT film, the thermal coupling to the substrate crystal needs to be considered as well. This energy relaxation will be discussed in the end.

[5] The statement is exact for the change in conductance ΔR^{-1} and with $\Delta R^{-1} \propto \Delta E^{-1}$. For the change in resistance it is approximately true as long as $\Delta R^2 \ll \delta R^2$.

Extending the Detector Model

Depositing the energy directly in the SPT film rises the question of how this affects the detector signal formation. There is no obvious reason why the decay times τ_t of the thermal and τ_{in} of the non-thermal component of the detector signal should be affected. The life time τ_n of non-thermal phonons of eqn. (2.4) becomes irrelevant though.

Mathematically, the new situation is represented by performing the limit $\tau_n \to 0$ in the differential equations. This neglects in a first simplified approach all homogenisation processes inside the thermometer film. The free electrons in the SPT film are assumed to be heated up instantaneously[6].

This affects the power inputs by non-thermal phonons eqn. (2.2) as well. $P_a(t)$ into the absorber crystal vanishes and $\epsilon = 1$. All the energy goes directly into the thermometer film and eqn. (2.2) is replaced by the new power inputs

$$P_e(t) = \delta(t - t_0)\Delta E, \quad P_a(t) = 0\,. \tag{2.35}$$

$\delta(t - t_0)$ is Dirac's Delta function.

The solution of the differential eqn. (2.5) and (2.6) for the new situation is derived from the eqn. (2.7)–(2.11). As expected performing the limit $\tau_n \to 0$ is allowed in all equations and leads to the solution of the detector model for instantaneous energy deposition in the SPT film:

$$\Delta T_e = \Theta(t - t_0)\left(A_n \cdot e^{-\frac{t-t_0}{\tau_{in}}} + A_t \cdot e^{-\frac{t-t_0}{\tau_t}}\right) \tag{2.36}$$

with the new amplitudes

$$A_n = \Delta E \cdot \frac{\nu_{in} - \frac{G_{ab}}{C_a}}{\nu_{in} - \nu_t}\left(\frac{\nu_t - \frac{G_{ab}}{C_a}}{G_{eb} - \frac{C_e}{C_a}G_{ab}} - \frac{1}{C_e}\right) \tag{2.37}$$

$$A_t = \Delta E \cdot \frac{\nu_t - \frac{G_{ab}}{C_a}}{\nu_{in} - \nu_t}\left(\frac{\nu_{in} - \frac{G_{ab}}{C_a}}{G_{eb} - \frac{C_e}{C_a}G_{ab}} - \frac{1}{C_e}\right)\,. \tag{2.38}$$

As shown, the detector model still describes the decay times τ_t of the thermal and τ_{in} of the non-thermal signal components and their amplitudes. However this approach does not describe the formation of the signal rise in the situation of directly absorbing particles in the SPT film. The signal rise needs do be described independently of the detector model, since it will be given by inhomogeneous relaxation processes, whereas the detector model treats all its thermodynamical subsystems as being homogenised.

[6]More precisely, the energy is deposited in the film's free electrons and phonon system according to the proportion of their heat capacities. Since the electronic specific heat is by far dominating, almost all the energy is deposited in the free electrons of the thermometer film.

Energy Propagation in the SPT Film

It is rather complex to estimate the real development of the signal rise with time, but some ideas about the energy propagation in the SPT film can be given. However drawing conclusions concerning the formation of the film resistance change $\Delta R(t)$ is at present knowledge not possible. The biggest uncertainty in all considerations is the non-uniformity of the real SPT film. Its transition temperature varies across the surface and influences the local sensitivity. Some areas may even be fully superconducting. Although in such an area a developing normal-conducting region is shorted by its surrounding, a dynamic resistance change will arise owing to the relocation of superconducting current paths.

A closed formula describing the detector signal cannot be provided, but it is possible to draw a rough picture of the occurring processes.

What may happen once a molecule deposits its kinetic energy at the surface of the SPT film can be shown by a simple estimation. A typical molecule with a mass of 100 kDa is equivalent to about 8000 carbon atoms. With an atomic distance of $\sim$ 0.1 nm this represents a ball of $\varnothing$ 2.5 nm diameter. The real molecule is somewhat larger since the molecules are not closely packed. When the molecule hits the SPT film, its kinetic energy of typically 10 keV may at first be deposited in the film in a hemisphere of presumably 5 nm diameter. The energy will quickly be thermalised among the conduction electrons [Moo81] in this volume. Using $C(T) \approx 1.9\,\mu\mathrm{eV}/(\,\mathrm{nm}^3\mathrm{K}^2)\cdot V \cdot T$, this leads to a local temperature rise of $\sim 6000\,\mathrm{K}$! As this hot region spreads out driven by the temperature gradient, it will enlarge across the whole film thickness. Further it will acquire a cylindrical shape and spread in the plane of the SPT film. The thickness of one of our films (detector *CH425C1*) was 55 nm. In a cylinder of that diameter and height, the mean temperature rise of the hot region reaching the film-substrate interface still is $\sim 280\,\mathrm{K}$.

It is interesting to note that due to the linear temperature dependence of $C(T)$ the mean temperature in such an expanding hot cylinder ($\Delta T \gg T_0$, T_0 the environmental temperature) decreases with the the square root of its volume, $T \propto \sqrt{1/V}$, thus linearly with its increasing radius, $T \propto 1/r$.

Signal Formation

The observed signal rise times of our detectors are in the order of $\mathcal{O}(\mu\mathrm{s})$. Using eqn. (2.33) shows that after $\tau_{el} = 1\,\mu\mathrm{s}$ the hot region has a radius $r = 0.12\,\mathrm{mm}$. Its mean temperature rise is then $\Delta T = 14\,\mathrm{mK}$, at an operating temperature of $T_0 = 150\,\mathrm{mK}$. Depending on the steepness of the superconducting–normal-conducting transition it is likely that the SPT film is driven normal-conducting inside the hot region. As the detectors are usually operated at a temperature where the SPT film resistance is about $R_{op} \approx (0.2 \ldots 0.5) R_N$ of its normal-conducting value, the film resistance in the hot region is at least doubled. Since

the radius of the hot region is too small and the resistance change is high, the simplified model describing the resistance change of the SPT used in sec. 2.3.2 can not be used in this case.

To estimate the rise of the total film resistance ΔR due to the local resistance change the situation is simplified to fit to a classical electrodynamic problem. A geometry of two concentric circles is considered. The larger one, having the radius $w/2$ and a resistivity ρ_{op}, represents a circle inscribed into the SPT film. The smaller one with the radius $r \ll w/2$ and the resistivity ρ_N represents the hot region. An equivalent resistivity ρ for this problem has already been discussed by C. Maxwell in [Max54] in the tree dimensional case. A. Kadin and M. Johnson used a generalisation of Maxwell's result in [Kad96] to derive an approximation for ΔR in the two dimensional case,

$$\frac{\Delta R}{R_{op}} = 8\frac{r^2}{w^2}\frac{R_N - R_{op}}{R_N + R_{op}}\,. \tag{2.39}$$

R_N is the normal-conducting resistance of the thermometer and R_{op} its resistance at the operating point. Using $r = 0.12\,\mathrm{mm}$, $w = 3\,\mathrm{mm}$ and $R_{op} = 0.5R_N$ results in a resistance change $\Delta R/R_{op} = 0.4\%$. With a usual measurement setup with a current $I_{tot} = 50\,\mu\mathrm{A}$ (see sec. 4.5.2) it results in a signal of detectable amplitude at the SQUID output of 0.3 V.

In conclusion, after a molecule impact onto the SPT film, a region of elevated temperature of only 0.12 mm size is already detectable after 1μs. During further propagation of the hot region the detector signal will rise as a larger area of the film is heated. Meanwhile the hot region cools by expansion until its temperature comes to a regime where $\Delta R \propto \Delta T$ as discussed before. From this point on no further resistance increase is expected with increasing size of the hot region.

Coupling to the Substrate: A Hotspot Model

Finally the energy loss of a hot region to the substrate crystal via the thermal coupling of the SPT film to the substrate needs to be investigated. A. Kadin and others [Kad96, Gup99] developed a hotspot model which describes the expansion and collapse of a transient hot region created by a particle impact in thin metal films of thickness $d \approx \mathcal{O}(10\,\mathrm{nm})$. Such a hotspot will expand in the film while it couples to the substrate. A. Kadin and his colleagues solved the heat flow equations and received a solution described by a "thermal healing length" Λ_{hs} and a "hotspot relaxation time"

$$\tau_{hs} = \frac{c_{el}d}{g_{ea}}\,, \tag{2.40}$$

with $g_{ea} = G_{ea}/A$ the per-unit area electron-absorber coupling. τ_{hs} represents the timescale at which the energy escapes to the substrate. The relevance of Λ_{hs}

and τ_{hs} in the hotspot model is that at $t = \tau_{hs}$, 63% of the energy lie inside a circle of diameter Λ_{hs}.

The hotspot model was developed for optical photon impact, thus for low energy deposition and low temperature rise. It is a solution of the heat flow equations for the case of constant $c_{el}(T)$, $\kappa(T)$, $g_{ea}(T) \approx const.$, thus only for small temperature changes $\Delta T \ll T$. At the low operating temperatures and the high impact energies of our detectors this is not fulfilled. However a coarse comparison between the timescale of energy loss to the substrate, τ_{hs}, and the timescale of cooling of the hot region by its expansion, τ_{el} (eqn. 2.33), might be given.

As mentioned before, the temperature decrease of a cylindrical hot region due to an expansion is inversely proportional to its radius, $T \propto r^{-1}$. The speed of this expansion is given by eqn. (2.33) and is proportional to the radius squared, $\tau_{el} = r^2 c_{el}/\kappa \propto r^2$, since $c_{el} \propto T$, $\kappa \propto T$. Due to the change in temperature with expanding radius, τ_{el} is not constant but is a measure of the speed of the expansion of the hot region at a certain time. It develops with the temperature as $\tau_{el} \propto T^{-2}$.

The hotspot relaxation time τ_{hs} is defined for a fixed temperature T only. However with the same consideration as above, with changing temperature a τ_{hs} can be given at any time which can be seen as a measure of the current coupling of the hotspot to the substrate. For higher temperatures ($T \gtrsim 1\,\mathrm{K}$) the electron-phonon coupling is much stronger than the Kapitza coupling and the coupling is given by $g_{ea} \approx g_K \propto T^3$. Then τ_{hs} scales with the temperature of the hot region as $\tau_{hs} \propto c_{el}/g_{ea} \propto T^{-2}$, since g_{ea} will be dominated by the temperature of the hot partner.

This means that the ratio τ_{hs}/τ_{el} will be the same in any stadium of the expansion of the hot region. The fraction of the energy lost to the substrate will be independent of the temperature at any time.

For example, a hot region as discussed before for detector *CH425C1* will reach a mean temperature of $T = 1\,\mathrm{K}$ at the time $\tau_{el} = 3.3\,\mathrm{ns}$ after the particle impact. Then it has enlarged to a radius of $6.8\,\mu\mathrm{m}$. At a temperature of 1 K the timescale at which energy escapes to the substrate is $\tau_{hs} = 61\,\mathrm{ns}$. This is much longer than τ_{el} and shows that the cooling of the hot region due to its expansion is more effective than its loss of thermal energy via the coupling to the substrate.

Since τ_{el} describes the temperature of the hot region at a certain time, whereas τ_{hs} is a coupling time constant calculated for a fixed environment temperature, the comparison between the two would not be worth much. Luckily in this special case both time constants have the same temperature dependence $\propto T^{-2}$ and the ratio between them is the same for all temperatures of the hot region.

By these rough estimates one may expect that less than 10 per cent of the energy deposited in the SPT film escape to the substrate by the thermal coupling g_{ea}. Thus energy transmitted to the substrate, being lost or re-absorbed plays a minor role.

2.4 Relaxation Processes Inside the Absorber Crystal

In this section the energy propagation in the absorber crystal will be discussed. It covers homogenisation processes of phonons in the crystal as well as the absorption of an inhomogeneous phonon distribution in the SPT film.

2.4.1 Phonon Propagation in the Absorber

A particle interaction in the absorber crystal produces non-thermal phonons in a very small volume at the impact spot. The phonons spread in the absorber crystal and homogenise their spatial distribution on a timescale τ_{hom}. τ_{hom} is given by the velocity and the mean-free-path of the phonons. Phonon scattering takes place in the crystal volume, with a scattering length l_0, and at the crystal surface. If the smallest crystal dimension (thickness) d_{min} is smaller than the volume scattering length, $d_{min} \ll l_0$, the effective mean-free-path l_{eff} can be approximated by an equation given by J. J. Thomson [Fuc-38],

$$l_{eff} = \frac{d_{min}}{2}(\ln \frac{l_0}{d_{min}} + \frac{3}{2})\,. \tag{2.41}$$

In crystals of reasonable quality and with dimensions as used in this work, the mean-free-path is dominated by surface scattering. This is the case for thermal phonons as well as for non-thermal phonons after the initial phase of quasi-diffusive propagation.

In our clean sapphire crystals the mean-free-path for scattering in the crystal volume l_0 is usually larger than the crystal dimensions. Then l_0 in eqn. (2.41) must be replaced by the largest crystal dimension d_{max}, and l_{eff} is an upper limit of the scattering length in the crystal.

l_{eff} is limited by the value of d_{min}. If the absorber has a cube-like geometry such that it has similar dimensions in all directions, then d_{min}, l_{eff} and d_{max} are of the same order of magnitude. The phonons can propagate through the crystal ballistically in any direction. In this case the homogenisation can be approximated by the crystal's longest dimension d_{max} and the phonon speed-of-sound which is equal to the phonon group velocity $v_s = v_g$,

$$\tau_{hom} = \frac{d_{max}}{v_s} \qquad \text{(ballistic case)}. \tag{2.42}$$

For example in the case of a $20 \times 10 \times 5\,\mathrm{mm}^3$ Al_2O_3 crystal with a speed-of-sound of approximately $v_s \approx 10^4\,\mathrm{m/s}$, the homogenisation time is $\tau_{hom} \approx 2\,\mu\mathrm{s}$.

If the phonons are not able to travel through the whole crystal without being scattered, $l_{eff} \ll d_{max}$, the homogenisation becomes a diffusive process. This is

the case if the scattering length l_0 gets short (for example in a dirty or a defect-rich crystal), or at high temperatures when phonon–phonon scattering reduces $l_0 \propto T^{-1}$. It takes place as well if the absorber's aspect ratio d_{max}/d_{min} shifts towards a longish shape, as occurs for example if the absorber crystal is a thin substrate die. In the diffusive case the homogenisation time is proportional to a diffusion constant D and to the square of the longest dimension d_{max},

$$\tau_{hom} = \frac{d_{max}^2}{D} \quad D = \frac{1}{3} v_s \cdot l_{eff} \qquad \text{(diffusive case)}. \tag{2.43}$$

For a $20 \times 10 \times 0.5\,\mathrm{mm}^3$ absorber the time constant would be $\tau_{hom} = 92\,\mu\mathrm{s}$.

Trying to take advantage of the fast energy homogenisation in the ballistic case would suggest a cube- or sphere-like absorber geometry. On the other hand the life time of non-thermal phonons is $\tau_n \propto V_a$ which demands for a small absorber volume. If, aiming for a small substrate volume, a thin substrate shall be used as absorber, in which the energy is homogenised diffusively, measures must be taken to quickly collect the phonons independent from their homogenisation in the absorber.

2.4.2 Structured Thermometer Films

If a thermometer film is of a shape such that its life-time of non-thermal phonons τ_n of eqn. (2.4) is shorter than the homogenisation time τ_{hom}, then the phonons in the absorber crystal are not equally distributed during the calculated life time τ_n. This may result in a variation of the signal shape of the detector. The pulse shape and the signal rise time may vary depending on the distance between the impact spot of a particle and the thermometer film. Especially variations of the rise time reduces the achievable time resolution of the detector.

A way to overcome this problem is to increase the thermometer film to the same size as the detection area which is on the backside of the absorber crystal. But increasing the film also increases its heat capacity and reduces the signal amplitude. To not increase the total area of the film when spreading it out over the whole detection area, the film may for example be structured with a certain pattern of holes or strips such that the heat capacity remains unchanged.

As a consequence, inhomogeneities in the detector signal may arise dependent on the location of the impact event relative to the film structures. For making a simple consideration, assume a particle impinging at the absorber surface below a structured film as shown in figure 2.6. It creates a cone of non-thermal phonons in the crystal. Not much is known about the angular propagation of high-energetic phonons in such a case. It can for example be uniform, have certain directions of precedence, or may have an angular distribution for example similar to Lambert's cosine law in the case of a radiant black body. Let's regard a cone with an opening angle of at 90 degrees as sketched in figure 2.6. Then a dependence of the impact

position is reduced if the structure size is of the order of or smaller than the thickness of the absorber crystal.

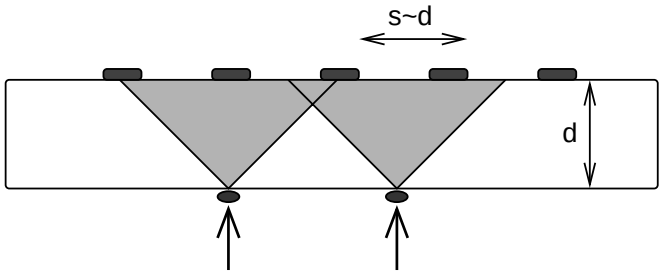

Figure 2.6: A structure size $s \sim d$ washes out inhomogeneities due to different impact places of particles. No matter where the impact occurs, always the same film area is illuminated with phonons.

In a thin normal-conducting metal film the current density is uniform in the whole cross section of the film. In a thin superconducting film the current is distributed non-uniformly. Since the magnetic field is expelled from the superconductor, the flux lines are in parallel to the surface of the film. At its edges, the flux lines are bent and the current density is increased according to $\overrightarrow{j} = rot(\vec{H}) - \dot{\vec{D}}$. For films of a thickness h (see figure 2.7) similar to the superconductor's penetration depth λ and a width w greater than λ, so that $wh \gg \lambda^2$, the current density close to the film edges $\pm w/2$ follows the distribution [Rho62]

$$j_y(x) = j_y(\frac{w}{2}) e^{-\frac{h(\frac{w}{2}-|x|)}{a\lambda^2}} \qquad (\frac{w}{2} - \frac{a\lambda^2}{2h} < |x| < \frac{w}{2}) \tag{2.44}$$

where a is a constant close to 1. λ is the penetration depth of magnetic field into a superconductor as given by the BCS theory [Bar57]. Due to this inhomogeneous current distribution the current response of an SPT due to a particle interaction

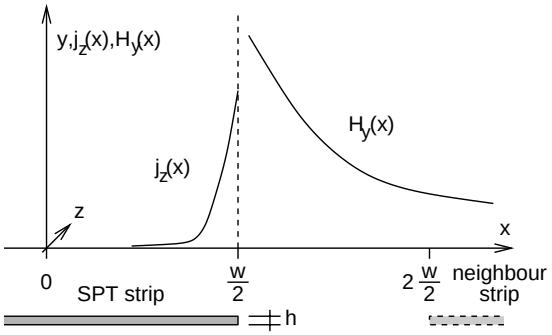

Figure 2.7: Current distribution in, and magnetic field on the x-axis outside a superconducting the film.

close to the edges of the film will be different from that of a particle interaction in the centre of the film.

The inhomogeneity in current response can be reduced if the SPT film is made of several strips instead of one contiguous film. A fraction of the total current flows through each of the strips. Inside each strip the current distribution is still inhomogeneous, but making the strips small enough so that a particle interaction heats up the strip uniformly across its cross section, minimises the effect of inhomogeneous current distribution. A strip should have a width in the order of the thickness of the absorber crystal.

If two superconducting strips are brought close together, their magnetic fields interact and influence their current distribution vice versa [Maw01]. The smaller their distance, the more the current and magnetic field distributions approach the situation of one closed strip of twice the width. The magnetic field $H_y(x)$ on the x-axis of a single strip, outside the strip ($x > w/2$), scales with $|H_y(x)| \propto \pi[(2x/w)^2 - 1]^{-1/2}$ (figure 2.7). Thus neighbouring strips need to be in a distance such that the interaction of their magnetic fields is not too high. A distance between two strips of $\approx w$ should keep the interaction between two neighbouring strips low enough.

Chapter 3

Operation of Cryogenic Detectors in a Mass Spectrometer

3.1 Parasitic Thermal Radiation

In the application of cryogenic calorimeters as detectors for mass spectrometry an entrance in direct line-of-sight to the detector must exist in the cryostat. For this reason the detector is directly exposed to thermal radiation from hot parts of the mass spectrometer. Part of the radiation will be absorbed by the detector. Due to the weak thermal coupling it may be heated up significantly, preventing the SPT film from reaching its transition temperature. To operate the cryogenic calorimeter under these conditions, the amount of thermal radiation being absorbed in the detector must be controlled carefully. Therefore it is important to know the amount of introduced total radiation power, the spectral distribution and the absorption coefficient of the detector in the relevant spectral range.

3.1.1 Thermal Radiation Introduced into the Cryostat

The total heat power emitted into the cryostat through an aperture of the area A is given by the Stefan-Boltzmann law:

$$P_{em} = \frac{2\pi^5 k_B^4}{15c^2h^3} \cdot A \cdot T^4 = \sigma \cdot A \cdot T^4 \qquad \sigma = 5.67 \cdot 10^{-8} \frac{\mathrm{W}}{\mathrm{m^2K^4}}\,. \tag{3.1}$$

σ is the Stefan-Boltzmann constant and T the temperature. So the major influence on the total heat power can be achieved by a reduction of the outside temperature. In the mass spectrometer setup this is done by cooling all parts in the line of sight of the detector by liquid nitrogen to a temperature of 80 K–100 K. Additionally the aperture diameter needs to be chosen as small as possible.

The spectral energy density of a black body $u_\nu = dE/d\nu$, $u_\lambda = dE/d\lambda$ is

given by Planck's law:

$$u_\nu(\nu,T) = \frac{8\pi\nu^2}{c^3}\frac{h\nu}{e^{\frac{h\nu}{kT}}-1} \quad \Leftrightarrow \quad u_\lambda(\lambda,T) = \frac{8\pi hc}{\lambda^5}\left(e^{\frac{hc}{\lambda kT}}-1\right)^{-1}, \tag{3.2}$$

with the frequency $\nu = c/\lambda$, the wave length λ and the speed-of-light c.

The distribution reaches its highest energy density at the wave length λ_{max} given by Wien's law:

$$\lambda_{max} = \frac{b}{T} \qquad b = 2.898 \cdot 10^{-3}\mathrm{m}\cdot\mathrm{K} \tag{3.3}$$

and shifts inversely proportional with the temperature. b is Wien's constant. For room temperature this maximum lies in the mid infrared spectral range. For the temperature of liquid nitrogen ($T = 77\,\mathrm{K}$) it is $\lambda_{max} = 38\,\mu\mathrm{m}$, thus in the far infrared. The frequency where the energy density drops to 10% of the maximum of the Planck distribution ($u(\lambda_{10\%},T) = 0.1u(\lambda_{max},T)$) already reaches the microwave spectrum.

To decrease the radiation load on the calorimeter, the solid angle element of the detector relative to the entrance aperture can be reduced quadratically by increasing the distance between the aperture and the detector. In the cryostat used for this project this is realized by a snout which is cooled to liquid helium temperature ($T = 4.2\,\mathrm{K}$). The entrance hole through which heat radiation of liquid nitrogen cooled surfaces enters the cryostat is in a distance of 60 cm to the detector. A detailed description of the cryostat is given in sec. 4.1.

3.1.2 Radiation Absorption in the Cryogenic Calorimeter

To estimate the radiation power actually absorbed in the cryogenic calorimeter one has to know the infrared absorption of the substrate and the metal film.

Dielectrics

In crystals with one atom per Wigner-Seitz cell and in covalent crystals the only excitation present is an oscillation of the valence electrons against the quasi-static ion bodies. This electronic polarisation oscillation occurs at frequencies in the order of $\omega_1 = 10^{16}\,\mathrm{Hz}$ in the ultraviolet and does not contribute to infrared absorption.

If the crystal is an ionic crystal, ionic polarisation oscillation adds to the electronic polarisation oscillation where the anionic ions oscillate against the cationic ions in the lattice cell. This oscillation takes place in a longitudinal mode with the frequency ω_L and a transverse mode with the frequency ω_T. ω_L and ω_T usually have values of $\mathcal{O}(10^{13}-10^{14}\,\mathrm{Hz})$ in the infrared. They are connected by the Lyddane-Sachs-Teller relation

$$\frac{\omega_L^2}{\omega_T^2} = \frac{\varepsilon(0)}{\varepsilon(\omega_v)} \tag{3.4}$$

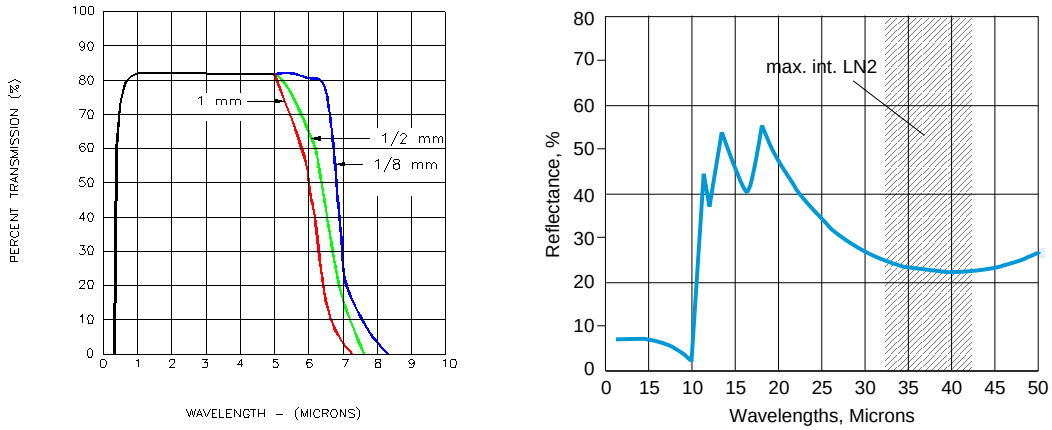

Figure 3.1: Typical transmission curve (left) and reflection curve (right) of infrared radiation in Al_2O_3 of several thicknesses.

with $\varepsilon(0)$ the dielectric function for the static case, and $\varepsilon(\omega_v)$ the dielectric function for frequencies far above ω_L with $\varepsilon(\omega \gg \omega_L)$ approaching a constant value. This is already the case at visible frequencies ω_v.

The ionic polarisation oscillation is a coupling of electronical and mechanical lattice oscillations and appears as polaritons. Due to the coupling, the oscillation splits into two branches, one appearing at frequencies below ω_T and one appearing at frequencies above ω_L. In the frequency range $\omega_T < \omega < \omega_L$ no excitation is possible and no absorption takes place. At frequencies slightly below ω_T an absorption maximum occurs. This is the resonance frequency of the (undisturbed) transverse-optical phonons.

At very low frequencies between zero frequency and the UHF radio frequency range an orientation oscillation may occur in ionic crystals where anions and cations truly change place. Since the frequencies are too low the orientation oscillation is not of importance for infrared absorption.

Al_2O_3 has its ionic polarisation oscillation at 13.5 μm. As shown in figure 3.1, the transmission of infrared radiation is almost 85% for wave lengths below 5 μm, above it drops to zero. The reflectance for $\lambda < 10\,\mu$m is below 10% and increases to $\sim$ 50% for $\lambda < 20\,\mu$m. At higher wave lengths is drops again to $\sim$ 25%. Thus there is effective absorption in Al_2O_3 between 5 μm and 10 μm, and above 10 μm half to three-fourth of the radiation power is absorbed. This is exactly the wave length region where the maximum power is emitted by the 77 K thermal radiation.

Metals and Superconductors

In metals a valence band completely filled and a conduction band partly filled with electrons exist. Excitations of electrons from the partly filled conduction

band to higher-energetic states in the conduction band (intra-band transitions) and excitations of electrons in the valence band to the conduction band (inter-band transitions) are possible. Both types of excitations occur at energies around 1 eV corresponding to frequencies in the visible range ($> 10^{15}$ Hz) and above. Far-infrared photons are not absorbed.

The most important excitation, which is also responsible for the brilliance of metals, is the collective oscillation of the free-electron plasma in the conduction band. Its oscillation states are called plasmons. At the plasma oscillation, the electrons are able to follow the oscillations of an electromagnetic wave up to a plasma frequency ω_p. For these frequencies the dielectric function $\varepsilon(\omega < \omega_p)$ is strictly real and negative so total reflection occurs. The electromagnetic wave penetrating the solid is exponentially damped on the length of a penetration depth d. For waves with a frequency $\omega > \omega_p$ the electron plasma can not follow, these waves are transmitted through the metal. The plasma frequency depends on the density N_C of electrons in the conduction band:

$$\omega_p = \sqrt{\frac{N_C e^2}{\varepsilon_0 \varepsilon_{el} m^*}}\,, \tag{3.5}$$

where e is the electron charge, m^* is the effective electron mass, ε_0 the dielectric constant of vacuum and ε_{el} the contribution of the bound valence electrons to the dielectric constant. For all metals the plasma frequency corresponds to an energy $\mathcal{O}(\omega_p) = 10\,\text{eV}$ which is the reason why metals are shiny reflective in the visible spectrum. For superconductors at the transition temperature this argumentation still holds.

Absorption and transmission through a thin superconducting film depend on film thickness and radiation frequency. For frequencies below the plasma frequency, the penetration depth d is [Fis36]

$$d = \sqrt{\frac{2\rho}{\omega \mu_m}} \tag{3.6}$$

with ρ the specific resistance, $\mu_m = \mu_0 \mu$ the magnetic permeability and $\omega = 2\pi\nu$ the angular frequency of the incoming wave. d is the length at which the electromagnetic power of the wave is damped to the $1/e^2$ th part since it is the $1/e$ damping length of the electric and magnetic field.

For the iridium-gold films used in this work the specific resistance was measured to be typically of $\rho = 1.25 \cdot 10^{-8}\,\Omega\text{m}$. With $\mu_m = \mu_0 \mu \approx \mu_0$ the penetration depth is

$$d(Ir/Au) = 1.4 \cdot 10^2\,\text{nm} \sqrt{\frac{10^{12}\,\text{Hz}}{\omega}}\,. \tag{3.7}$$

For the 77 K thermal radiation the frequency with the highest energy density is $\nu_{max}(77\,\text{K}) = 4.7 \cdot 10^{12}\,\text{Hz}$. At this frequency the penetration depth becomes

$d(\nu_{max}) \approx 26\,\text{nm}$, and for the 10% frequency $u(\nu_{10\%}) = 0.1u(\nu_{max})$, which is $\nu_{10\%} = 0.72 \cdot 10^{12}\,\text{Hz}$, the penetration depth becomes $d(\nu_{10\%}) \approx 66\,\text{nm}$. This means that an SPT film with a typical thickness of $d_{film} = 50 - 150\,\text{nm}$ would reflect most of the incoming thermal radiation. Only a few percent of the radiation power would pass through the film and be absorbed in the sapphire crystal. When the film resistance drops as the SPT film gets to its operating temperature, the penetration depth is further decreased.

In summary, mounting the detector in a way that the molecules as well as the parasitic heat radiation hit the SPT film instead of the substrate crystal, is expected to significantly reduce the thermal radiation load.

3.2 Time-Of-Flight Mass Spectrometry

In this section the functional elements of a TOF-MS are discussed. First, the principle of TOF-MS is explained. Second, a specific ion source, the MALDI (matrix assisted laser desorption / ionisation) ion source is introduced and a model of its functionality is presented. After this the mass resolution of a TOF-MS and ways to improve it are discussed. At the end the desired resolution of a detector for high molecule masses is estimated.

3.2.1 Linear TOF-MS

In a TOF analyser the ions' time-of-flight between a source and a detector is measured [Leh96]. A simplified principle of a TOF-MS is shown in figure 3.2. By accelerating ions of the charge state z in an electric potential difference U, they gain the kinetic energy $zeU = E_{pot} = E_{kin} = mv^2/2$ where m and v are the molecule mass and velocity. This means that light ions will fly faster than heavy ions. Thus starting at the same time, light ions will arrive earlier at the detector located at the distance D[1]. The square of the time-of-flight is proportional to the m/z value of the ions. In a simple approximation neglecting the time of the ions in the ion source, the flight time t becomes

$$t = D\sqrt{\frac{1}{2eU}\frac{m}{z}}\,. \tag{3.8}$$

TOF analysers need a pulsed, discontinuous ion beam. For each ion pulse a complete mass spectrum is recorded. Usually $100 - 1,000$ pulses are summed to improve the signal-to-noise ratio.

[1] In TOF-MS the expression "drift tube" is commonly used for the evacuated and force-free time-of-flight analyser tube. Strictly speaking this is wrong since the expression "drift" depicts the directional flow in a field with a constant mean velocity, given by continuous interactions with a stationary background.

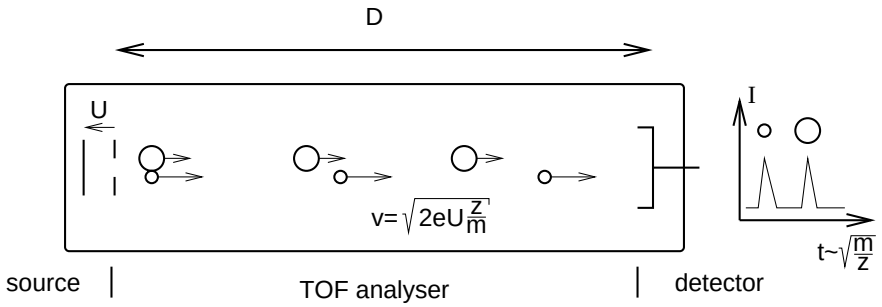

Figure 3.2: Simple scheme of a TOF mass spectrometer. Ions are accelerated in the source to same kinetic energy. Passing through the flight tube, lighter ions reach the detector earlier. The detector records the arrival time.

A widespread used ion source in TOF-MS is the matrix assisted laser desorption / ionisation (MALDI) source. It will be described below. Detectors are Micro Channel Plates (MCP) or similar secondary electron creating detectors. In the present work the conventional detector is replaced by a cryogenic calorimeter.

3.2.2 Matrix Assisted Laser Desorption / Ionisation

In a laser desorption / ionisation (LDI) ion source an analyte substance, fixed on a sample plate, is desorbed and ionised by a pulsed laser beam. The ions are accelerated in an electric field to form an ion beam. Acceleration voltages usually are $10 - 40\,\mathrm{keV}$. The number of analyte substances which are not immediately destroyed by the high energy density of the laser beam is quite limited. Using an additional "matrix" substance as a mediator for the laser power solves the problem, and expands the LDI technique for the use with many other substances. Together with the preparation of the analyte in a matrix substance this ion source is called Matrix Assisted LDI source (MALDI source).

Figure 3.3 displays the mechanical setup of an LDI, respectively MALDI, source. The sample is mounted on a plate in the ion-optical axis of the TOF analyser. The plate is movable to focus the ion optics on a selected spot of a sample droplet. The focused spot is irradiated by a pulsed laser the power of which can be tuned by an attenuator. Laser pulses need to be short ($\sim 4\,\mathrm{ns}$) compared to the ions' time-of-flight. The wavelength may range from the UV [Str94] to the IR [Ber97, Men99]. Generally cheap UV nitrogen lasers ($\lambda = 337\,\mathrm{nm}$) are used.

Additionally, an optical camera is mounted to control the sample positioning. The source also includes several ion-optical elements (not shown in the figure). These are an electrostatical Einzel Lens to collimate the ion beam into the detector plane, and two pairs of electrostatic deflection plates to direct the beam onto the detector.

For MALDI the analyte molecules are integrated in the lattice of a poly-

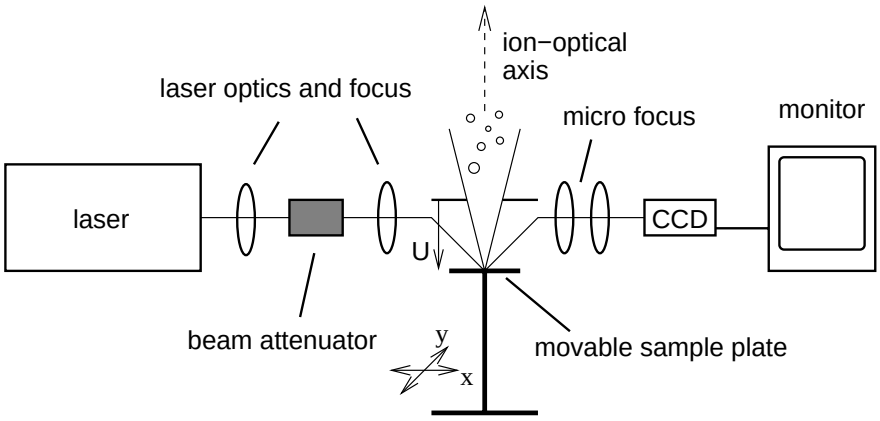

Figure 3.3: Scheme of a MALDI source. The sample is illuminated by a pulsed laser beam of tunable power. Ions are extracted from the source and accelerated by the voltage U. A CCD camera is mounted for optical control.

crystalline matrix substance. Usually, the proportion of matrix molecules to analyte molecules is $10^3 - 10^4$, and almost each analyte molecule is individually surrounded by the matrix molecules. The matrix substance is chosen such that it effectively absorbs the laser radiation, and that it chemically fits the analyte. During the MALDI ablation, all matrix molecules surrounding an analyte molecule are evaporated and a detached intact analyte molecule is left over. Commonly used matrices for MALDI of proteins are 2,5-dihydroxybenzoic acid (DHB), sinapic acid, 4-hydroxybenzoic acid (HBA) and 3-hydroxypicolinic acid (HPA).

Understanding the Desorption /Ionisation Process

The MALDI principle has been invented in the mid eighties of the past century independently by two groups in Germany and Japan [Kar87, Kar88, Tan88]. Initially it was called matrix-UV-LDI. The idea of using a matrix appeared to be the breakthrough for the known LDI technique. It was then quickly shown that with MALDI it was possible to analyse molecules with masses up to 250 kDa without destroying them [Kar89a, Kar89b], and MALDI TOF-MS showed a sensitivity competitive to other MS like Plasma Desorption MS or Fast Atom Bombardment MS [Tan88, Kar89c]. Nowadays MALDI sources are found in a large number of commercial mass spectrometers.

Despite its widespread use, the processes underlying the matrix assisted desorption / ionisation are still poorly understood. A number of ion formation models are presented in [Zen98]. A common understanding exists of the initial laser absorption process in the matrix molecules which mediate the laser power

and thereby the evaporation of a plume of hot material from the sample surface. Then several ways of creating "primary ions", both from matrix and analyte, are suggested, and different ways of energy transfer leading to "secondary ionisation" reactions of analyte molecules in the MALDI plume are considered.

Away from these detailed considerations about energy and charge transfer, a quite descriptive, yet comprehensive model was suggested by Karas et al. in [Kar00]. Several properties of the MALDI ion formation are generally stated:

- Essentially only single charged ions are observed.
- Positive as well as negative ions are observed depending on the polarity of the acceleration field.
- Mass spectra of matrix substances themselves show distinct special features, e. g. in negative-ion mode strong electronic signals and matrix-hydrogen adducts are observed, pointing to the intermediate formation of hydrogen free radicals.
- Despite the large excess of matrix molecules, under certain conditions like e g. low laser fluency mainly only analyte molecules are observed.
- For a wide range of laser wavelength (IR to UV) the obtained mass spectra look very similar.
- Analyte ions are excited and have a tendency to break up either in the source (prompt fragmentation) or in a metastable manner during flight (post-source decay).
- Singly charged multimers[2] are often observed.

Based on these observations, Karas et al. developed their model which shall be summarised briefly in the following paragraph.

By the arrangement of matrix, acid and contaminant ions around the analyte, the pH environment of the analyte molecule is assumed to be conserved during the sample preparation. This is important not to destroy the biological sample. Each analyte molecule is fully embedded in a "solid solution" in matrix molecules and is not in touch with neighbouring analyte molecules. The optical power of the laser is absorbed in the matrix which leads to a local overheat and a "sudden explosive phase transition" of sample material. Highly excited clusters are desorbed, containing few analyte ions embedded in matrix molecules. Initial ionisation is considered to appear during cluster formation, since the cluster separation is likely not to be strictly charge neutral: ions carrying the counter-charges providing the pH environment may be missing, so a cluster may carry one

[2]compound of two or more weakly bound single molecules (monomers)

or more excess charges. Neutral clusters may become charged due to e. g. photo ionisation. Due to their excitation, the clusters tend to break into smaller pieces and to evaporate neutral matrix molecules, until one neutral or single charged analyte molecule is left. Highly charged clusters loose charge by the evaporation of protonated matrix molecules or by electron capture, both driven by Coulomb forces. In the end the analyte molecule is mainly neutral or singly charged as observed in the MALDI mass spectra.

3.2.3 Limits of Mass Resolution

In the TOF-MS the ion beam produced in the source must be focused on the detector in a way that all ions with the same mass arrive after the same time-of-flight. The smearing of the time-of-flight defines the mass resolution achievable with the device. Using a MALDI source the ions' arrival time at the detector is exact only if all ions are created at the same time, at the same electrical potential i. e. at the same coordinate on the ion beam axis, and with the same initial velocity.

In a real MALDI source neither of these conditions is strictly fulfilled. The complicated MALDI desorption and ionisation process has a finite duration, starting with the onset of the laser shot, and continuing until the last molecules are ionised. This introduces a certain distribution in starting time. The ions will appear at different starting points, since they are ablated from layers of different depth in the sample droplet. Molecules might as well cross a certain electric potential uncharged before they finally get ionised. This leads to an initial spatial ion distribution. The starting place of an ion in the electric potential is of importance as the truly passed electric potential defines the final kinetic energy of the ion. Lastly, due to the high and sudden energy impact by the laser, each ion is provided with an individual, not negligible initial velocity. The last two effects lead to an initial ion energy distribution. All these effects lead to a broadening of the arrival time at the detector place for ions with identical m/z value [Boe92].

Focus in Space: Electric Field Geometry

A certain point on the ion beam axis exists at which identical ions with different starting points pass at the same time [Boe92]. Ions which start at a lower potential in the source pass through a shorter electric field and gain a lower kinetic energy compared to ions which start at a higher potential but pass through a longer field. The latter ones leave the source later but gained higher kinetic energy. At a certain point in the field-free region the slow ions are overtaken by the fast ions. A simple ion source with one electric field for ion extraction is shown in figure 3.4(a). There is a point D where ions starting around a point s_0 in first

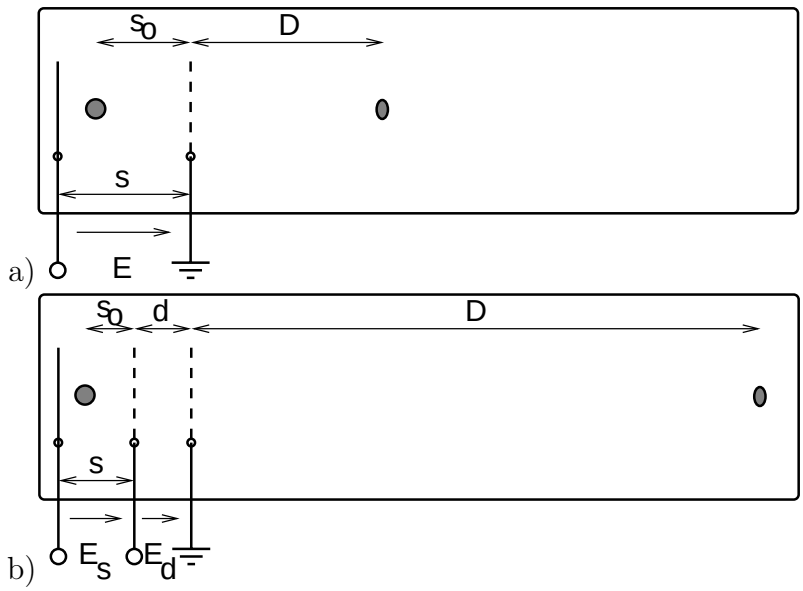

Figure 3.4: Illustration of the space focus point in simple (a) and double-stage (b) extraction MALDI sources.

order in space all pass at the same time. This point is at [Boe92]

$$D = 2s_0\,. \tag{3.9}$$

At this point D the detector should be placed. This position is called space focus as in first order ions with different starting points around s_0 are focused here. An energy distribution caused by different initial velocities is not affected by the space focus.

With the simple setup of figure 3.4(a) there is only the length of the ion source s, to which the parameter s_0 is closely related, which allows to tune the space focus. The achievable distances D are too short for suitable flight lengths since the differences in molecule flight times are indistinguishabley small. This problem can be overcome if the electric field is not constant but has a suitable gradient along the ion beam axis. Even the simplest case, of two different fields E_s and E_d in two regions s and d, as illustrated in figure 3.4(b), yields a significant improvement [Wil55]. Then the ratio E_d/E_s is an additional, non-geometric parameter which can be used to tune the space focus to a desired point. Regarding some boundary conditions, the space focus of this so-called "double stage extraction" MALDI source is given by [Wil55]:

$$D = 2s_0 k_0^{\frac{3}{2}} \left(1 - \frac{1}{k_0 + k_0^{\frac{1}{2}}} \frac{d}{s_0}\right)\,. \tag{3.10}$$

s_0 is again the average position of the ions in the source, and k_0 is given by

$$k_0 = \frac{(s_0 E_s + dE_d)}{s_0 E_s} \,. \tag{3.11}$$

Focus in Energy: Time-Lag Focusing

To narrow the energy distribution caused by the distribution of initial velocities, a method of varying the electric field E_s in time was developed [Fra97, Wil55]. By the energy focus, all ions of the same type but with a distribution of initial energies pass a distinct point at the same time. Similar to applying an electric field gradient along the ion beam axis for improved space focus, a variation of $E_s(t)$ in time yields a focus in energy. Keeping $E_s = 0$ until a delay time τ and then switching it on to its operational value already yields a focus. During such delayed extraction (DE) [Bar97] or time-lag focusing (TLF) the ions will pass certain distances in the source, according to their speed. If τ is chosen correctly, when switching on E_s the ions have reached places in the electric field where their kinetic energy just equals the potential energy they "missed" while the electric field was switched off. After acceleration all ions will achieve the same total energy. The geometrical setup is still the one of figure 3.4(b).

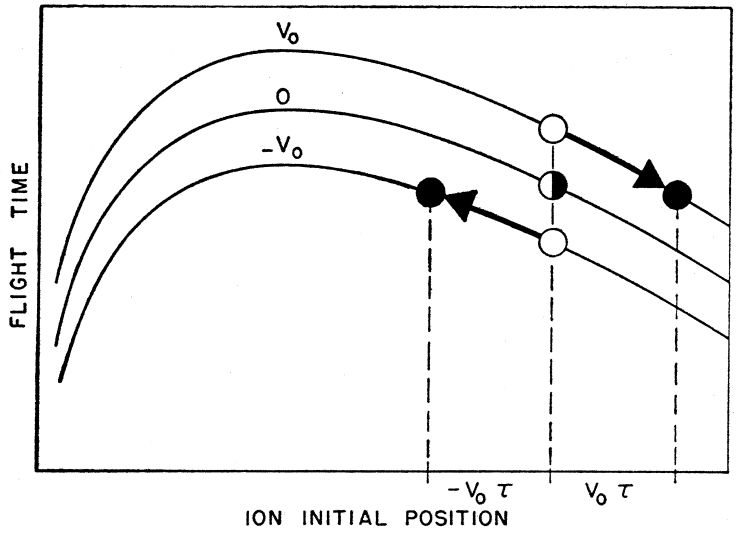

Figure 3.5: Curves of flight time versus initial ion position. During the time τ the ions have moved to the positions marked with black circles. If the electric field U_s is now switched on all ions will have the same time-of-flight. Figure taken from [Wil55].

The delayed extraction is illustrated in figure 3.5. The curves show the ions' time-of-flight T depending on their starting position s_0 in the source, for ions of

different initial velocities 0 and $\pm v_0$. Ions with different velocities 0 and $\pm v_0$ may be created at a place, marked by the white circles. As long as the acceleration voltage is switched off ($t < \tau$) their position in the source changes and they move along their flight time curves according to their initial velocity. When the electrical field E_s is switched on at the time τ, the ions have reached the positions marked by the black circles. As can be seen, if τ is chosen correctly, all ions have the same total time-of-flight T. T is given by

$$T = 1.02 \left(\frac{m}{2ze(s_0 E_s + dE_d)} \right)^{\frac{1}{2}} \left(2k_0^{\frac{1}{2}} s_0 + \frac{2k_0^{\frac{1}{2}}}{k_0^{\frac{1}{2}} + 1} + D \right) \tag{3.12}$$

and is equal to the time-of-flight of an ion starting at the position s_0 with zero velocity. k_0 is given by eqn. (3.11). The energy focus is achieved by setting τ to

$$\tau = -1.02m \left(zeE_s \frac{dT}{ds} \right)^{-1} . \tag{3.13}$$

m is the ion mass, which means τ is not valid for all masses but must be selected to fit to the mass range [Wil55] of interest. Typical values of τ are between several hundred ns and few μs.

As the space focus point from above is given in a first order approximation of the ion starting point, it still slightly depends of the initial starting point. If the starting points are very widespread, the space focus will be smeared out as well. Since the ions are travelling through the source with different velocities for the time τ at TLF, the gain in energy focus is paid with a loss in space focus. A compromise has to be made and the best overall focus point needs to be found somewhere between space focusing and TLF energy focusing.

3.2.4 Ion Reflectors: Reflectron-TOF

Another way to improve the total mass resolution of a TOF-MS is to separate the space focusing from the energy focusing (as present in case of TLF). This can be done by inserting an ion mirror into the ion flight path. An ion mirror consists of a one or more stage electric field, similar to the ion source. Its electrical potential must be slightly higher than the acceleration potential in the ion source so that all ions are stopped and reflected in the mirror. A reflectron TOF (reTOF) mass spectrometer is sketched in figure 3.6. The ion beam is slightly rotated out of the optical axis of the mirror such that the ion beam can be focused on the detector.

The idea of the ion mirror is that ions with high kinetic energy penetrate deeper into the electric field of the mirror than ions with less kinetic energy. The high-energetic ions' trajectories become longer than the trajectories of the lower-energetic ions. They therefore remain in the mirror for a longer time. This leads to a negative time-of-flight dispersion inside the mirror. If the geometry and the

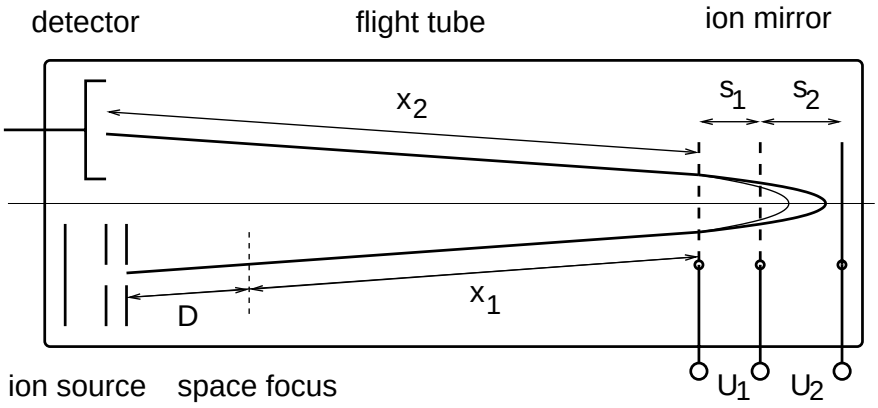

Figure 3.6: Scheme of a reflectron TOF-MS

electric field strengths are chosen properly this negative dispersion can be tuned to cancel the positive time-of-flight dispersion of the field-free regions. Since the penetration depth only depends on the ion energy and not on its m/z value, the mass resolution is not affected by the mirror [Kar72].

If the ion mirror is equipped with one electrical field of voltage U_1 a first order correction of the ions' time-of-flight can be applied in terms of ion energy, since the retention time of ions can be expanded to terms of $T_D \propto \sqrt{U_1}$. If an additional field of voltage U_2 is introduced a second order correction in ion energy can be applied. Such mirrors are called two-stage ion reflectors. By choosing the ratio U_1/U_2 the focus can be tuned to the distance $X = x_1 + x_2$ of figure 3.6. The condition for energy focus in the two-stage ion mirror is given by the equations [Mam73]

$$U_1 \approx 0.7U_0 \quad U_2 \approx 0.45U_0 \quad s_1 \approx 0.008X \quad s_2 \approx 0.06X\,, \tag{3.14}$$

where $zeU_0 = ze(U_{min} + U_{max})/2$ is the average energy of the ions in the field-free flight space one wishes to focus. The segmentation of X to x_1 and x_2 is not relevant which means one is free to choose the source distance different from the detector distance as long as the total X fulfils the equations (3.14).

As displayed in figure 3.6 the ion reflector is aligned such that it projects the space focus D of the ion source onto the detector place. It provides an energy focus to the ion beam. The distance D is tuned by adjusting the fields of the ion source to provide a space focus. In this point of view the space focus generated in the ion source gets separated from the energy focus generated by the ion reflector. Both are adjustable separately.

The ion reflector does not affect a spatial distribution of ions. Since it compensates the dispersion in the field-free region, it allows to mirror an ion plume with a distinct spatial distribution to a point in a distance X without increasing the spatial distribution. By this, the total ions' time-of-flight is increased but the distribution in time given by the spatial distribution is not. Consequently the

mass resolution will be improved.

Another point of view is as follows: Looking at the setup of a mirror with a two-stage electrical field, it is equivalent to the two-stage extraction in the ion source. Thus it is obvious that the mirror can be treated as an inverted source. The entrance space focus x_1 of the mirror shall be identical with the space focus point D of an ion source. Then ions which appear at a point in time at the ion sources' space focus with different energies will travel to the mirror and will be stopped therein. Due to their different energies they will be stopped at different turn-around points. The ion distribution from the source is so to speak mapped to the mirror [Boe92]. Now the mirror acts as an ion source and projects the ions to its output space focus x_2 where the detector is placed. Thereby the flight distance and the total time-of-flight is prolonged by the distance X whereas the absolute error in time is kept constant since the reflectron setup is dispersion-less. Thus the relative resolution in time-of-flight is improved by the ion mirror.

In our reTOF-MS two ion mirrors are mounted. The first mirror is built as a two-stage mirror. It is used for energy focusing. The second mirror is cooled with liquid nitrogen and is built with one "short" electric field: entrance grid and back electrode are close to each other, the electric field is stronger than in the first mirror. The strong electric field causes a short retention period and thus a low dispersion in the second ion mirror. The second ion mirror is intended for ion reflection only. Focusing of the ion beam on the detector plane is tuned by the first ion mirror. The exact setup of the instrument is described in sec. 4.3.

3.2.5 Mass Resolution Aimed at

The desired mass resolution of the detector of a TOF-MS is given by the intrinsic broadening of the mass signal to be measured. There is no need to apply a detector with a mass resolution better than the uncertainty of the mass signal itself. Besides the mass broadening provided by the MALDI-TOF setup, each molecule differs in mass due to the statistical fluctuations of its natural isotope distribution [Leh96]. In the low mass range with few atoms building the molecules, the isotope distribution in molecules of the same substance can be resolved. However, already at masses above a few kDa the isotope distribution changes from a set of individual peaks into one indistinguishable mass peak with a natural broadening.

Considering for example a BSA molecule of $m_{BSA} = 66.431\,\mathrm{kDa}$ mass, its mass signal will drop to 5% of its peak value within a window of $\Delta m = 30\,\mathrm{Da}$ [Dor90]. A common definition of mass separation in MS is the so-called 10%-valley criteria which means that two mass signals of same height are assumed to be separable if the signal intensity between the peaks drops to 10% of their maximum value. According to that definition BSA would be separable from another substance if the mass difference between them is at least 30 Da. In our TOF-MS the total time-of-flight of BSA is about $t_{BSA} \approx 600\,\mu\mathrm{s}$. The time-of-flight is related to the ion mass by $t = a \cdot \sqrt{m}$. For our TOF-MS it was experimentally found

that $a = 2.33\,\mu\text{s}/\sqrt{\text{kDa}}$. With this relation, a broadening in mass of $\Delta m = 30\,\text{Da}$ leads to a broadening in time-of-flight of $\Delta t = 0.136\mu\text{s}$. This is the time resolution aimed at for the cryogenic detector being developed in this project.

With the detector's time resolution being fixed for all masses, the relative mass error decreases with increasing molecule mass. Since the absolute mass error $\Delta m|_m$ at a mass m given by

$$\Delta m|_m = \frac{2}{a}\sqrt{m}\Delta t \tag{3.15}$$

increases with $\sqrt{m}$, the relative mass error

$$\left.\frac{\Delta m}{m}\right|_m = \frac{2}{a}\frac{1}{\sqrt{m}}\Delta t \tag{3.16}$$

drops with $1/\sqrt{m}$ as the molecule mass rises. So with a fixed time resolution Δt, the relative mass resolution improves for heavier molecules.

Chapter 4

Experimental Setup

In this chapter, the experimental setup of the TOF mass spectrometer will be described. An overview of the components is displayed in figure 4.1. The mass spectrometer is made up of a tube containing TOF analyser and MALDI source. An adiabatic demagnetisation refrigerator (ADR) containing the cryogenic detector is attached to it. Additionally some timing and data recording equipment is installed.

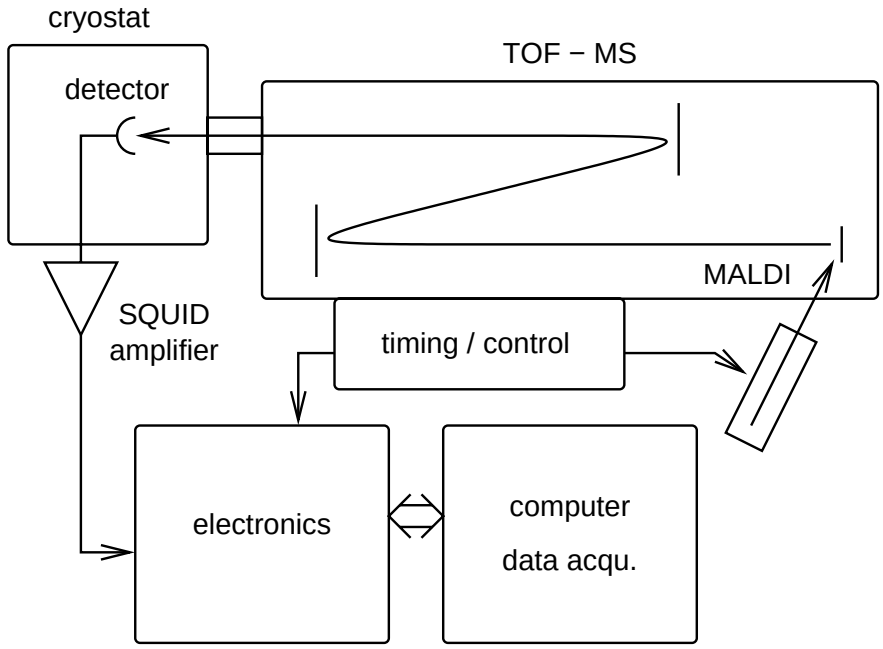

Figure 4.1: Experimental setup of the time-of-flight mass spectrometer setup with a cryogenic detector in a cryostat.

The description of the setup will start with the cryostat. The principle of the ADR will be described, and the heat load due to thermal radiation from the MS

through the input snout connecting the cryostat to the MS will be discussed in detail. This point turned out to be of central interest.

The mounting of the cryogenic detector in the cryostat and in the ion beam axis completes the description of the cryogenic part of the setup. The description of the detector itself is subject of the next chapter.

Next, the TOF-MS is described in detail, followed by a section about the methods of the MALDI sample preparation.

The measurement electronics are described in the following section. The measurement circuit and the SQUID readout are explained in detail. The measurement circuit is similar to the one used in the CRESST experiment [Bru93, Uch01]. Of particular interest is the SQUID and its readout electronics. A considerable effort was put in achieving a high-bandwidth, low-noise setup.

The chapter is completed by an overview of the data acquisition and the on-line and off-line data analysis.

4.1 Cryostat

The cryostat, containing the cryogenic detectors, is an Adiabatic Demagnetisation Refrigerator (ADR). It reaches a base temperature of 34 mK and provides a 4.2 K thermal radiation shield for the cryogenic detector.

A functional sketch of the cryostat is shown in figure 4.2. It was manufactured by the company CSP Cryogenic Spectrometers based in Ismaning near Munich. The speciality of this device is a snout of 45 cm length. It consists of three concentric tubes, of which the outermost holds the vacuum. The innermost tube and the tube in between are connected to the liquid helium reservoir and the liquid nitrogen reservoir, respectively. The molecules enter the cryostat via the snout which is attached to the mass spectrometer at the end of the time-of-flight path. As will be explained in sec. 4.1.2 below, the design of the snout controls the heat load on the detector surface due to thermal radiation from the mass spectrometer.

The cryostat is connected to the mass spectrometer via a valve, which allows to separate the vacua of spectrometer and cryostat. The whole cryostat is mounted on rails so that it can be moved towards the mass spectrometer along the axis of the ion flight path. This is used for moving the liquid nitrogen shielded part of the snout through the connection valve between cryostat and mass spectrometer, into a socket which is liquid nitrogen cooled as well, inside the mass spectrometer. So the whole line-of-sight from the detector inside the cryostat to the liquid nitrogen cooled ion reflector in the mass spectrometer is surrounded by a shielding at liquid nitrogen temperature, and no room temperature radiation can enter this shield. The rails also make it possible to move the cryostat away from the mass spectrometer and disconnect it for maintainance.

Power supplies, a Picowatt AVS-47 AC resistance measurement bridge and

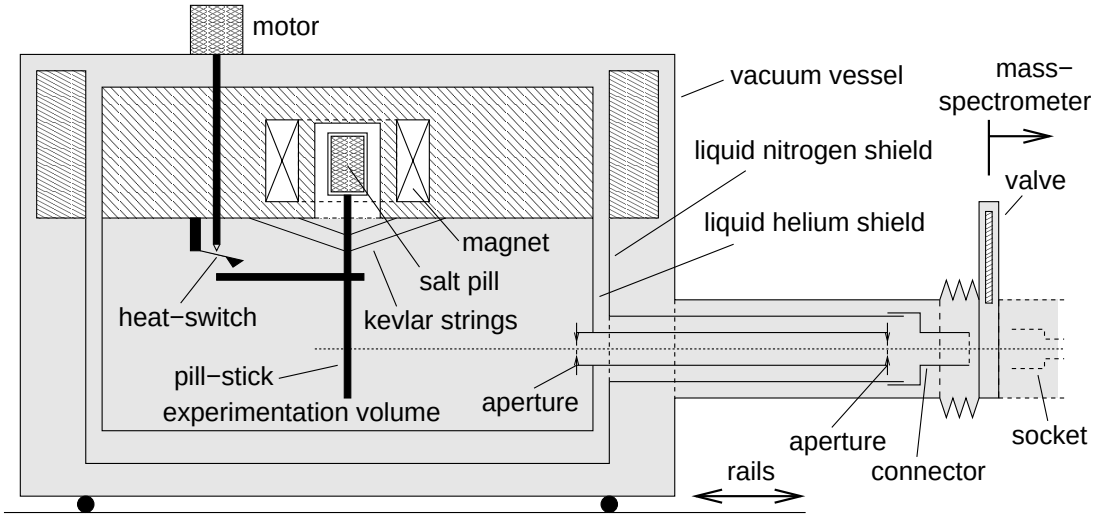

Figure 4.2: Sketch of the cryostat used with the mass spectrometer. It is an adiabatic demagnetisation refrigerator and is fitted with a liquid nitrogen and liquid helium cooled snout as the entrance for the molecules to be detected. Snout and ADR are described in the text.

other measurement electronics are placed in a 19" rack and controlled by a PC. With the resistance bridge it is possible to connect up to 8 thermometer channels. All data related to cryostat operation is recorded with the PC, and it allows fully automated cool-down, operation and temperature stabilisation.

4.1.1 Principle of Adiabatic Demagnetisation Refrigerators

To reach temperatures in the range of some tens of mK, nowadays two types of machines are well-developed and commonly in use. The one is the ^{3}He / ^{4}He Dilution Refrigerator, and the other is ADR. The advantages of the ^{3}He / ^{4}He Dilution Refrigerator are its continuous process, which allows to run such a cryostat for theoretically unlimited time, and its typically much higher cooling power. The ADR has only limited cycle lifetime after which the process of cool-down has to be redone. On the other hand, the ADR is simpler in its setup and does not need a complicated gas handling system. Also the handling of the whole cryostat gets much easier this way.

Depending on the transition temperature of the cryogenic detector, the ADR cycle life time may be up to two days for a typical operating temperature of 100 mK. Cycling may be done automatically overnight. Additionally handling is simplified and reliability is improved compared to a Dilution Refrigerator.

The heart of the ADR cryostat is a paramagnetic salt pill mounted in the centre of a magnetic coil as shown in figure 4.2. The salt pill is mounted on a copper stick, the pill-stick, which sticks out of the magnet to carry the temperature of

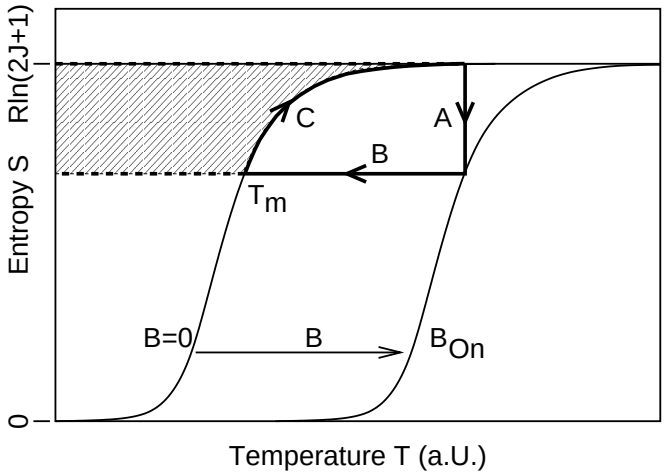

Figure 4.3: Entropy diagram of a paramagnetic salt in an ADR

the salt pill to an accessible and magnetic-field-free experimentation volume. The salt pill is hooked thermally isolated on a plate at the bottom of the liquid helium reservoir (base-plate, 4 K-plate) with Kevlar strings which have a very low heat conductivity. The liquid helium reservoir provides the operation temperature for the superconducting magnet coil mounted inside the reservoir, and on the other hand it works as the heat bath at $T_B = 4.2\,\mathrm{K}$ for cooling the paramagnetic salt pill.

The paramagnetic salt pill consists of a salt of a rare earth which has a half occupied $4f$ shell. If no magnetic field is applied to the salt pill, at temperatures above the self-ordering temperature T_m of the spin system, the spins uniformly occupy the $2J + 1$ states, assuming a total angular momentum J. Then the entropy per mole of the spin system is

$$S_S = R \ln(2J + 1)\,, \tag{4.1}$$

with R being the gas constant.

To start a cool-down cycle, the pill-stick is coupled to the heat bath via a mechanical heat-switch which is mounted on the base-plate and is operated by a motor at room temperature. With the heat-switch closed, a magnetic field is applied to the salt pill to orient the spins along the magnetic field vector.

With the spins being oriented in the magnetic field, one degree of freedom for carrying thermal energy is lost. Due to the conservation of entropy, S_S is pushed into the phonon system of the salt pill and leads to a heating-up of the salt pill and the pill-stick. With the heat-switch closed, the entropy S_S is carried out of the salt pill and into the heat bath, as the pill-stick is cooling to the heat bath temperature. The situation is visualised in the S - T diagram figure 4.3. By increasing the magnetic field B, the entropy of the spin system drops isothermally, following path A.

Due to finite heat conductivity of the heat switch the thermal relaxation takes some time until the salt pill is approximately back at the bath temperature T_B, and the heat-switch may be opened again. The salt pill is now a thermodynamically isolated system carrying a total entropy S_P. If then the magnetic field is reduced adiabatically to zero, the spin system is again capable of carrying the entropy S_S, and the entropy S_P will equally distribute also in the spin system following the equipartition rule. In figure 4.3 the temperature of the salt pill is reduced adiabatically along path B as the entropy per degree of freedom is reduced. The lowest reachable temperature is given by T_m according to the ratio between the heat capacity C_S of the spin system, the total heat capacity C_P of the whole closed system containing salt pill and pill-stick, and the applied magnetic field B_{On}. The salt pill will then slowly warm up along path C by gathering heat from its ambiance by the mechanical mounting, the measurement wires connecting the pill-stick to the environment, electrical heating by the measurement currents, and thermal radiation. The heat power gained by this process from the salt pill is marked as the hatched area in figure 4.3 [Pob96].

The ADR cryostat used with the mass spectrometer is in one point extended compared to the general description given above. To reduce the heat flow via cables and mechanical mountings, it is fitted with two salt pills. A Gadolinium Gallium Garnet (GGG) salt pill with higher $T_{m1} \sim 500\,\mathrm{mK}$ (first stage) is mounted between a Ferric Ammonium Alum (FAA) salt pill with lower $T_{m2} \sim 20\,\mathrm{mK} < T_{m1} < T_B$ (second stage) and the heat bath. The mechanical and electrical connections leading from the heat bath to the second stage pill are anchored at the first stage pill. By reducing the heat-flow to the FAA salt pill the warming-up is slowed down and thus the operating time at a certain temperature setpoint is increased. The base temperature may be lowered as well.

The operation of the cryogenic detector requires a fixed and stable temperature. With the ADR cryostat the temperature of the pill stick can be regulated by applying a small magnetic field to the salt pill. In normal cryostat operation, at the end of the cool-down the magnetic field is first lowered to $B = 0$ and then again slowly increased, until the operating temperature of the detector is reached. The temperature is then stabilised by regulating the magnet current with a PID controller.

4.1.2 Thermal Radiation Introduced into the Cryostat

Usually the cold parts of a cryostat are fully surrounded with a shield at liquid helium temperature, and the introduced heat flow by radiation is negligible compared to heat flow through mechanical mountings and electrical wires. In the mass spectrometer cryostat an opening is necessary to let the ions enter into the cryostat. This opening must be in direct line-of-sight to the detector which operates at a temperature of about 100 mK.

An opening in the cryostat can be treated as a black body radiator if the radi-

ation field outside is uniformly distributed in all directions. Its emitted thermal radiation is given by the Stefan-Boltzmann law eqn. (3.1), and the hole irradiates with the Lambertian cosine characteristic to the half space inside the cryostat. The radiation power scales with the fourth power of the black body's temperature. It is absolutely crucial to keep the introduced heat load at a tolerable level. The size and the distance of the entrance hole for the ions must be chosen with care.

Simply drilling a hole of an area $A = 1\,\mathrm{cm}^2$ in the wall of the cryostat, considering a uniform temperature distribution of $T_h = 4.2\,\mathrm{K}$, 77 K and 300 K, respectively, outside the cryostat, would lead to a total heat power irradiated into the cryostat of

$$P_{em} = \sigma \cdot 1\,\mathrm{cm}^2 \cdot T_h^4 = \begin{cases} 1.8\,\mathrm{nW} & , \quad T_h = 4.2\,\mathrm{K} \\ 200\,\mu\mathrm{W} & , \quad T_h = 77\,\mathrm{K} \\ 46\,\mathrm{mW} & , \quad T_h = 300\,\mathrm{K} \end{cases} . \tag{4.2}$$

This would cause a heat flux at the place of the pill-stick, which is in a distance of about 20 cm to the cryostat wall, of

$$\Phi_{em} = P_{em}/\{4\pi \cdot (20\,\mathrm{cm})^2/2\} = \begin{cases} 1.4\,\mathrm{pW/\,cm}^2 & , \quad T_h = 4.2\,\mathrm{K} \\ 160\,\mathrm{nW/cm}^2 & , \quad T_h = 77\,\mathrm{K} \\ 37\,\mu\mathrm{W/cm}^2 & , \quad T_h = 300\,\mathrm{K} \end{cases} . \tag{4.3}$$

For comparison, the introduced total heat power at 300 K will cause 100 ml of liquid helium to boil out in 93 minutes[1]. The heat flux at 77 K on a detector holder of $3.0 \times 3.0\,\mathrm{cm}^2$ size is already comparable with the heat introduction through mounting and cabling to the pill-stick of the ADR cryostat. On the other hand a mounted detector will be thermally weakly coupled. The thermal coupling of typical detectors will be in the order of $\mathcal{O}(10^1 - 10^2\,\mathrm{nW/K})$ as discussed in sec. 6.1, so this heat flux will still heat the detectors up from base temperature to far above 100 mK.

As shown the size of the entrance hole for the ions must be chosen with care. The 300 K thermal radiation must not enter the cryostat at all. Instead, the whole flight path of the ions that is in the line-of-sight of the cryogenic detector should be at least shielded with a liquid nitrogen cooled radiation shield. Furthermore the opening in the liquid helium cooled shield should be as far away from the detector as possible, as the solid angle of the detector relative to the entrance hole reduces with the square of its distance.

These considerations lead to the design of a snout as shown in figure 4.2. To move the entrance hole in the liquid helium shield away from the cryogenic detector, a copper tube of 14 mm inner diameter and 50 cm length is connected to the liquid helium shield. The distance between the cryogenic detector and the

[1] $\Delta H_{ev} = 20.6\,\mathrm{J/g}$, $\rho = 125\,\mathrm{g/l}$

entrance hole of the tube is then 60 cm. Different apertures may be mounted at both ends of this tube to adjust the hole size and thereby the radiation power entering the cryostat. The aperture at the outer end of the snout acts as a point-like source and its size defines the radiation power being irradiated into the cryostat. The aperture at the inner end of the snout cuts out the solid angle element of this radiation power that will enter the experimentation volume. Ideally, the rest is absorbed by the walls of the snout.

The inner wall of the snout tube was blackened with potassium sulfide (K_2S, "Schwefelleber") to increase the infrared absorption and thus minimise reflections. As small-angle reflection is quite high for all materials, additional baffles must be installed inside the tube to prevent radiation coming directly from the input aperture to be reflected at the inner tube wall.

Additionally the liquid helium cooled tube is placed inside a liquid nitrogen cooled tube. This is to reduce the heat load to the liquid helium cooled tube to get it as cold as possible, especially at the outer end. Since the coupling to the helium bath can only be provided at the inner end of the 50 cm long tube, heating of the outer end due to heat radiation onto the tube must be minimised. Additionally, at the end of the liquid nitrogen cooled tube a connector with baffles is mounted which fits into a liquid nitrogen cooled socket inside the mass spectrometer. By this connection the cryostat's snout can be moved into the mass spectrometer's socket so that no 300 K thermal radiation can enter the line-of-sight of the cryogenic detector at all.

The outermost ends of the liquid nitrogen tubes, the one of the snout and the one inside the mass spectrometer, have been measured to achieve a temperature of 100 K. With this black body temperature and a usual set of apertures of $\varnothing$ 10 mm diameter each, the heat power transmitted into the cryostat is

$$P_h = 45\,\mathrm{nW} \tag{4.4}$$

at the snout outlet, and the heat flux at the detector position is

$$\Phi_h = 40\,\mathrm{nW/cm^2}\,, \tag{4.5}$$

a value that is acceptable during the detector operation.

Not for every type of cryogenic detector that much effort needs to be taken to reduce the thermal radiation load on the detector surface. For example tunnel junction detectors are usually operated at higher temperatures around $0.3 - 4\,\mathrm{K}$ and have a much smaller surface area of only $\sim 100\,\mu\mathrm{m} \times 100\,\mu\mathrm{m}$. Other groups like [Ger00, Hil98] use setups which expose the cryogenic detector directly to the MALDI source at room temperature.

4.2 Detector Setup

The cryogenic detector is mounted at the end of the pill-stick, on two support holders made of annealed copper. They carry as well the shunt resistors of the

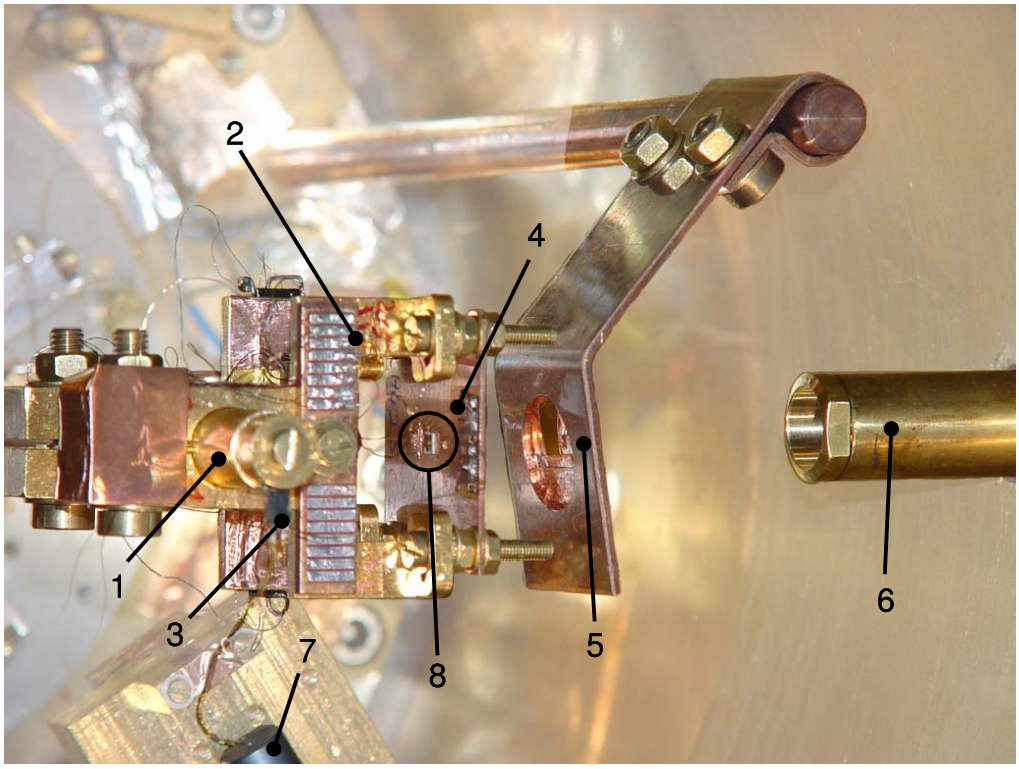

Figure 4.4: Mounting of a cryogenic detector in the cryostat. (1) pill-stick, (2) top support holder with soldering terminal, (3) carbon thermometer (below top support holder), (4) holder of the cryogenic detector, (5) 4 K aperture, (6) entrance snout, (7) SQUID sensor, (8) detector.

readout circuits (see sec. 4.5.2), a carbon thermometer for measuring the temperature of the cryogenic detector, and a soldering terminal for the electrical wiring.

Besides the detector in the alignment with the mass spectrometer a second one can be mounted on the bottom support holder, which allows measurements with two detectors in the same cryostat run. For example one detector can be run as the cryogenic detector with the mass spectrometer and the other one may be characterised with a ^{55}Fe source or its transition might be measured in absence of thermal radiation load.

Figure 4.4 shows a picture of a mounted cryogenic detector. Two additional apertures may me mounted to reduce the thermal radiation on the cryogenic detector if necessary. A "cold aperture" mounted directly in front of the detector (not visible in the figure) can be aligned most precisely. The purpose of the other aperture is mainly to reduce the thermal radiation load on the pill-stick. It is mounted with a copper stick to the 4 K plate.

The design of the detector holder varies for the different cryogenic detectors, depending on their shape. In figure 4.4 the holder is simply a copper plate with

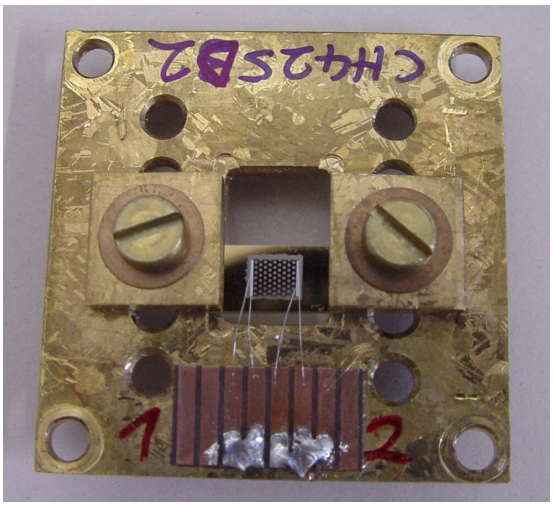

Figure 4.5: Another detector holder with a mounted detector.

a hole of ∅ 3.2 mm diameter. The detector is glued to it with two drops of GE-Varnish at opposite corners. Another holder with a mounted detector is shown in figure 4.5. The holder is a copper plate with a machined square hole (behind the detector crystal) and a machined groove in which the detector settles. The detector is fixed by square copper discs screwed to the holder with beryllium-copper spring washers which adjust the clamping force. All holders have glued copper-capton contact strips, to which the electrical contacts from the detector are bonded.

4.3 Mass Spectrometer

The mass spectrometer was built according to our specifications by Stefan Kaesdorf Geräte für Industrie und Forschung, based in Munich. By its functional principle it is a MALDI Reflectron-TOF as explained in sec. 3.2. It is equipped with a liquid nitrogen cooled ion reflector.

Figure 4.6 shows the mass spectrometer, without the cryostat mounted at the end. If a channel plate detector is mounted at the ion outlet, it may be run like any conventional MALDI TOF-MS.

The spectrometer is split in two vacuum chambers connected with a small gate valve. The MALDI source is placed in the small vacuum chamber (source chamber) on the right side of figure 4.6, all other components are mounted inside the main vacuum chamber in the middle of the drawing. This allows to vent the source chamber and replace the measurement samples in less than one hour, as the source chamber may be pumped to its operational pressure of $< 3 \cdot 10^{-7}$ mbar in about 30 minutes.

The measurement samples are placed on top of a stick which is inserted along

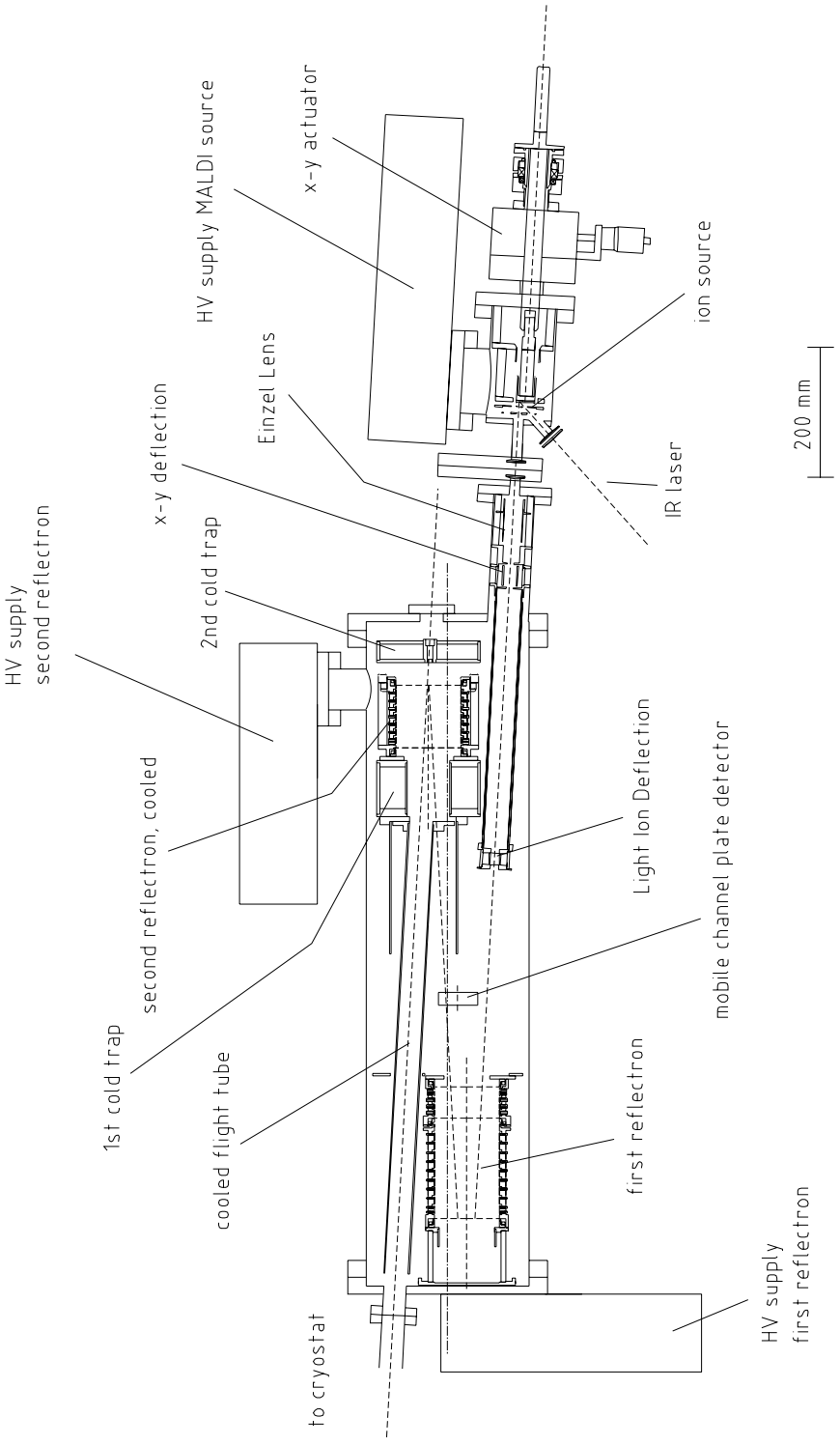

Figure 4.6: Sketch of the mass spectrometer. See the text for description.

the ion beam axis from the backside of the MALDI source. The stick can be rotated revolver-like and can carry up to six different measurement samples on a stainless steel disc with six grooves (figure 4.7). A certain position to shoot on with the laser on one of the measurement samples may be selected with an x-y actuator pair, under the optical control of a video monitoring system. The stainless steel disc is screwed to the stick, which allows a quick change of the disc and to prepare a new sample on the disc while another one is measured in the mass spectrometer.

A shot from the pulsed UV laser of 337 nm wavelength desorbs and ionises the molecules. The shot duration is some ns. The laser is attenuated with a dielectric attenuator and focused on the sample disc with a lens with focal length $f = 200\,\mathrm{mm}$ outside the vacuum. At the sample disc the laser power density usually is in the order of $10^6 - 10^7\,\mathrm{W/cm^2}$. The laser shot also triggers the time-of-flight measurement. The maximum acceleration voltage of the MALDI source is 18 kV. Its delayed extraction can be tuned in onset time, and in voltage step height between $\sim 0 \ldots 90\%$ of the acceleration voltage. The ion beam is focused with an Einzel Lens and deflected in the electric field of x-y deflection plates.

The mass spectrometer is also instrumented with a light-ion-deflection. It consists of a pair of deflection plates which are applied with an electric field from the moment when the laser has fired. They deflect any ions out of the beam path until the electric field is switched off. As the light ions are the fastest ones they are the first ones to arrive at the light-ion-deflector and are deflected. After the light ions have passed the deflector and the heavier ions of interest arrive, the deflection field is switched off and these ions can freely pass the deflector. The deflection of light ions is used to prevent the detector, MCP as well as cryogenic detector, from saturating. It is of special interest when working with the cryogenic detector. At almost every measurement shot, a large number of light matrix ions is emitted from the source. They could heat up the detector above its operational temperature and make it insensitive for a few $100\,\mu$s. To avoid that, these light matrix ions must be prevented from hitting the detector by the light-ion-deflector.

The time-of-flight path is a reflectron with two ion mirrors. The first ion mirror has a middle and an end grid and is used to tune the mass focus onto the detector plane. The second ion mirror has one grid and a short electric field length. Its purpose it to deflect the ion beam with only little disturbance of the ion focus. Between the two reflectors an additional detector may be moved into the beam path. It is useful for alignment purposes and to check for an ion signal when it cannot be found with the main detector.

The second ion mirror is cooled with liquid nitrogen in a way that all surfaces which are in the line-of-sight of the cryogenic detector are cooled to a temperature between 77 K and 100 K. In addition a tube is mounted at the head of the reflector which reaches to the end of the main vacuum chamber. This flight tube is liquid nitrogen cooled as well. So any part in line-of-sight with the detector is covered

No.	V_{acc} [keV]	V_{DE} [keV]	t_{DE} [ns]	V_L [keV]	V_x [V]	V_y [V]	V_{1E} [keV]	V_{1M} [keV]	V_2 [keV]	Ion
1	18.0	13.0	0	9.6	170	0	23.0	17.0	20.0	
2	18.0	14.0	400	9.6	180	0	23.0	17.2	20.0	INS
3	18.0	14.0	600	9.6	180	0	23.0	16.2	20.0	
4	18.0	14.0	800	9.6	180	0	23.0	16.2	20.0	BSA
5	13.5	10.0	0.0	7.2	120	0	17.5	12.0	15.0	
6	9.0	6.0	0.0	4.7	90	0	11.5	8.0	10.0	

Table 4.1: Typically used settings of the mass spectrometer ion optics: V_{acc} Acceleration voltage, V_{DE}, t_{DE} Delayed Extraction voltage and delay time, V_L Ion Lens voltage, V_x, V_y Beam Deflection voltages, V_{1E}, V_{1M} reflector #1 end- and mid grid voltages, V_2 reflector #2 grid voltage.

with a liquid nitrogen cooled shielding.

Practical considerations suggested the design with two reflectors. With only one reflector, the cryostat would need to be mounted close to the ion source. Since the cryostat as well as the ion source with its high voltage power supplies consume a lot of space, this would be almost impossible.

At the beam outlet of the main vacuum chamber a gate valve with a clearance of 50 mm is mounted. There, either a conventional channel plate detector or the ADR cryostat with its cooled snout may be mounted. The liquid nitrogen cooled part of the cryostat's snout can then be pushed through the gate valve into a socket at the end of the liquid nitrogen cooled tube inside the mass spectrometer. The channel plate detector is mounted in a 60 cm long tube to locate it at the same position in the beam path as the cryogenic detector.

For operating the mass spectrometer, a proper set of parameters must be found to focus the ion beam on the detector. With the focus point shifting slightly with the mass of the ions, different settings are appropriate for different mass ranges. A summary of useful settings for the mass spectrometer ion optics is given in Table 4.1. The column "Ion" marks parameter sets which were notedly useful for the measurement of specific ions (insulin or BSA).

4.4 Sample Preparation

For MALDI mass spectrometers, the preparation of a suitable matrix / analyte compound is a crucial step in the whole MS process. It is the key to get the analyte molecules ionised and accelerated in the right manner in the MALDI process.

The difficulty is to find a suitable solvent and matrix which are compatible

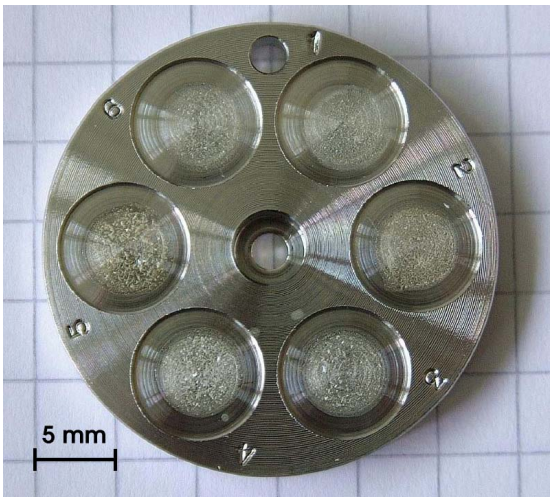

Figure 4.7: A sample disc of the mass spectrometer with six dried droplets prepared.

with the MALDI process as well as with the analyte. In the process of the cryogenic detector development, well-known proteins were used to measure the parameters of the detector, amongst others Insulin (5.734 kDa), Cytochrome C (12.361 kDa), Bovine Serum Albumin BSA (66.431 kDa) and Immuno-globulin G IgG (150 kDa). They all worked well in the MALDI process with the matrices sinapic acid and 2,5-DHB.

For sample preparation the dried-droplet method was used, as described in the following paragraph [Glo00].

Before preparing the MALDI target, the analyte protein and the matrix each need to be dissolved in a solvent consisting of:

60%	Acetonitrile
0.1%	Tri-fluor acetic acid (TFA)
39.9%	deionised H_2O ($> 1\,M\Omega$)

The matrix is prepared in a saturated solution, with matrix molecules falling out at bottom. The concentration of the dissolved analyte proteins (stock solution) usually is $1\,\mu g/\mu l$. Matrix solution and stock solution are then mixed with a ratio of $2:1$ to $1:1$, and $1-2\,\mu l$ of the mixture is put on a sample disc of the mass spectrometer. The droplet needs to dry for about 30 min. Picture 4.7 shows a sample disc with six different sample droplets.

Another important fact when handling the sample discs is the cleaning before reuse. First, old droplets are removed with solvent in the ultrasonic for 15 min, then the sample disc is cleaned with a mixture of 50% ethanol, 50% deionised water in the ultrasonic for 15 min. At the end the sample disc is flushed with acetone and dried.

4.5 Measurement Electronics

The developed cryogenic detectors are very low-ohmic devices. A special measurement setup is needed to convert the resistance change of the superconducting phase transition thermometers (SPT) into a voltage signal which can be fed in a conventional digitiser to be processed in a computer. The measurement setup is shown in figure 4.8. It will be described in the following sections, starting with the elements inside the cryostat.

4.5.1 Cold Parts

Superconducting phase transition thermometers have a resistance in the order of $10 - 200\,\mathrm{m\Omega}$ at their operating point. This impedance is too low to be sensitively measured with a FET or similar transistor circuit. Instead, the appropriate device to read out such low-impedance signal sources is a Superconducting Quantum Interference Device, SQUID. It measures a current by sensing the magnetic field produced by the current in the SQUID input coil. The function of the SQUID will be described in detail in sec. 4.6.

The centre of the measurement setup is the readout circuit, shown in figure 4.9. It consists of the SPT film, a shunt resistor and the SQUID input coil. These parts are placed in the cryostat, as close to each other as possible, to reduce parasitic inductance and capacitance of the wiring connecting them. The shunt resistor is mounted on the pill-stick, because its thermal noise (Johnson noise) shall be as low as possible. The SQUID sensor and its input coil are mounted close to the pill-stick on a support from the 4 K plate. It must not be mounted at the pill-stick for several reasons: The heat dissipation of the bias current in the SQUID sensor is unacceptably high. Additionally the SQUID sensor is very sensitive to temperature changes. It needs the well-defined temperature of the liquid-helium bath for stable operation. Finally, several wires connect the SQUID sensor with its feedback electronics which are located outside the cryostat. These cables would introduce heat load to the pill-stick as well if the SQUID is mounted there.

4.5.2 Readout Circuit

The readout circuit is sketched in detail in figure 4.9. A constant measurement current is injected into the readout circuit with a differential current source located outside the cryostat. Typical measurement currents are in the order of $I_{tot} = 5 - 100\,\mu\mathrm{A}$. The current splits up in the two branches of the readout circuit, according to the resistance proportion of the shunt resistor R_S and the SPT film resistance R_F. Usually $R_S = 20\,\mathrm{m\Omega}$, and $R_F = 10 - 100\,\mathrm{m\Omega}$ at its operating point. If the resistance of the SPT film changes, for example because an ion hits the calorimeter and heats it up, the branching of the current changes.

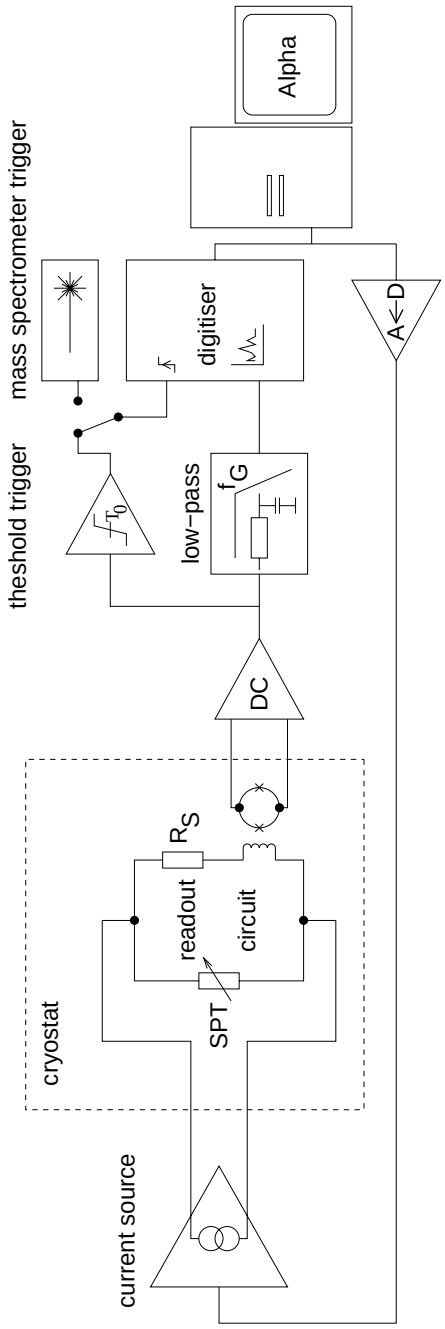

Figure 4.8: Measurement electronics diagram. A constant current is injected into the readout circuit. A resistance change of the SPT leads to a current change in the SQUID sensor which is amplified and fed into a digitiser. The feedback of the SQUID is not shown for simplicity.

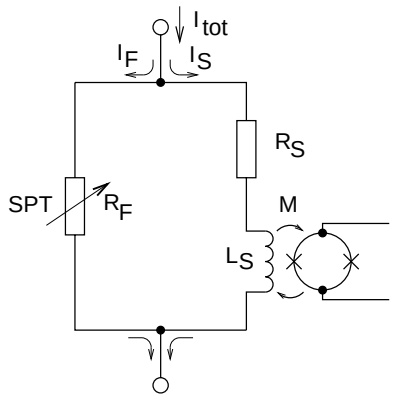

Figure 4.9: Readout circuit for measuring resistance changes of the SPT film.

I_{tot} is constant at any time. Thus the dynamic properties of the current source and the capacitance and inductance of the long wires feeding I_{tot} from outside the cryostat to the readout circuit do not affect the dynamic behaviour of the readout circuit at all.

Although the inserted measurement current I_{tot} is constant, the SPT film may be driven either in a "constant current" or a "constant voltage" regime. If the shunt resistor is larger than the SPT film resistor, $R_S \gg R_F$, then the majority of I_{tot} passes through the SPT film. The voltage drop in the readout circuit is defined approximately by R_F,

$$\Delta U = U_F = R_F \cdot I_F \approx R_F \cdot I_{tot}\,, \tag{4.6}$$

the larger the ratio between R_S and R_F the better the approximation. If R_F changes due to an ion impact, ΔU will change but the current through the SPT film $I_F \approx I_{tot}$ will stay constant. This is the "constant current" regime. In this regime, the dissipated electrical power $P_{el} = I_F^2 R_F \approx I_{tot}^2 R_F$ in the SPT increases when the temperature of the SPT film rises. This effect is called positive electrothermal feedback.

In the opposite case, if $R_S \ll R_F$, the majority of I_{tot} flows through R_S, and the voltage drop in the readout circuit is mainly given by the constant R_S,

$$\Delta U = U_S = R_S \cdot I_S \approx R_S \cdot I_{tot} = const\,. \tag{4.7}$$

Then, if R_F changes, its voltage drop will not change but its current which is a small fraction of I_{tot} will change with its resistance change, $I_F = U_F/R_F \approx U_S/R_F$. This is the "constant voltage" regime. If in this regime R_F is increased due to ion impact, the dissipated electrical power $P_{el} = U_F^2/R_F$ is decreased and thereby counteracts the deposited energy of the ion impact. This effect is called negative electro-thermal feedback [Cab96, Irw98].

In practice, neither of the extremes is fulfilled. Nevertheless it is taken care that R_S usually is smaller than R_F. Operating on the "constant voltage" side is preferred due to its self-stabilising capability.

4.5.3 Signal Processing

For actually measuring the resistance of the SPT film, the current in the shunt branch of the readout circuit is measured via a SQUID sensor. The SQUID sensor is operated with an appropriate flux locked feedback electronics which provides a voltage proportional to the current through the SQUID input coil. This voltage is fed through an anti-aliasing low-pass filter and recorded with a 25MHz digitiser module. The data can then be saved and analysed in a VMS Alpha workstation with custom made software.

The measurement current I_{tot} can be controlled by a computer via a D-A converter through a control input of the current source. This feature is mainly used when recording transition curves of SPT films.

Data recording is done in two different modes. One mode is used if events are recorded which happen randomly, for example the measurement of radioactive test pulses like the 5.9 keV ^{55}Fe X-ray pulses. In this mode the recording of events is triggered once the SQUID output voltage exceeds a certain trigger threshold. Then a time window is recorded which includes the whole event. In the other mode the recording is directly triggered by the laser shot of the mass spectrometer. In this mode the time window usually is larger, as the whole event is recorded from the moment of the laser shot until the last ions for sure have arrived at the detector.

4.5.4 Measurement Software

Both programs used for recording, for random events and for MS shots, include online analysis tools to check the quality of the recorded data. To each recorded event a smoothing by moving-average is applied. After smoothing, for random events the pulse height of the event is analysed by a maximum search and is plotted in an online pulse-height histogram. For MS shots, after smoothing ion impact times are determined in the recorded shot as the first derivative of the signal curve exceeds a certain trigger level. With this a coarse online mass spectrum is produced.

The final measurement analysis is done off-line. For the random pulses, usually in a first step bad records are sorted out. These are records with a SQUID flux loss, which produce a voltage step with the height of a multiple of the flux quantum, resets of the SQUID electronics, pile-ups of several events, or other disturbed records. In a second step, a theoretical model of the pulse shape as described in sec. 2.2.1 is fitted to each record. With these data the analysis can be performed.

For the analysis of the MS data multiple routines were developed which are described in sec. 4.7.

4.6 High-Speed SQUID Readout

In contrast to other experiments done with SPT calorimeters, the bandwidth of the measurement system plays an important role when doing the time-resolved measurements in a TOF-MS [Uch01]. Although the relevant time resolution in the order of 0.1 μs does not constitute a serious problem for the conventional electronics outside the cryostat, difficulties arise in the cold parts of the measurement circuit and in the SQUID amplifier electronics. SQUID amplifiers are limited in their bandwidth by several factors which will be discussed in the following sections. Amplifiers which can resolve 0.1 μs short signals rank among high-speed SQUID amplifiers. For our setup, the bandwidth of the cold readout circuit needs to be considered as well.

4.6.1 Different SQUID Amplifier Setups

Usually the terminal voltage of a SQUID sensor is not measured directly because of its non-linear and periodic transfer function. Instead, it is operated with an amplifier- and feedback circuit which keeps the SQUID sensor in a stable operating point and linearises its output voltage. The SQUID amplifiers are classified as modulated and unmodulated amplifiers according to the functionality of the feedback loop.

Modulated and unmodulated SQUID amplifier are sketched in figure 4.10. The SQUID sensor is supplied with an adjustable DC bias current as symbolised by the Resistor I_{Bias} in both cases. If, like in many applications, the SQUID is used not as a magnetic flux sensor but as a current sensor, an electric coil is wound around the SQUID sensor such that it magnetically couples to the SQUID sensor. This input coil is then supplied with the current to measure. A feedback coil is wound around the SQUID sensor as well. Once the feedback loop is closed, this feedback coil is driven in a way such that it always produces a magnetic flux which zeroes out the magnetic flux produced by the input coil. Thereby the SQUID sensor is stabilised at a certain operating point. In turn, the output signal of the SQUID amplifier is in fact the voltage driving the feedback coil.

It must be mentioned here that the bandwidth of SQUID amplifiers is not limited by the SQUID sensor itself whose bandwidth is limited by the inductance of the superconducting ring. It is limited by the time constant of the amplifier loop.

Modulated and unmodulated SQUID amplifiers differ in the way the feedback loop is closed. In the modulated SQUID amplifier (figure 4.10a), the terminals of the SQUID sensor are connected to a preamplifier via a transformer. Thus the feedback loop is DC decoupled and needs to be closed with the help of a modulation frequency f_{mod}. The modulation frequency continuously drives the feedback coil of the modulated SQUID amplifier with an amplitude corresponding to a flux modulation of about $\Phi_0/2$ in the SQUID sensor. This leads to a modulation of

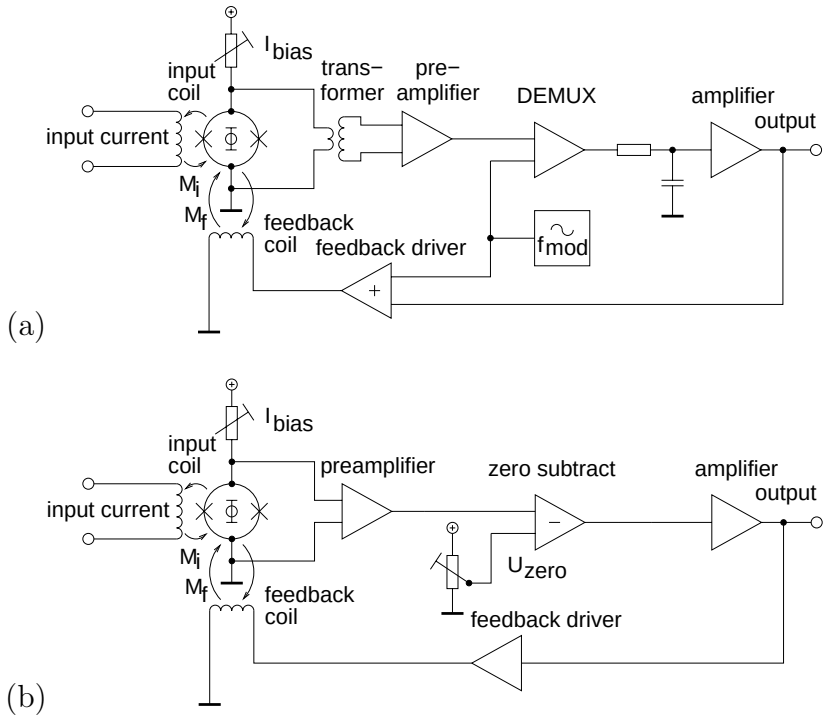

Figure 4.10: Functional diagram of the modulated (a) and unmodulated (b) SQUID amplifier.

the magnetic field in the SQUID sensor and thus to a modulation of its terminal voltage. The transformer is used to lift the signal strength by a factor of $5 \ldots 10$ before the preamplifier. It also matches the low impedance of the SQUID sensor to the higher impedance of the preamplifier.

Past the preamplifier, the SQUID signal is fed in a multiplexer (demodulator) together with the modulation frequency f_{mod}. This selectively suppresses frequency components which are not in phase with the modulation frequency. Then the modulation frequency is removed with a low-pass symbolised by the R-C element and the signal is amplified to its final amplitude. The loop is closed by adding this signal back to the modulated driver of the feedback coil. The amplified signal as well represents the output voltage of the modulated SQUID amplifier.

In the unmodulated SQUID amplifier (figure 4.10b) no transformer is involved. The terminals of the SQUID sensor are directly connected to the preamplifier. By this a constant and unwanted DC voltage offset is amplified as well. It needs to be subtracted; otherwise it would be fed back to the feedback coil and self-amplified. After being amplified, the signal closes the DC-coupled loop to the feedback driver and works as the output voltage of the unmodulated SQUID amplifier.

Modulated SQUID amplifiers may achieve a better noise level than unmod-

ulated SQUID amplifiers. Since they settle on a modulation frequency their working frequency is shifted away from the $1/f$ noise of the preamplifier which dominates around zero frequencies. Additionally the signal-to-noise ratio of the SQUID sensor is improved due to the amplification of the cold transformer.

On the other hand the transformer is the element which actually limits the loop delay and the bandwidth of modulated SQUID amplifiers. The modulation frequency cannot be higher than the cut-off frequency of the transformer. For example the SQUID amplifiers installed in the High-Speed Test Cryostat #2 have a modulation frequency $f_{mod} = 320\,\mathrm{kHz}$. The bandwidth must be limited by a low-pass filter to a maximum of half the modulation frequency. The cut-off frequency and the order of the low-pass specify the leakage of the modulation frequency to the output signal of the SQUID amplifier.

Unmodulated SQUID amplifiers in contrast have a worse noise level. They are less stable to operate due to the DC offset subtraction. It needs to be done very carefully and is quite sensitive to temperature drifts of the DC voltage offset of the amplifier circuits in the feedback loop. Their bandwidth is much higher than that of modulated SQUID amplifiers, though, since they are not limited by the transformer. In addition the full bandwidth of the feedback loop is accessible to the signal bandwidth since no frequency gap needs to be regarded between the signal cut-off frequency and a modulation frequency.

One of the test cryostats being used for preliminary detector tests (called cryostat #2) was initially provided with a four-channel modulated SQUID amplifier. Many of the preliminary detector tests, like most of the 5.9 keV ^{55}Fe X-ray experiments were made in test cryostats instead of in the ADR cryostat used in the MS setup. The modulated SQUID amplifiers had a modulation frequency $f_{mod} = 320\,\mathrm{kHz}$ and a bandwidth of 25 kHz. Later on, one of the amplifier channels was modified to have a bandwidth of 150 kHz and thus be able to theoretically detect at least small-signals with a rise time of $(150\,\mathrm{kHz})^{-1}/2\pi = 1.1\,\mu\mathrm{s}$. The drawback of this setup was the leaking of the modulation frequency to the SQUID output signal since the filter steepness was not high enough.

In addition an unmodulated SQUID amplifier was installed in the same test cryostat, with a bandwidth of $\sim 1\,\mathrm{MHz}$. It was quite sensitive to flux losses, though, so it could process small signal amplitudes only.

One further development of the unmodulated SQUID amplifier is the double-stage SQUID amplifier. In this setup, instead of connecting the terminals of a first stage SQUID sensor directly to an operational amplifier, it is connected via a resistor to the input coil of a second stage SQUID sensor. The feedback loop is closed through the first stage SQUID, and the second stage SQUID works as another preamplifier before the operational amplifier [Uch98].

The advantage of the double-stage SQUID setup is an improved noise level. It is $0.3\,\mathrm{nV}/\sqrt{\mathrm{Hz}}$ for the best room temperature operational amplifiers. This is particularly important for the preamplifier stage. The one used in the MS cryostat has a noise level of $0.7\,\mathrm{nV}/\sqrt{\mathrm{Hz}}$. It is larger than the SQUID sensor's

output noise level of $\sim 0.2\,\mathrm{nV}/\sqrt{\mathrm{Hz}}$ and dominates the total noise.

If the first stage SQUID signal is amplified by a second stage SQUID with an amplification factor between 5 and 10, the signal-to-noise ratio of the operational amplifier stage is improved correspondingly and its contribution to the total noise is less than that of the SQUID sensor itself. Double-stage SQUIDs can achieve a $\delta V/\delta\Phi$ of a few mV/Φ_0 instead of $10-100\,\mu\mathrm{V}/\Phi_0$ of single-stage SQUIDs [Mas95]. A double-stage SQUID setup has been mounted in another test cryostat (Leiden test cryostat #3).

For the mass spectrometer cryostat it was decided to mount two single-stage unmodulated SQUID amplifiers. The SQUID sensors are made by JeSEF Jena Superconductive Electronics Foundry located in Jena, Germany, whereas the dual amplifier was built by Cryoton Ltd. located in Troitsk, Russia. The SQUID noise level was specified as $4.4\,\mathrm{pA}/\sqrt{\mathrm{Hz}}$ and measured to be between $5-8\,\mathrm{pA}/\sqrt{\mathrm{Hz}}$, which is in fair agreement, if the non-ideal measurement conditions in the laboratory are taken into account. Some other technical data of the SQUID amplifiers are shown in Table 4.2.

As a further improvement of the SQUID system in the mass spectrometer cryostat, the application of a cold preamplifier is in development [Uch02]. Thereby the preamplifier stage of the amplifier electronic is mounted inside the cryostat on one of the cold shields. This reduces the noise of the preamplifier and improves the loop gain of the feedback loop. Bandwidth and signal-to-noise level are increased.

parameter	value
amplifier type	unmodulated
SQUID noise level	$4.4\,\mathrm{nA}/\sqrt{\mathrm{Hz}}$
SQUID input coil inductance	320 nH
mutual inductance input coil – SQUID	10 nH
SQUID $\mathrm{d}I/\mathrm{d}\Phi$	$204\,\mathrm{nA}/\Phi_0$
amplifier $\mathrm{d}V/\mathrm{d}\Phi$	$1.27\,\mathrm{V}/\Phi_0$
amplifier bandwidth	1 MHz

Table 4.2: Some technical data of the SQUID amplifiers used in the mass spectrometer cryostat setup

4.6.2 High-Speed Behaviour

The maximum reachable bandwidth of the readout electronics is limited by several components. First to mention are the parts of the measurement electronics outside the cryostat. They are state-of-the-art devices, connected with standard

50 Ω BNC or Lemo wires, and consequently give no limitation here. The upper limit of time resolution is given by the digitiser module which has a shortest time-base of 40 ns.

Readout Loop

A not negligible factor is the L/R time constant of the readout circuit. For being current sensitive, a certain magnetic flux $\Phi = L_S \cdot I$ must be applied to the SQUID sensor via its input coil. The more current sensitivity is desired, the higher inductance L_S of the input coil is necessary. The inductance of the SQUID input coil in the MS cryostat is $L_S = 320\,\mathrm{nH}$. The inductance L_W of the wiring of approximately $0.6\,\mu\mathrm{H/m}$ adds to it. For this reason the wires need to be as short as possible. A length of 40 cm seems to be the minimum feasible length, since the SQUID input coil is mounted at the 4 K plate. The wires need to be thermally well anchored and have a minimum length for not acting as a heat bridge.

On the other hand there is the film and the shunt resistance. The shunt resistance shall be as low as possible for working in negative electrothermal feedback mode. A shunt resistor of $R_S = 20\,\mathrm{m\Omega}$ was chosen. The film resistance of one of the cryogenic calorimeters (*CH425C1*, sec. 5.2) was measured with the method described in appendix A to be $R_{op} = 110\,\mathrm{m\Omega}$ at its operating point. Additionally, the resistance of a superconductor in its transition strongly depends on the current flowing through it. Changing the current through the SPT film due to a temperature change leads to an additional, dynamic resistance term of the SPT film [Fra94],

$$R_{dyn} = I \cdot \frac{\delta R}{\delta I}\,. \tag{4.8}$$

Altogether the time constant of the readout loop is

$$\tau_{loop} = \frac{L_S + L_W}{R_S + R_{op} + R_{dyn}}\,. \tag{4.9}$$

Due to the steepness of $\delta R/\delta I$ at the transition temperature, R_{dyn} can be a multiple of the normal-conducting resistance. R_{dyn} can be barely estimated. Thus it is difficult to calculate the true time constant of the readout loop.

SQUID Feedback

As already mentioned in sec. 4.6.1, the constraint in bandwidth of the SQUID amplifier results from the feedback loop. The SQUID sensor itself has a bandwidth far above 1 GHz, limited by the inductance of the superconducting ring.

The restriction in the bandwidth of a SQUID amplifier lies in the finite delay time in its feedback loop. Above a certain threshold in gain, the bandwidth of operational amplifiers decreases linearly with increasing gain. The preamplifier circuit which has the highest gain of about 100 takes a huge part of the SQUID

amplifier's phase shift. At usual lengths of the wiring connecting the cooled SQUID sensor with the room-temperature amplifier electronics, the signal delay in the wiring contributes to the delay time of the feedback loop as well. In the MS cryostat, the cabling length between the SQUID sensor and the amplifier is $2.0 \ldots 2.5\,\mathrm{m}$.

It is also important do distinguish whether an amplifier is limited by the bandwidth or by the slew rate[2]. If it is limited by the bandwidth, when increasing the amplitude of the input signal the bandwidth does not change, instead the slew rate of the output signal rises. If in the opposite case the slew rate is limited, with increasing the input signal the bandwidth decreases.

Passive elements such as L-R or R-C elements are bandwidth limited, as they obey an exponential law which relates the magnitude of the output signal directly with the magnitude of the input signal. Many active components, such as operational amplifiers, are slew rate limited, as they are characterised by their ability to follow an input signal with a limited output signal rate independent of the magnitude of the input signal.

So with an amplifier which is known to be limited to a certain bandwidth it is still possible to measure small signals with a steepness higher than allowed by the bandwidth limit, as long as a limiting slew rate is not exceeded.

4.7 Mass Spectrometry Data Analysis

Signals of conventional channel plate detectors are quite easy to analyse. With an impinging particle, a certain charge appears at their output. The duration and pulse height in volts is defined by the capacitances inside the channel plate. Its duration is in the order of tens of nanoseconds and thus in the time scales of TOF-MS approximated by a Dirac Delta function. To achieve a mass spectrum in an experimental run, it is sufficient to sum up all the digitiser traces recorded during repeated laser shots.

Signal processing with the signals of the cryogenic detectors is not as easy. An impact event at a cryogenic calorimeter results in a film resistance rise with a duration in the order of $\sim 5\,\mu\mathrm{s}$, and a relaxation to the equilibrium film resistance with an exponential time constant of typically $100 - 200\,\mu\mathrm{s}$. With this, two problems arise in mass spectrum generation: determining the onset time, i.e. the ion impact time from the signal rise, and handling pile-ups when ions impact the detector whilst it is still relaxing from an earlier event. A recorded event in figure 4.11 illustrates the situation.

During the cryogenic detector development simultaneously efforts were undertaken to develop a suitable technique for analysing the mass spectrometer shots. It was done by off-line manipulation of the recorded data, as this is the most flexible way to apply different techniques.

[2]slew rate=maximum signal rate of change an amplifier can follow

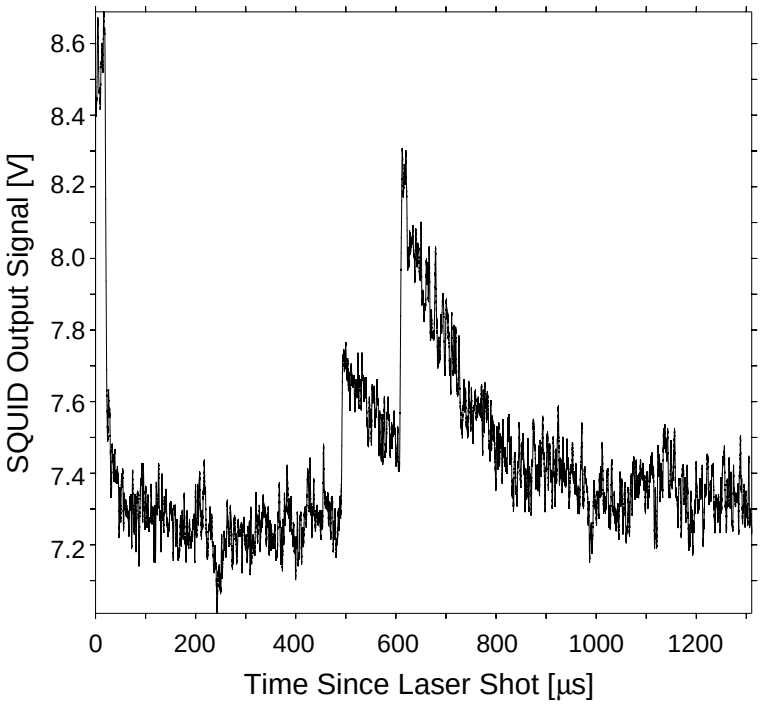

Figure 4.11: A typical cryogenic calorimeter signal as recorded in a MS shot with detector (CH425C1). The protein was BSA.

Derivation Method

The simplest method to find events in a shot record and determine their onset times is to form the derivative of the record. Spikes are expected to occur in the derivative at the points in time (recorded channels) when a signal rise takes place in the data. This was also tried with applying a moving average smoothing to the shot record before taking the derivative, at which for each channel a mean value out of the neighbouring n channels is built.

The derivation method is very sensitive to noise in the input signal which is derived as well. The signal-to-noise ratio tends to become worse. Because of its simplicity the method is useful for quick coarse online data evaluation but not reliable enough for exact analysis.

Deconvolution Method

The deconvolution method scans the shot record for a unified model pulse. This is done by deconvoluting the shot record with the model pulse which is shifted through the digitised sample. If the model pulse is conveniently adjusted on the time axis such that its onset time is at the onset time $t = 0$ of an impact event, then the deconvolution shows a maximum at this point [Urb89].

Such model pulses may be derived from theoretical models, or be summed

from events actually measured with the used calorimeter. Such a standard event is summed out of a class of measured events which are assumed to be close to the expected pulse shape, with as few disturbances as possible. Once a standard event is summed, it may be compared with every event of its creation class and thus be used to refine the creation class successively.

The deconvolution method did not show up the expected quality in impact event detection. The number of missed events was too high to be useful for sensitive MS data processing. Reason for this is the too broad variation in pulse shapes around the mean shape. Many events were not detected due to the fact that the convolution product's peak amplitude at an impact onset did not exceed the noise level.

Gauss-Filter Method

The shot records are filtered by a Gaussian bandpass filter function. High-pass and low-pass cutoff frequencies are tuned in a way that the filter is most sensitive to the frequencies appearing at an impact event's signal onset and rise, and suppresses best all other frequencies. Then the Gauss filtered shot records show one wave train at every impact event in the record.

A pulse is identified in the shot record when the filtered signal exceeds a certain trigger level. This level is calculated for each shot record as a multiple n of the root-mean-square noise V_{rms} of the filtered signal, where the tunable parameter n usually is in the order of $n \approx 3 - 5$. For each identified event, moving average minimum and maximum of the shot record are determined in a certain window around the event. The onset time is defined as the point when the signal reaches 10% of its maximum in this window.

The Gauss-filter method happens to be the most successful method of impact event onset time determination up to now. By using a bandpass instead of a model pulse's fixed rise time it is more tolerant to the fluctuations in pulse shape than the deconvolution method. It is the method currently in use for generating mass spectra. A sample shot record is shown in figure 4.12. The grey curve shows the recorded shot, the black curve is the Gauss-filtered shot. The vertical bars mark the times where the impact event onset has been determined. The method of determining the onset time by searching for the 10% value of the peak amplitude seems not to be the most precise one. It was as well tried to fit a theoretical pulse shape to the shot record, using the determined 10% onset value as a starting value for the fit. The fits worked out well but did not improve the time resolution. It is likely that the time resolution is at present limited by the low signal-to-noise ratio, which means that the noise in amplitude leads to a noise on the time axis.

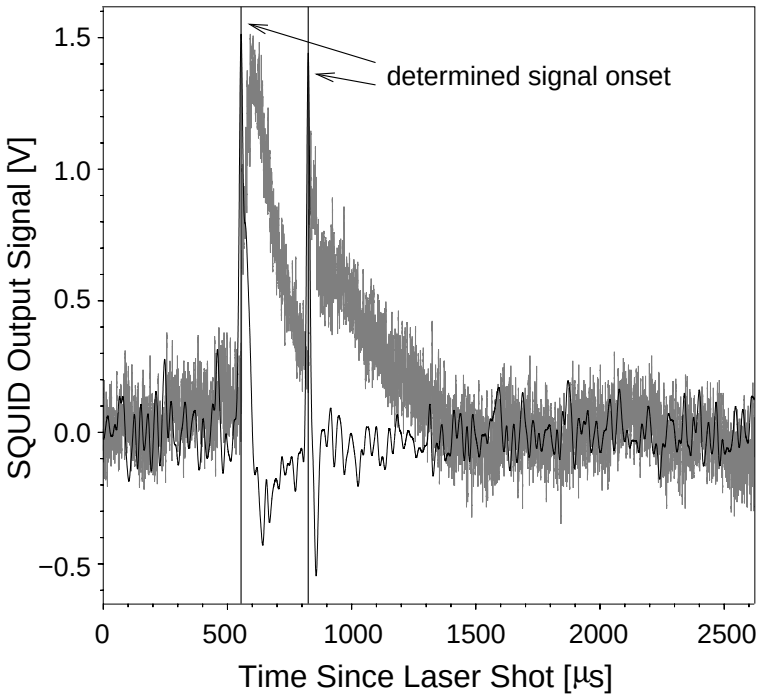

Figure 4.12: Onset time determination of an impact event with Gauss-filter method. Grey curve: shot record, black curve: Gauss-filtered shot record, vertical bars: determined onset times of events.

Wavelet Method

Wavelet analysis is a method of time dependent spectral analysis. For comparison, a discrete Fourier analysis of a shot record window treats the record window as an elementary cell of a periodic signal and represents a constant frequency distribution at all times inside the shot record window. Wavelet analysis instead scans through the record window and determines the varying frequency distribution at each recording time [Kai94].

For this a certain wavelet needs to be created. It may be of arbitrary shape except for a few prerequisites among which the most important is that its total integral must vanish. For spectral analysis a very suitable wavelet is the Morlet [Gou84] which is a complex wave dampened by a Gaussian,

$$\Psi_0(\tau) = e^{i\omega_0\tau} \cdot e^{-\frac{\tau^2}{2}} \tag{4.10}$$

where ω_0 is the wave number and τ is a dimensionless time. The convolution of the shot window with this wavelet $\Psi_o(\tau)$ results in the intensity distribution of the wave number ω_0 at all times in the shot window. Once the convolution is done for different wave numbers $\omega_0 = \omega_{min} \ldots \omega_{max}$ the frequency spectrum at all times is deduced in the given frequency range.

For the impact event analysis supposably a lot of information may be derived from this spectral analysis. One application of the wavelet method may be a spectrally resolved search for events in a shot. While the Gauss filter method selects patterns in a certain frequency band only, a search for more complex patterns would be possible in a wavelet spectrum. The search would not be limited to certain frequencies but could account for the development of the frequency spectrum with time. A more selective event detection, in terms of time accuracy as well as noise rejection, could be possible.

Chapter 5

Detector Development

5.1 Fabrication Process

Most of the detectors produced for this work were made of an Iridium/Gold (Ir/Au) proximity-effect bilayer film evaporated on an r-plane oriented sapphire crystal. Some detectors used for preliminary tests used other materials for the thermometer, as explained in the subsequent sec. 5.2.

Substrate Treatment The sapphire crystals had a size of $20 \times 10 \times 0.5\,\mathrm{mm}^3$. Before film evaporation, the substrates were cleaned rubbing them with Q-Tip sticks soaked first in acetone, then in isopropanol. Afterwards they were rinsed with deionised water and dried with nitrogen gas.

For manufacturing detectors with smaller dimensions, the crystals were cut by standard methods after the evaporation of the Ir/Au film. To protect the film, it was coated with photo-resist before cutting. Since the Ir/Au films are sensitive to inter-diffusion at higher temperatures, it had to be taken care that the samples did not heat up above $\sim 100\,^{\circ}\mathrm{C}$ during cutting.

Proximity-Effect Superconducting Film Evaporation For SPT thermometer films Ir/Au proximity-effect tri-layer films were used. Due to the proximity-effect the transition temperature of the iridium film can be lowered by bringing it in contact with a normal-conducting gold film. Usually this is done by evaporating an iridium film onto a gold film or vice versa. The fabrication of the Ir/Au proximity-effect films used here was investigated and described by [Hoe98],[Nag94] and [Sta00]. Besides the Ir/Au proximity-effect pair, others like Aluminium/Silver [Irw96], Molybdenum/Copper [Cho00] (a multilayer sandwich) or the Niobium/Silicon alloy [Jul97] are used by other groups.

The proximity-effect films were all evaporated in an Iridium/Gold evaporation system at the Technische Universität München. It is equipped with an electron-gun evaporation system in which different crucibles containing iridium powder

run No.	*CH410*	*CH425*
degass substate	45 min/350 °C	
adhesion layer (Ir)	5.0 nm/300 °C	5.0 nm/300 °C
Au film	60 nm/150 °C	10 nm/100 °C
Ir film	60 nm/25 °C	40 nm/20 °C

Table 5.1: Ir/Au film evaporation processes. For each layer thickness and substrate temperature during evaporation is given.

and gold wire can be chosen. The film thicknesses were measured with a quartz-crystal deposition thickness measurement device. The samples could be loaded and unloaded through a load lock without venting the evaporation chamber.

In each evaporation run four substrates were evaporated at a time. By cutting each substrate to several detectors, many detectors could be produced with one evaporation run.

Below the Ir/Au bilayer a thin iridium adhesion layer was evaporated at high substrate temperature since gold films show a poor adhesion on a sapphire substrate. After that the gold film was evaporated. The iridium film had to be evaporated last since it had to be evaporated at room temperature and must not be heated any more, e. g. by evaporating additional films. Gold atoms would inter-diffuse into the iridium film and prevent the proximity effect. In one evaporation run the substrate was de-gassed by heating it for 45 min prior to the start of the evaporation process. The evaporation runs are shown in Table 5.1.

After film evaporation and eventual cutting of the substrate, the SPT thermometers were structured by sputter etching. A photo-lithographic mask was developed on the film and the SPT was etched using an argon beam. Sputter etching was also done in a facility at the TU München.

Contact Pads To finish the detector layout, gold and aluminium contact- respectively bond-pads were sputtered onto the SPT. The aluminium pads are superconducting at the operation temperature of the SPT and are used for applying the measurement current via aluminium bond wires. Via the gold pad the thermal link to the heat bath is applied by gold bond wires. The shape of the bond pads was defined with lift-off masks.

The detectors were mounted in different types of holders, depending on the size of the detector, and were bonded to copper-capton pads for easy electrical connection in the cryostat. Pictures of some mounted detectors were already shown in the description of the cryostat setup in sec. 4.2.

5.2 Development of Detectors with a Fast Signal Rise

Since many years cryogenic calorimeters are developed for the application in Dark Matter searches, neutrino physics and a variety of other applications requiring high energy resolution. For these applications the cryogenic calorimeters were optimised for a low threshold and best energy resolution. High energy resolution was achieved by adjusting the time constants of the detector sufficiently long to get a most homogeneous response. In the present work, the detectors had to be optimised to obtain a fast response time. The time constants of the cryogenic calorimeters were subsequently reduced to achieve about $1\,\mu$s signal rise time.

In this chapter several detectors and tests that were made with them are presented. It covers preliminary tests which were made without the use of the TOF-MS setup. Results obtained by TOF-MS are the subject of the subsequent chapter.

The detector properties were studied by irradiating the detectors with radioactive sources and measuring their response in time (rise time) and amplitude (energy resolution). Several detectors were investigated to study the parameters influencing the time response. The detector size was subsequently reduced down to the size of the detectors actually used for TOF-MS. The section is concluded by a comparison of all detectors and their properties.

A first Detector, with an SPT made of Tungsten

In the beginning of the development of fast cryogenic detectors, detectors of well known dimensions should have been investigated to compare the achieved rise times and energy resolution with present results. The first detector shown in this chapter (named *CWBIO1*) is a $20 \times 10 \times 5\,\mathrm{mm}^3$ size calcium tungstate ($CaWO_4$) substrate with a superconducting tungsten film of $5 \times 3\,\mathrm{mm}^2$ size evaporated on it.

The transition temperature of the superconducting film is at $T_c = 24\,\mathrm{mK}$. The intrinsic transition temperature of tungsten is $T_C = 15\,\mathrm{mK}$. It was observed that tungsten films evaporated on the calcium tungstate crystals show an increased transition temperature, depending on the evaporation process. For reasonable operation of a detector in the TOF-MS it should be $T_C = 50 \ldots 150\,\mathrm{mK}$. It was considered that the transition temperature of the tungsten could be raised into this range by using a suitable evaporation process.

The detector shown here was first irradiated with a radioactive ^{55}Fe X-ray source which emits 5.89 keV and 6.49 keV K_α and K_β X-ray lines, respectively. The source was mounted to illuminate the $20 \times 10\,\mathrm{mm}^2$ plane opposite to the side carrying the SPT film (backside), using the $CaWO_4$ as absorber. A pulse height spectrum is shown in figure 5.1. The abscissa was scaled to the energy of the K_α line. The energy resolution in this measurement is limited by the low signal

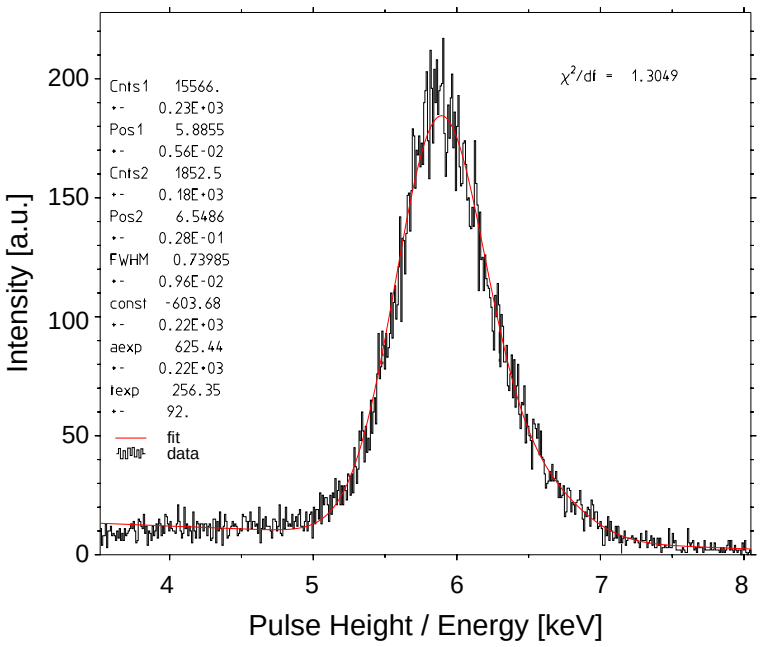

Figure 5.1: Energy resolution of the $\sim 6\,\mathrm{keV}$ K-shell lines of ^{55}Fe of detector *CWBIO1*

amplitude of only $\sim 0.1\,\mathrm{V}$ for the K-lines. It was about $E/\Delta E \approx 8$. The K_α and K_β lines cannot be resolved, though the fit in figure 5.1 indicates the presence of the K_β line at $6.49\,\mathrm{keV}$ with an intensity of $\sim 1/10$ of that of the K_α line.

The measurement above was repeated with an ^{241}Am source mounted outside the cryostat. ^{241}Am decays to excited $^{237}\mathrm{Np}^*$ by emitting a $5486\,\mathrm{keV}$ α particle which is absorbed in the plastic housing of the source (closed source). The $^{237}\mathrm{Np}^*$ emits $59.5\,\mathrm{keV}$ γ's ($35.9\,\%$) which are energetic enough to reach the detector inside the cryostat. The measured energy resolution of $E/\Delta E \approx 12$ is slightly better than the one measured with the ^{55}Fe source. This may be due to the increased signal amplitude (improved signal-to-noise ratio) in the latter measurement.

From a pulse-shape analysis the rise time of the detector pulses was determined. To remove the influence of background events (cosmic radiation and inelastically scattered $\gamma's$), events with an amplitude of $50-70\,\mathrm{keV}$, corresponding to the $59.5\,\mathrm{keV}$ γ-line, were selected. The rise time distribution of these events is shown in figure 5.2. The rise time was determined to be $\tau_{rise} = (155 \pm 18)\,\mu\mathrm{s}$. It is even somewhat shorter than the calculated ideal collection time $\tau_{coll} = 206\,\mu\mathrm{s}$. This can be explained by an inelastic decay of non-thermal phonons in the CaWO_4 crystal. Inelastic phonon decay, characterised by $\tau_{crystal}$, is a concurring process to the collection of non-thermal phonons in the SPT film with the time constant τ_{film}, as described by eqn. (2.3). For the detector here, $\tau_{crystal}$ and τ_{film} are of comparable size. To reduce the signal rise time, in a next step a detector with a smaller substrate was made on a silicon crystal.

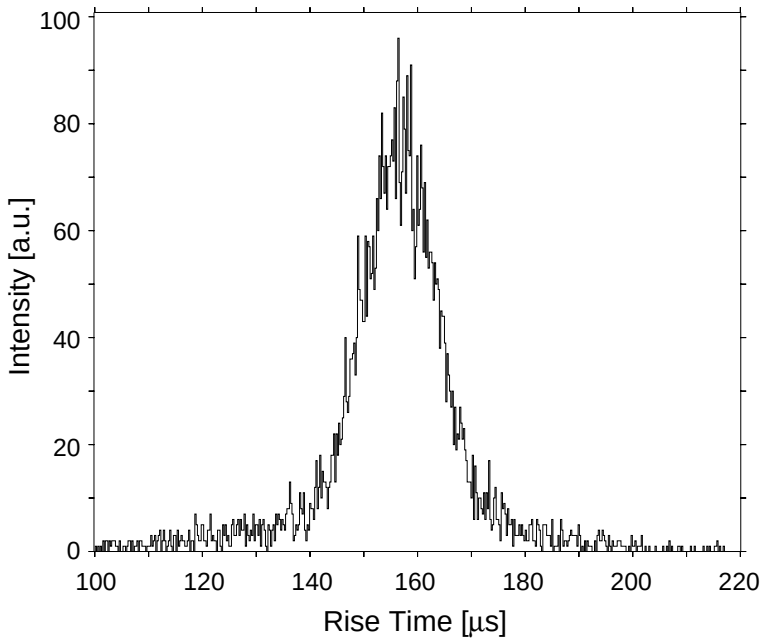

Figure 5.2: Rise time spectrum of detector *CWBIO1*, recorded with an ^{241}Am source. The rise times are smoothly distributed at $\tau_{rise} = (155 \pm 18)\,\mu$s.

Effects of an Inhomogeneous Phonon Distribution in the Substrate

A detector with a $3 \times 2\,\mathrm{mm}^2$ Ir/Au SPT with $T_C = 45\,\mathrm{mK}$, evaporated on a silicon crystal of $20 \times 10 \times 0.6\,\mathrm{mm}^3$ was investigated (detector *SI365*). Due to the smaller absorber volume the life time of non-thermal phonons as well as their ideal collection time τ_n, $\tau_{coll} \propto V/A$ was expected to be shorter than that of the detector described above. The measurement presented here was done with a ^{55}Fe source illuminating the backside of the absorber. Figure 5.3 shows the pulse-height spectrum of one such measurement. There is a main peak with a resolution of $E/\Delta E = 3.3$ at a pulse height of 1.1 V and a tail of events at amplitudes up to $\sim 2.7\,\mathrm{V}$. This tail contains about $1/10 - 1/20$ of the events, depending on where the cut is set, which have a shorter rise time of about $6\,\mu$s as shown in figure 5.4. The rise times of the main peak are distributed around $(21 \pm 12)\,\mu$s.

An explanation of this behaviour could be the spatial inhomogeneity of the detector response. If an X-ray is absorbed in the substrate in a certain distance from the SPT film, the non-thermal phonons will spread out and finally distribute homogeneously in the substrate. As long as the time constant for this homogenisation is much shorter than the life time of non-thermal phonons τ_n, the non-thermal phonons will be collected in the SPT film with τ_n.

When an X-ray is absorbed in the substrate right below the SPT film, more energy may be absorbed in the thermometer. While the non-thermal phonons will be reflected between the interface to the SPT film and the opposite surface

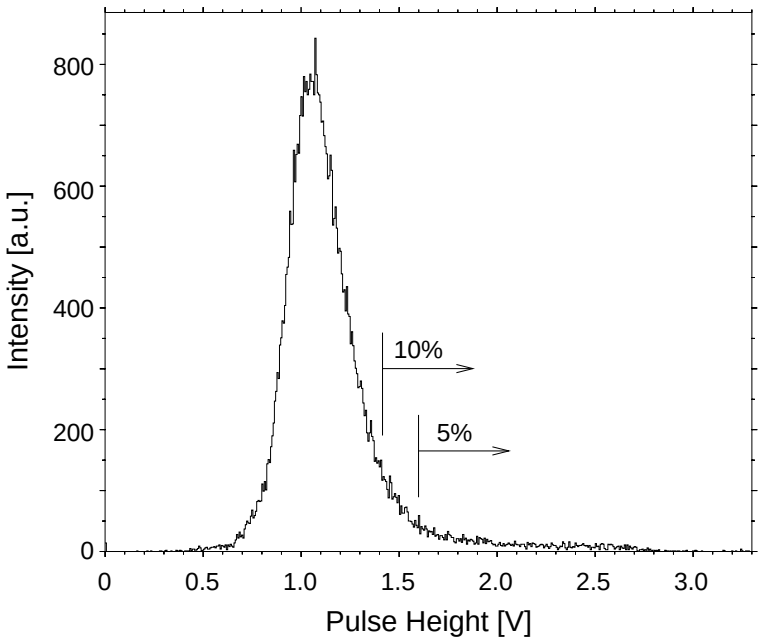

Figure 5.3: Pulse-height spectrum of detector *SI365*, measured with a ^{55}Fe X-ray source. $5 - 10\%$ of the events have an increased pulse-height.

of the substrate, there is a large probability for them to be absorbed in the SPT film. Only phonons which diffuse away from the SPT film without being absorbed will distribute in the substrate. Due to the smaller thickness of the absorber the diffusion constant of the phonons is reduced compared to the $CaWO_4$ detector. The probability for immediate absorption increases. The consequence of this is a higher signal amplitude and a faster signal rise.

If this model is correct, then the fraction of faster pulses with higher amplitude should roughly represent the area of the substrate being covered by the SPT film. For the detector here, where the SPT covers 3% of the substrate this seems to be in fair agreement.

This explanation is also supported by a Monte-Carlo simulation done for this detector. The signal amplitude and a collection time of non-thermal phonons were calculated for different impact spots of the X-ray in the absorber, independent of the detector model. This was done by a simulation of the phonon propagation and scattering in the substrate, with a certain absorption probability for phonon which hit the interface to the SPT film. It resulted in an almost constant amplitude and collection time for impact spots all over the substrate, except if the impact spot was below or close to the SPT film. There the amplitude was increased and the collection time decreased.

In summary, the detector shown here made it clear that a small SPT localised at a certain spot on the absorber surface will lead to an inhomogeneous rise time

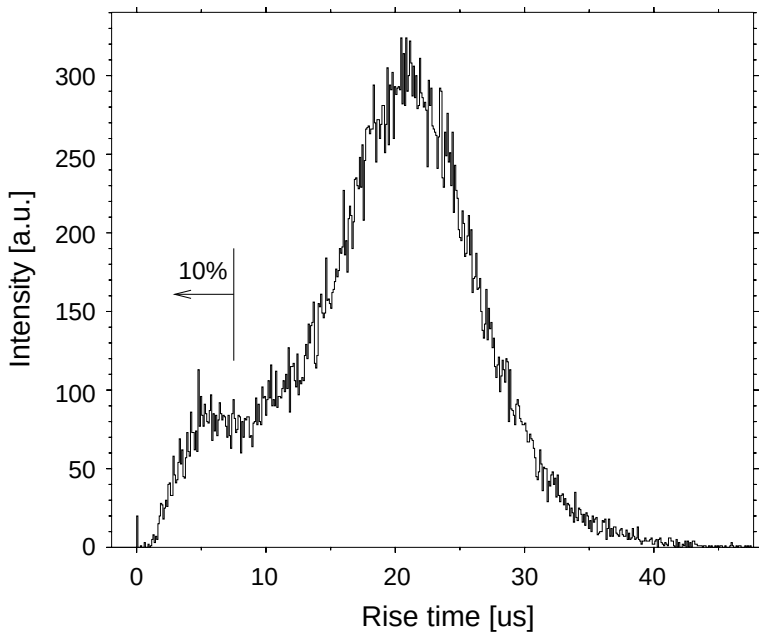

Figure 5.4: Rise time distribution of detector *SI365*, measured with X-rays of a ^{55}Fe source.

distribution, depending on the absorption place of the detected particle.

Spreading the SPT Across a Large Substrate Surface Area

The dispersion of non-thermal phonons in the substrate has shown to influence the signal rise of the detector. Additionally, for detectors used in TOF-MS the collection time of non-thermal phonons needs to be about 20 times less than it was for the before mentioned detector. In this case the influence of the phonon dispersion becomes even worse. However the influence can be minimised by spreading the SPT film across a larger area on the absorber substrate.

This was tested with another detector (*CH410A*). It was made of a sapphire substrate of $20 \times 10 \times 0.5\,\mathrm{mm}^3$, with an SPT ($T_C = 65\,\mathrm{mK}$) as sketched in figure 5.5. The V/A ratio was decreased from 20 (detector *SI365*) to 2.5, leading to a $\tau_{coll} = 2.2\,\mu\mathrm{s}$. In order to not increase the mass and thus heat capacity of the evaporated material, the SPT film was split into five strips of $0.4\,\mathrm{mm} \times 8\,\mathrm{mm}$ each, with 0.4 mm distance between them. Another positive effect of the strips may be that a magnetic field can penetrate between the strips as discussed in sec. 2.4.2 and the current is homogeneously distributed among all five strips [Maw01, Rho62]. The strip distance used should be large enough for this effect to take place. The five strips should ideally carry the same current $I_F/5$ each.

Since the SPT film is structured now, it is not possible to directly attach a thermal link to the heat bath to it. It would lead to an inhomogeneous rise time

and pulse shape distribution, dependent of the distance between the thermal link and the point where the phonons are absorbed in the SPT film. Instead, the detector was coupled to the heat bath via the substrate, by clamping it directly in a copper holder, without the usual thermal isolation by sapphire balls.

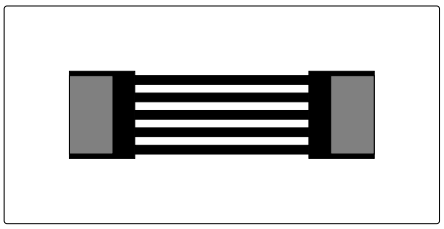

Figure 5.5: Sketch of detector *CH410A*.

For the measurements shown a ^{55}Fe X-ray source was used shining on the entire backside of the absorber. The energy resolution was quite poor, which may result from the indirect coupling via the substrate: Depending on the distance of the spot of X-ray absorption to the heat sink and the detector film, a different fraction of the non-thermal phonons escapes through the thermal link without being collected in the SPT. However the energy resolution is not as important for the TOF-MS detectors as the time behaviour.

The rise times show a quite broad distribution around $3.2\,\mu$s, as shown in figure 5.6. This is in fair agreement with the calculated value of $\tau_{coll} = 2.2\,\mu$s. It is already in an order of magnitude suitable for TOF-MS. The broad distribution of rise times up to $\sim 8\,\mu$s may be explained by the longest possible phonon diffusion path, which is from the edge of the substrate to the film strips. This distance is about 6 mm. Referring to sec. 2.4.1 this results in a diffusion time of about $8\,\mu$s. Thus particle interactions close to the edge of the substrate will result in signals with a relatively long rise time.

Another measurement, done with the X-ray source collimated by an aperture of $\varnothing\,2$ mm diameter below the strips, gives additional hints that diffusion in the substrate is responsible for the signals with long rise times. In this measurement the distribution of rise times was narrower and the tail of long rise times above $\sim 8\,\mu$s vanished. However, in this measurement some other things were changed at the detector, thus this is not completely conclusive.

Improving the Speed of the Detector Signal

With the last detector, a reasonable signal rise time has already been achieved. However the phonon collection time would be further improved by a larger SPT area (better V/A ratio). But since the signals of the above detector were already quite small, it is not reasonable to further increase the SPT film volume and thus its heat capacity. In turn to decrease V/A, detectors were made on a smaller

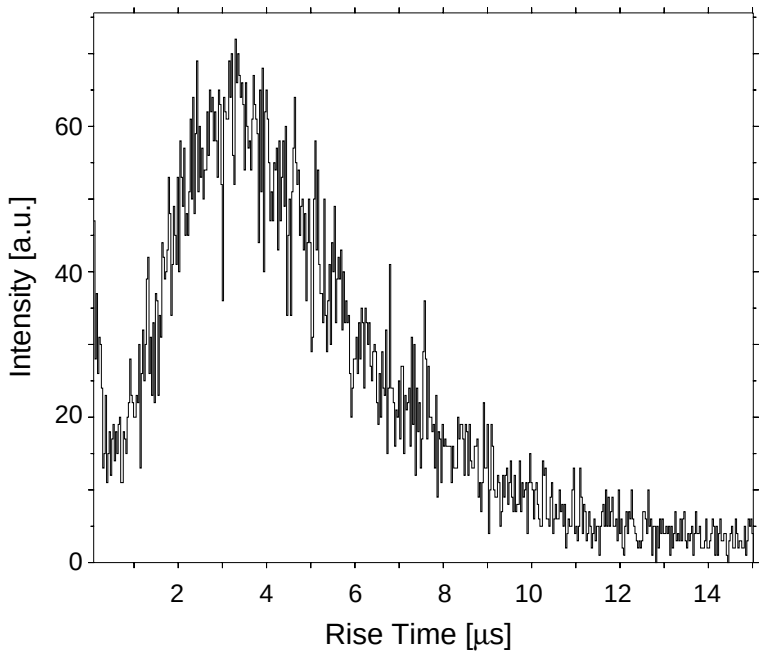

Figure 5.6: Rise time spectrum of detector *CH410A*.

substrate. Additionally, the time delay by diffusion of phonons in the substrate is decreased if it is smaller.

To produce smaller substrate dies, $20 \times 10 \times 0.5\,\mathrm{mm}^3$ standard sized substrates were cut into pieces of $10 \times 5 \times 0.5\,\mathrm{mm}^3$ size after the evaporation of the superconducting film. With these smaller substrates, the investigation of detectors which were truly usable for TOF-MS begun.

With the $10 \times 5 \times 0.5\,\mathrm{mm}^3$ sized detectors, several different shapes of patterning of the SPT film have been tested. All SPT films have an outer dimension of about $3.2 \times 2.8\,\mathrm{mm}^2$ plus some $\sim 1.5\,\mathrm{mm}^2$ area for contact pads. One detector *(CH410C1)* has a non-structured, plain $3 \times 3\,\mathrm{mm}^2$ SPT film. This is a well-known shape, made for comparison. The other detectors were structured with a hexagonal hole pattern inside the film, all similar to the one sketched in figure 5.7. The hole size as well as the hole distance were varied between the detectors. To distinguish them easily, they were named by the hole size and the hole distance. For example, the $350\,\mu\mathrm{m}/400\,\mu\mathrm{m}$ detector (*CH410B2*) has holes of the size $350\,\mu\mathrm{m}$ in a hexagonal pattern with a centre-to-centre distance of $400\,\mu\mathrm{m}$. All detectors are listed in Table 5.2 later.

All detectors were fitted with a gold frame (not shown in figure 5.7) which covers all the surface of the substrate around the SPT film. The detectors were clamped into their holders such that the heat link was provided via the clamps pressing on the gold frame. Additionally in many measurements the detectors were mounted with an aperture of $3 \times 3\,\mathrm{mm}^2$ size through which only the SPT

film was illuminated by the X-ray source.

The idea of this design was that phonons created in the absorber below the SPT film will be collected in the SPT film effectively and quickly. The fraction of phonons which escapes to parts of the substrate which are not covered by the SPT film, would produce a delayed signal since the phonons would diffuse forth, and back to the SPT film, before detection. The gold frame was applied to absorb most of these phonons so that the SPT film only collects and detects the fast ones.

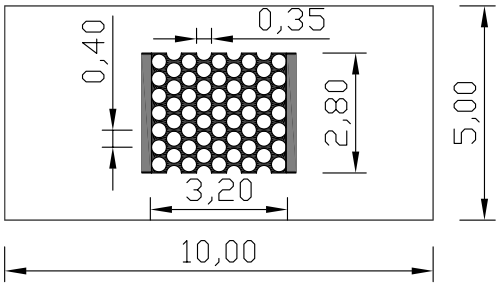

Figure 5.7: Sketch of the hole structure of the detector with 350 μm/400 μm sized holes (detector *CH410B2*).

In this setup, all detectors were investigated with ^{55}Fe X-ray sources. They had transition temperatures between 40 mK and 60 mK. It turned out that all detectors had their rise times distributed around $\tau_{rise} \approx 2 - 8\mu$s. On average, the $10 \times 5 \times 0.5\,\mathrm{mm}^3$ sized detectors were as fast as the detector with the strip structure above *(CH410A)*. One exception was a detector with 175 μm/200 μm sized holes (detector *CH410C2*), the rise times of which widely spread up to more than 20 μs.

The fastest of these detectors was the one with 250 μm/400 μm sized holes (detector *CH410B1*). The figures 5.8–5.10 show results from a measurement which was done without an aperture, the whole substrate was illuminated with X-rays. Figure 5.8 displays the pulse-height spectrum. The distribution of pulse heights is broad, as expected due to the indirect thermal coupling via the substrate. It has a maximum at an amplitude of ~ 0.15 V. Towards lower amplitudes, the intensity first decreases and then rises until the cut-off voltage of the trigger threshold.

The spectrum can be divided at the minimum of the distribution, into pulses having an amplitude more than or less than ~ 0.1 V. The pulses with an amplitude less than ~ 0.1 V have broadly distributed rise times, with a long tail to rise times far above 20 μs, shown in figure 5.9. They were related to hits distant to the SPT film.

In comparison, the rise time distribution of the signals with an amplitude higher than 0.1 V is much sharper, as shown in figure 5.10. Its peak is at 2.8 μs, with a FWHM of about 2 μs. These pulses were related to hits below or close to the SPT film. This is confirmed by the ratio of SPT film area to the total illu-

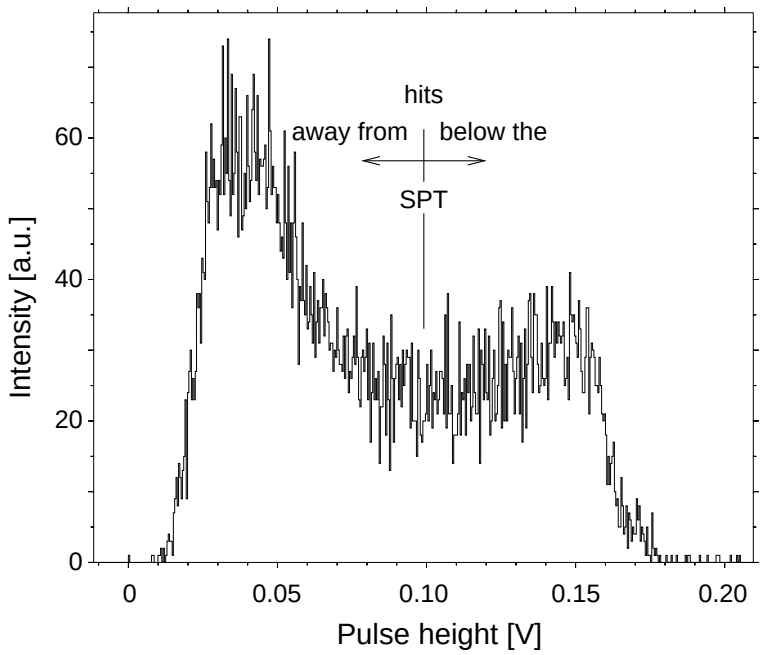

Figure 5.8: Pulse height spectrum of the detector with 250 μm/400 μm sized holes (detector *CH410B1*). Low-amplitude events are hits far away from from the SPT, high-amplitude events are hits below the SPT. A cut is shown dividing the two classes.

minated absorber area. It was also proven by measurements done with another detector (350 μm/400 μm sized holes, detector *CH410B2*), with and without an aperture of $3.0 \times 3.0\,\mathrm{mm}^2$ size in front of the SPT film. Yet the rise time distribution of the detector with 250 μm/400 μm sized holes are shown since this one happened to be the fastest of all the detectors on a $10 \times 5 \times 0.5\,\mathrm{mm}^3$ substrate — though the differences in speed were not really substantial.

The detector with the best energy resolution measured during this project up to now was a detector with 350 μm/400 μm sized holes (detector *CH410B2*). Its energy spectrum is shown in figure 5.11. The fit resulted in an energy resolution of $E/\Delta E = 15$. This measurement was taken using a copper aperture of $\varnothing\,1\,\mathrm{mm}$ diameter to collimate the X-rays on a spot in the centre of the detector film.

Since the rise times achieved with the $10 \times 5 \times 0.5\,\mathrm{mm}^3$ sized detectors were already in the order of magnitude suitable for TOF-MS, the test measurements were continued with the TOF mass spectrometer.

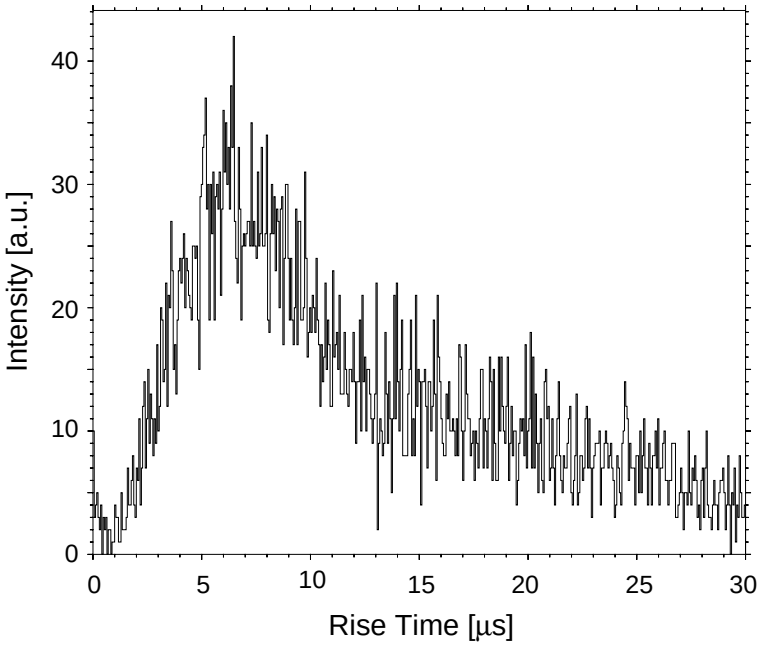

Figure 5.9: Rise time distribution of the detector with 250 μm/400 μm sized holes, for events with an amplitude < 0.1 V.

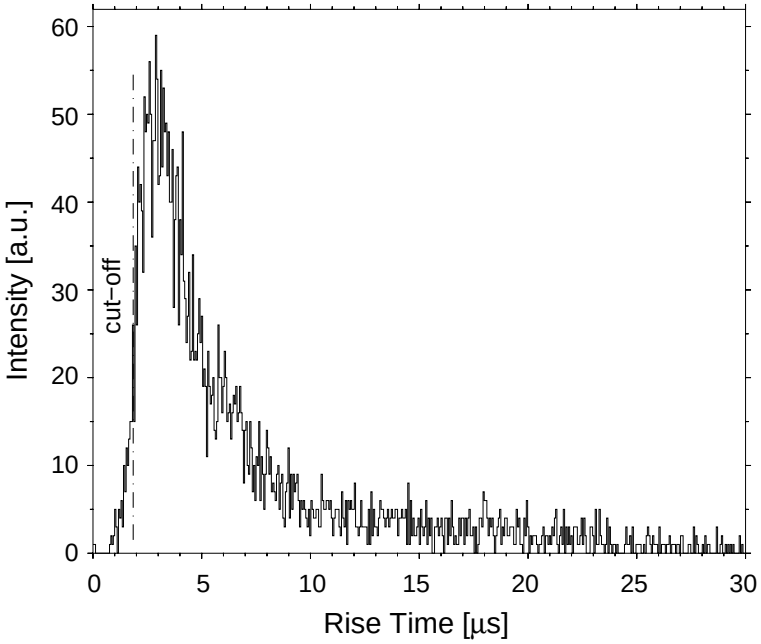

Figure 5.10: Rise time distribution of the detector with 250 μm/400 μm sized holes for the events with an amplitude > 0.1 V. The cut-off in rise time at $\sim 1.8\,\mu$s is possibly given by the bandwidth limit of the read-out circuit.

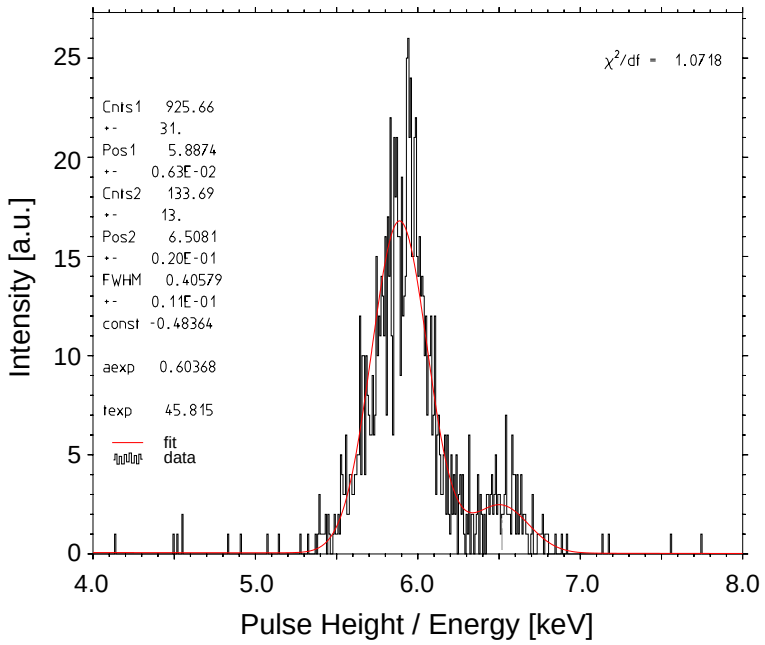

Figure 5.11: Pulse height distribution of the detector with 350 μm/400 μm sized holes (detector *CH410B2*), normalised to the ^{55}Fe K_α line. A relative energy resolution (FWHM) of $E/\Delta E = 15$ results from the fit. The X-ray beam was collimated using an aperture of $\varnothing$ 1 mm diameter.

Detectors used for Mass Spectrometry

With the $10 \times 5 \times 0.5\,\mathrm{mm}^3$ sized detectors the first detectors were developed which were actually used in the TOF-MS. From then on the emphasis of the detector development shifted from test with radioactive sources to measurements with simple, well-understood test proteins.

Plain Film Detector The first detector actually used for TOF-MS experiments was the detector with the plain $3 \times 3\,\mathrm{mm}^2$ SPT film (detector *CH410C1*). It had the highest operating temperature of 60 mK of all the $10 \times 5 \times 0.5\,\mathrm{mm}^3$ sized detectors and thus the highest chance of getting superconducting under the presence of a thermal radiation load from the MS. It was still necessary to improve the thermal coupling of the SPT to the heat sink. A gold pad and gold bond wires were bonded from the SPT to the heat sink to increase the transition temperature to $T_C \approx 40$ mK under the presence of heat radiation[1]. This is barely above the base temperature of the ADR cryostat of ~ 34 mK and reduced the

[1]Transition temperature, if not explicitly mentioned differently, always means the measured temperature of the detector holder when the thermometer film is in the transition. It varies with measurement conditions. The actual temperature of the superconducting film is always higher than this measured one, especially under the condition of thermal radiation load.

actual cycle life time to some hours. Succeeding detectors were fabricated with a higher transition temperature.

250 μm/400 μm Hole Structure The detector with the fastest rise time at that time was the detector with the 250 μm/400 μm hole structure. Since the transition temperature of that detector was too low to reliably operate it in the TOF-MS, another detector (*CH425D2*) with that structure was made. It had a transition temperature (without thermal radiation) of $T_C = 145\,\mathrm{mK}$ which was sufficiently high and allowed the operation of that detector above the cryostat's base temperature.

With the last two detectors the first MS measurements were done. The time resolution achieved in MS measurements will be discussed in sec. 6.2.

A Detector with Gold Absorber Another detector design which was briefly tested was a design using a gold absorber pad instead of the substrate or the SPT film as molecule absorber. It was used in detector *CH425D1*. This was a detector on a $20 \times 10 \times 0.5\,\mathrm{mm}^3$ substrate. It consisted of an SPT film of $3 \times 0.5\,\mathrm{mm}^2$ size with $2 \times 2\,\mathrm{mm}^2$ square 250 nm thick gold pads at each end of the SPT film. The gold pads were used as absorbers. After a molecule impact, the energy would diffuse through the gold pad to the SPT film and heat up the SPT film. The disadvantage of this design is the limited area of the gold pads, since the diffusion time in the gold pad is crucial. The diffusion time lowers with rising thickness of the pad, on the other hand a thick gold absorber owns a high heat capacity and reduces the signal amplitude. Thus a minimum thickness and a maximum volume of the pad limit its area. The detector with gold absorber pads was used for detector rise time and MS time resolution measurements in sec. 6.2. It happened to show no advantage in terms of speed but has a limited absorber size.

Detectors on $3.0 \times 3.0 \times 0.5\,\mathrm{mm}^3$ sized Substrates In the end it became more and more clear that none of the structures of the SPTs gave a significant improvement of detector speed. The more important factor for detector speed still seems to be the collection time of non-thermal phonons and the ratio V/A. On the other hand a simple SPT film without holes gives the possibility of directly using the SPT film as absorber, avoiding the substrate and its phonon collection processes.

For these reasons, a detector was made on a substrate of $3.0 \times 3.0 \times 0.5\,\mathrm{mm}^3$ size with one side fully covered with a $3.0 \times 3.0\,\mathrm{mm}^2$ SPT film (detector *CH425C1*). The SPT was an Ir/Au thermometer out of a 5 nm iridium sticking layer, a 10 nm gold and a 40 nm iridium proximity effect film. Its film resistance was measured with the method described in appendix A to be $R_N = 110\,\mathrm{m}\Omega$. This corresponds to an electric conductivity of $\sigma = 1.65 \cdot 10^8\,(\Omega\mathrm{m})^{-1}$. The heat capacity of the SPT

film is given by the thicknesses of the gold film and the iridium films, whereas for the latter a molar specific heat of $3.1\,\mathrm{mJ/(molK^2)}$ [Kit80] for the normal-conducting iridium was assumed. With this $c_{el} = 308\,\mathrm{J/(m^3K^2)} \cdot T$. Most of the TOF-MS results presented in chapter 6 were done with this detector.

5.3 Discussion of Rise Times

Table 5.2 shows an overview of all detectors with their measured rise times. The table also includes two detectors investigated by M. Sisti in [Sis99] for comparison. With these detectors, the table spans the whole range of detector sizes of cryogenic calorimeters of this type investigated up to now. The table lists all detectors with their substrate material, SPT film material, layout and measured rise time. The rise times given for the two detectors *SISTI#1* and *SISTI#3* are the means of the measured values given in [Sis99]. The given error is the standard deviation corresponding to the mean value. For the other detectors the given rise times are the peak value and the width FWHM of the distribution of the particular measurement. For detectors for which the shape of the distribution was very asymmetric, the maximum and the half-maximum widths of the distribution are given. For detector *CH425D2* no measurements were taken with radioactive sources. It was used in the TOF-MS only.

The SPT areas and the V/A values in parenthesis in Table 5.2, for the detectors with gold frame on $10 \times 5 \times 0.5\,\mathrm{mm^3}$ sized substrates, are the values of the SPT film only, neglecting the gold frame around the SPT. The area of the contact pads is listed separately. The calculation of V/A is different for these detectors as well. They are assumed to operate in a way that they collect all phonons as long as the phonons are below the SPT film. Phonons which leave the area below the SPT film without being absorbed escape into the heat sink via the gold absorber frame. Thus according to sec. 2.3.2 it is assumed that V/A can be represented by the area of the SPT film δA, given in the table, and the substrate volume δV below the SPT. The $\delta V/\delta A$ of the distinct SPT films then only differs by an "effective surface allocation" due to the different hole structures. Of course this is only an approximation.

The rise times of all the detectors are plotted in figure 5.12 versus the V/A values. The crosses with error bars represent the measured rise times τ_{rise} of Table 5.2. According to the detector model of sec. 2.2 they should represent the life time of non-thermal phonons τ_n. The straight lines are the ideal collection times of non-thermal phonons $\tau_{coll} = 2V_a/(A < v_\perp \alpha >)$. They are given for the different absorber $\rightarrow$ SPT material pairs, according to the insert in figure 5.12. τ_{coll} differs from τ_n by the absorption probability $\bar{\eta}$ and by $\tau_{crystal}$, the probability of thermalisation of non-thermal phonons in the absorber crystal. Both can not be reliably calculated. The latter can be expressed in relation to τ_{film} by a

Detector	SPT layout	Substrate material	Substrate size V/mm^3	SPT metal	SPT area A/mm^2	V/A mm	measured τ_{rise}/μs
SISTI#1 [a)]	plain 9×13	Sapphire	$40 \times 40 \times 41$	W	117	561	430 ± 49
SISTI#3 [a)]	plain 8×9	Sapphire	$40 \times 40 \times 41$	W	72	911	635 ± 24
CWBIO1	plain 3×5	$CaWO_4$	$20 \times 10 \times 5$	W	15.00	66.7	155 ± 18
SI365	plain 2×3	Silicon	$20 \times 10 \times 0.6$	W	6.00	20	21 ± 12
CH410A	Fingers	Sapphire	$20 \times 10 \times 0.5$	Ir/Au	$16 + 24$	2.50	$3.2(+2.7 - 1.6)$
CH410C1	plain 3×3	Sapphire	$10 \times 5 \times 0.5$	Ir/Au	$(9 + 1.5)$	(0.5)	$4.0(+1.6 - 0.8)$
CH410B1	holes 250/400	Sapphire	$10 \times 5 \times 0.5$	Ir/Au	$(5.87 + 1.12)$	(0.76)	$2.8(+1.7 - 0.8)$
CH410B2	holes 350/400	Sapphire	$10 \times 5 \times 0.5$	Ir/Au	$(2.90 + 1.12)$	(1.54)	$4.5(+3.0 - 2.5)$
CH410C2	holes 175/200	Sapphire	$10 \times 5 \times 0.5$	Ir/Au	$(2.83 + 1.12)$	(1.58)	$7.0(+20 - 3.0)$
CH425D2	repeat 250/400	Sapphire	$10 \times 5 \times 0.5$	Ir/Au	$(5.87 + 1.12)$	(0.76)	N.A.
CH425D1	Au absorber	Sapphire	$10 \times 5 \times 0.5$	Ir/Au	$7 + 1.5$	2.94	2.0 ± 0.8 [b)]
CH425C1	plain 3.0×3.0	Sapphire	$3 \times 3 \times 0.5$	Ir/Au	$3 \times 3 = 9$	0.50	1.3 ± 0.4 [b)]

Table 5.2: Overview of detector designs and rise times.
[a)] source: [Sis99]; τ_{rise} is mean over all measurements, error is stdev.
[b)] see sec. 6.2 below.

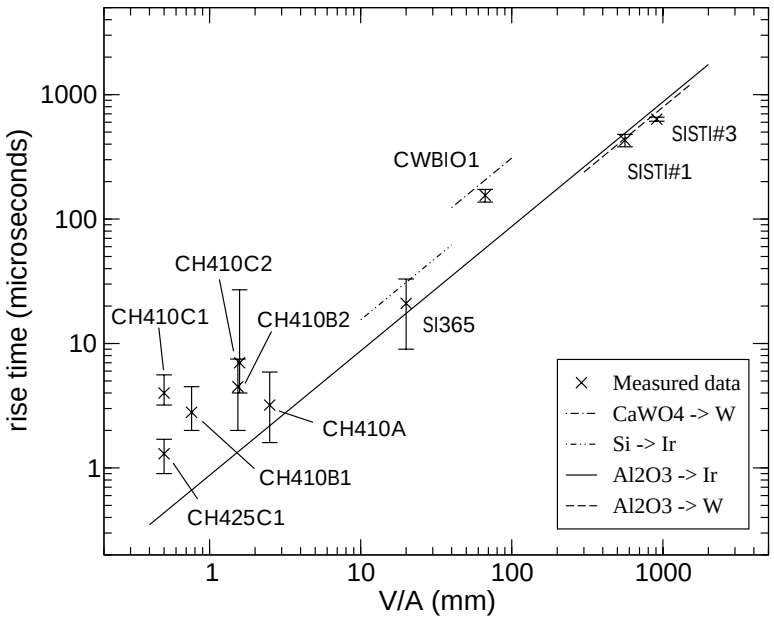

Figure 5.12: Measured rise times τ_{rise} (marks with error bars) and ideal phonon collection times τ_{coll} (lines) versus the V/A values of all detectors. The lines are calculated for different substrate → SPT material pairs (transmission from → to).

fraction

$$\varepsilon = \frac{\tau_{crystal}}{\tau_{film} + \tau_{crystal}} \,. \tag{5.1}$$

This changes eqn. (2.3) to $\tau_n = \varepsilon\tau_{film} = (\varepsilon/\bar{\eta}) \cdot \tau_{coll}$.

If the thermalisation time of non-thermal phonons in the crystal is negligibly long (see sec. 2.2.1), $\tau_{crystal} \gg \tau_{film}$, then $\varepsilon \to 1$. $\bar{\eta}$ is expected to be $\bar{\eta} \approx 0.3$ as discussed in sec. 2.2.3. Assuming that for the small-sized detectors used in this work the thermalisation of non-thermal phonons in the crystal can be neglected, the discrepancy between the measured rise time τ_{rise} and τ_{coll} is $\bar{\eta}$ and τ_{rise} may be up to three times longer than τ_{coll}. The measured rise times are in fair agreement with τ_{coll} over three orders of magnitude of V/A.

For the two detectors *SISTI#1* and *SISTI#3* the calculated τ_{coll} (dashed line) and the measured τ_{rise} are almost equal. This is explained by the fact that $\bar{\eta}$ and ε calculated by [Sis99] are equally high and $\varepsilon/\bar{\eta} \approx 1$. For example [Sis99] determines $\bar{\eta}_{\#1} = 0.76$ and $\varepsilon_{\#1} = 0.84$, $\bar{\eta}_{\#3} = 0.8$ and $\varepsilon_{\#3} = 0.68$.

The detectors *CWBIO1* and *SI365* have rise times shorter than τ_{coll} (dash-doted and dash-dot-doted line, respectively). With $\bar{\eta} < 1$ by definition, this shows that $\tau_{crystal}$ for these detectors seems to be comparable to τ_{coll}. The measured life time of non-thermal phonons τ_n is reduced by $\tau_{crystal}$ according to eqn. (2.3).

The measured τ_{rise} of the detectors with gold frames, on $10 \times 5 \times 0.5\,\mathrm{mm}^3$ sized substrates (detectors *CH410C1*, *CH410B1*, *CH410B2*, *CH410C2*, *CH425D2*), are

plotted versus the assumed $\delta V/\delta A$. Then all four detectors appear to have a longer rise time than given by the model τ_{coll}. However if $\varepsilon \approx 1$ a measured τ_{rise} three times higher can be explained by an $\bar{\eta} \approx 0.3$ as discussed. On the other hand is seems like the phonon collection with the gold frame did not work as expected and τ_{rise} seems to be given more by the actual V/A than by $\delta V/\delta A$.

The $3.0 \times 3.0 \times 0.5\,\mathrm{mm}^3$ sized detector (*CH425C1*) is the fastest one. Since it has one of its surfaces fully covered with the SPT film, almost half of the substrate surface is covered. Besides this optimisation of V/A, this also suggests that inelastic phonon surface scattering in the substrate is suppressed compared to phonon collection in the SPT and $\varepsilon \approx 1$. Thus for this detector $\bar{\eta} \approx \tau_{coll}/\tau_{film} = 0.38$ is in fair agreement with sec. 2.2.3. It is also possible that the measured rise time of this detector was in fact limited by the L/R time constant of the readout circuit. At least this possibility cannot be fully ruled out.

Chapter 6

Mass Spectrometer Results

In this chapter the measurements characterising the final TOF-MS setup are presented. It starts with a measurement trying to estimate the actual thermal radiation load on one of the cryogenic detectors. The major part of the chapter deals with time-of-flight measurements. The current time resolution, mass separation and energy resolution are presented. Following, measurements of heavy proteins and polymers are shown. The chapter concludes with a measurement of the current sensitivity threshold of the developed TOF-MS.

6.1 Thermal Radiation Load on the Detector

This section is split in two parts. First the absorption of heat radiation in the cryogenic detector is calculated. By this value and the temperature increase of the SPT film the thermal coupling of the detector to the heat bath is determined. This is done for two operating modes of the detector, using the substrate as absorber and directly shooting on the thermometer film. In the second part the obtained thermal coupling of the detector will be compared with the one calculated from the known thermal coupling of the used gold wires.

Heat Absorption

An important factor for the operation of cryogenic detectors in the mass spectrometer is the amount of heat load they receive by the thermal radiation entering the cryostat through the snout aperture. It was investigated in detail for detector *CH425C1* which was measured in three different setups. First in the well-known operating mode of using the substrate as particle (molecule) absorber, thus irradiating the substrate with the "hot" thermal radiation from outside the cryostat. Second the detector was turned round so that particles and thermal radiation hit its SPT thermometer film. And third the cryostat snout was closed to shield the detector from any external thermal radiation. The last measurement was done to achieve the transition temperature of the detector in absence of external heat

CH425C1	T_C	ΔT_C	$P_{Det}^{100\,\mathrm{K}}$	P_{Abs}	G_{eb}^{heat}	G_{Au}^{meas}
measurement	mK	mK	nW	nW	$\frac{\mathrm{nW}}{\mathrm{K}}$	$\frac{\mathrm{nW}}{\mathrm{K}}$
substrate	82	71	1.13	0.85	12.0	$4 \cdot 230$
film	129	24	1.13	0.30	14.4	
closed snout	153		≈ 0			

Table 6.2: Values obtained by the measurement of external thermal radiation onto detector *CH425C1*. For description see text.

load. The measurement current was in all cases $0.1\,\mu$A which gives negligible joule heating and transition temperature rise to the SPT film, since even with a ten times higher current no shift in transition temperature was observed.

Between all measurements the cryostat was never disconnected from the mass spectrometer, neither was the snout setup changed, since it would not be possible to rearrange an exactly identical alignment again.

The first column of Table 6.2 shows the measured transition temperatures in the three different cases. The transition of the closed snout case showed a width of only 1 mK, the film shot and absorber shot case transitions had a width of 6 mK and 20 mK, respectively. For calculations, the middle values of the temperature ranges were taken.

The entrance aperture of the snout had a diameter of 8 mm. Additionally a cold aperture of $3.0\,\mathrm{mm} \times 1.5\,\mathrm{mm}$ size had to be mounted in front of the detector to halve the heat load, since without it no transition could be observed in the substrate shot case. For all calculations a black body temperature of 100 K was assumed for the environment outside the cryostat. This is the temperature measured at the tips of the liquid-nitrogen cooled tube in the mass spectrometer and at the cryostat snout which are stuck together in normal operation. Additionally taking into account the Lambertian angular characteristic of the snout entrance as a black body emitter and the distance to the detector of 60 cm, the radiation power onto the detector calculates to

$$P_{Det}^{100K} = 1.13\,\mathrm{nW}\,. \tag{6.1}$$

From the absorption and reflection curves of sapphire shown in sec. 3.1.2 it can be seen that the reflection at $\lambda_{max}(100\,\mathrm{K}) = 29\,\mu$m is about $\sim 25\%$, whereas the transmission through the 1 mm thick detector is almost zero. In other words about 75% of the thermal radiation are absorbed in the detector crystal, which is $P_{Abs}^{sub} = 0.85\,\mathrm{nW}$. The absorbed power is conducted to the heat bath via the coupling G_{eb}, causing a temperature difference of $\Delta T_C^{sub} = 71\,\mathrm{mK}$. Thus the thermal coupling of the thermometer film needs to be $G_{eb}^{heat,sub} = 12.0\,\mathrm{nW/K}$.

Looking at the case of direct film shot, the temperature difference ΔT_C^{film} is 3.0 times lower than in the substrate shot case. Since the temperature of the

heat bath changes, the thermal coupling G_{eb}^{heat} changes as well[1]:

$$G_{eb}^{heat}(\bar{T}^{film}) = G_{eb}^{heat}(\bar{T}^{sub}) \cdot \frac{\bar{T}^{film}}{\bar{T}^{sub}} = 1.2 \cdot G_{eb}^{heat}(\bar{T}^{sub}) = 14.4\,\mathrm{nW}/K\,, \qquad (6.2)$$

where $\bar{T}^{film}$ and $\bar{T}^{sub}$ are the average temperature $\bar{T}$ across the thermal link G_{eb} for the case of irradiation the SPT film and the substrate respectively. $\bar{T}$ is given by the temperature T_{high} of the hot end and T_{low} of the cold end of the thermal link by $\bar{T} = (T_{high} + T_{low})/2$. The radiation absorption of the detector film can now be calculated as

$$\frac{P_{film}}{P_{Det}} = \frac{1}{P_{Det}} G_{eb}(\bar{T}^{film}) \Delta T^{film} = \frac{1}{P_{Det}} G_{eb}(\bar{T}^{sub}) \frac{\bar{T}^{film}}{\bar{T}^{sub}} \Delta T^{film} \qquad (6.3)$$

$$= \frac{1}{P_{Det}} P_{Det} \cdot 0.75 \frac{\bar{T}^{film}}{\bar{T}^{sub}} \frac{\Delta T^{film}}{\Delta T^{sub}}\,. \qquad (6.4)$$

It only depends on the measured temperatures and the radiation absorption of the sapphire crystal and calculates to

$$P_{film} = 0.30 P_{Det}\,. \qquad (6.5)$$

This rest absorption of 30% of the irradiated power takes place in the SPT film, where electric and magnetic fields enter on the length scale of a penetration depth d^{em}, and in the sapphire crystal behind the film by radiation which is not damped through the film thickness. For detector *CH425C1* the film thickness $d_{film} = 55\,\mathrm{nm}$ equals about two $d^{em} \approx 26\,\mathrm{nm}$ which means that only few percent of the incoming radiation pass through the film, the rest is reflected or absorbed.

Thermal Coupling

Above, the thermal coupling of the SPT thermometer film was calculated to be $G_{eb}^{heat} = 12.0\,\mathrm{nW/K}$ in the case of irradiating the substrate. This thermal coupling must be provided by the gold wires thermally connecting the thermometer film to the heat bath. For the measurements here detector *CH425C1* was connected by 4 gold wires (type AW7, distributor Müller Feindraht AG Thalwil/Switzerland) with a length of $\sim 0.7\,\mathrm{cm}$ and a resistance $R(4.2\,\mathrm{K}) = 18\,\mathrm{m\Omega/cm}$ each. Their

[1] For the temperature drop discussed here being not negligible compared to the absolute temperature of the body, i.e. $T_{high}^2 - T_{low}^2 \ll T_{high} \cdot T_{low}$ not being fulfilled, the heat flow equation $\dot{Q} = -\alpha A T \frac{dT}{dx}$ ($\dot{Q}$ the energy flow per unit time, α a conductance coefficient, A the cross sectional area perpendicular to the heat flow) needs to be solved exactly and results in $\dot{Q} = G(\bar{T})\Delta T$ with $G(\bar{T}) = -\alpha \frac{A}{\Delta l}\bar{T}$, $\Delta T = T_{high} - T_{low}$, Δl the length along which the temperature drop ΔT takes place, and $\bar{T} = \frac{T_{high}+T_{low}}{2}$, i.e. $G(\bar{T})$ must be calculated at the mean temperature $\bar{T}$ between the hot and the cold end of the body.

heat conductance was calculated to be $G_{Au}^{sub} = 4 \cdot 230\,\mathrm{nW/K}$ which is 77 times more than G_{eb}^{heat}.

This implies that the major part of G_{eb} is provided by additional thermal resistances. They are found in parasitic thermal couplings at the bond points of the gold wires on the thermometer film. The gold bond pad has a thickness of 400 nm and a width of 0.2 mm, thus the cross sectional area is strongly reduced compared to the gold wires of $\varnothing\, 25\,\mu$m diameter. Additionally the heat of the thermometer film needs to be collected in the gold bond pad, thus it has to flow through the thermometer film to the gold pad. The thermal conductivity of the thermometer film is also low, given by its small cross sectional area of $3.0\,\mathrm{mm} \times 55\,\mathrm{nm}$.

The latter is approved by the increase in transition width with increasing heat load. A temperature gradient evolves across the thermometer film, being higher at presence of higher heat load. With changing the operating temperature the normal-conducting area of the film shrinks or expands, defining the transition width.

Also others ([Sis99]) have measured parasitic couplings - translated to the temperatures here - of as low as $G_{par} = 12\,\mathrm{nW/K}$ per gold wire[2], dominating the total G_{eb}.

Additionally one should mention that once a parasitic coupling $G_{par} \ll G_{Au}$ is present, G_{Au} is additionally reduced since the main temperature drop occurs at G_{par} and the gold wire is at the temperature of the heat bath over its full length — $G_{Au} \to G(\bar{T}) \cdot T_{low}/\bar{T}^{sub} = G(T_{low})$, which is about 1.4 times less.

On the other hand one could consider the absorbed detector power to be higher than the calculated value. The integrated spectral flux of the Planck distributed radiation being absorbed in the sapphire crystal is hard to estimate and may vary between 60% and 80%, giving a small correction to P_{sub}.

But of more interest are variations in thermal radiation power entering the cryostat. Inside the snout tube, infrared radiation coming from the entrance aperture may not be absorbed at the tube walls but be reflected and guided through the snout. These reflections may achieve a quite high efficiency since they take place under a shallow angle of incidence. To prevent reflections, a labyrinth of additional baffles needs to be placed inside the snout as displayed in figure 6.1a). They must not disturb the line-of-sight of the detector, but back-scatter radiation coming from the entrance aperture instead of allowing small-angel reflections. Since in the measurements here a quite large entrance aperture was chosen it was not possible to machine useful baffles for inside the snout. Instead a spiral was wound out of copper wire of $\varnothing\, 1.2\,\mathrm{mm}$ diameter which was inserted into the snout as shown in figure 6.1b). Since the copper wire has a certain thickness, reflection at flat incidence still can take place at its surface

[2] [Sis99] measures $G_{par}(21\,\mathrm{mK}) = 4.4\,\mathrm{nW/K}$ for Detector #1, with 2 gold wires. $\Rightarrow G_{par}(\bar{T}^{sub}) = 0.5 \cdot G_{par}(21\,\mathrm{mK}) \cdot \bar{T}^{sub}/21\,\mathrm{mK} = 12\,\mathrm{nW/K}$

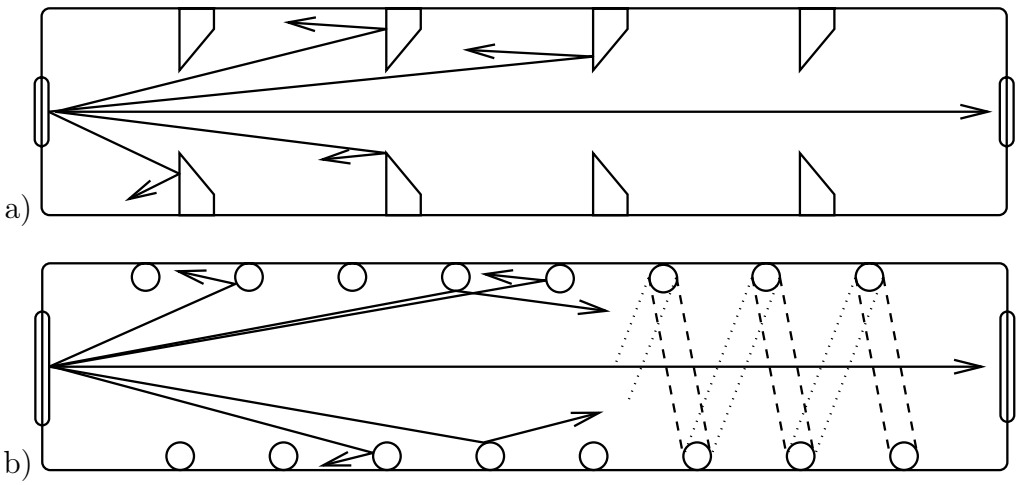

Figure 6.1: Sketch of the baffle arrangement inside the snout, preventing small angle reflection of infrared radiation at the snout walls. a) baffles labyrinth with good absorption qualities, b) baffle spiral for large aperture diameters, with reduced absorption quality.

directed to the snout. One may imagine from this that the radiation power at the detector place might be twice as high as calculated.

In addition it is as well possible that the temperature of the thermal radiation entering the cryostat is higher than the expected 100 K. This happens if residual thermal radiation of surroundings at room temperature shines into the liquid-nitrogen cooled parts of the mass spectrometer, directly onto the entrance aperture or indirectly via reflections at inherently cooled surfaces. A part where this may happen is the cooled ion mirror. First, there needs to be an orifice in the cooled surfaces to let the ion beam enter. Room-temperature heat radiation as well enters this orifice and may be reflected at the back plane of the ion mirror. Second, the ion mirror is operated at a high electric potential and thus the cooled metal surface additionally needs to be interrupted for electrical isolation. Due to the strong temperature dependence of the thermal radiation power, a shift of the mean radiation field temperature of only 20 K to 120 K already leads to an increase of the radiation power by a factor of 2.

In summary the real heat load on the detector and thus the heat conductance to the heat bath may be about four times higher than calculated above, $G_{eb}^{new} \approx 50\,\mathrm{nW/K}$. This thermal conductance needs to equal the thermal coupling given by parasitic thermal resistances and the gold wires $G_{Au}/1.4$. Since the heat conductance of the gold wire is more than ten times better than G_{eb}^{new}, it accounts for only $\sim 10\%$ of the total value. The remaining part is that of parasitic thermal resistances and is about

$$G_{par} \approx 55\,\frac{\mathrm{nW}}{\mathrm{K}}\,. \tag{6.6}$$

Having four gold wires in parallel, each wire provides a fraction of the parasitic heat conductance of $G_{par}^{1wire} \approx 14\,\frac{\mathrm{nW}}{\mathrm{K}}$. This is in agreement with the values measured by [Sis99].

6.2 Time Resolution

Since the time resolution of the cryogenic calorimeter is independent of the total time-of-flight of the proband molecules, it can be measured also with light ions. For the measurements here gold ions were used which have been ablated from a piece of gold foil, using the source in LDI mode without a matrix. Gold atoms have the advantage that their mass is well defined since only one stable isotope exists, whereas in macromolecules the measured mass peak may be broadened by the intrinsic presence of different isotopes. Additionally macromolecules tend to fragment and broaden the measured mass peak. To prevent these uncertainties gold atoms were used as calibration standard for investigating the time resolution.

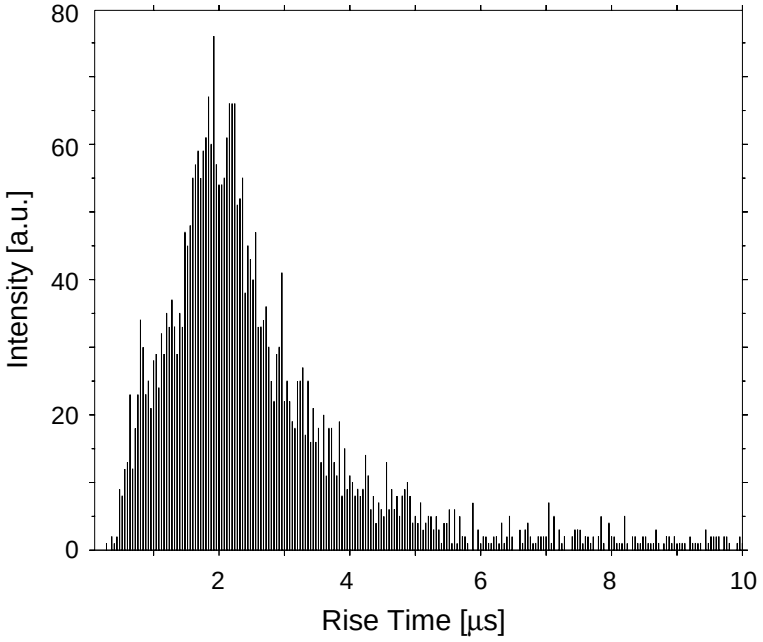

Figure 6.2: Rise time spectrum of detector *CH425D1*.

Figure 6.2 shows a distribution of signal rise times actually achieved in a measurement of gold atoms with detector *CH425D1*. The plot shows the time in which the signal amplitude rises from 10% to 90% of the maximum value of an event (10%–90% rise time).

About 10000 laser shots were recorded. They were off-line scanned with the data analysis program for pulses due to particle impacts. To filter good detector

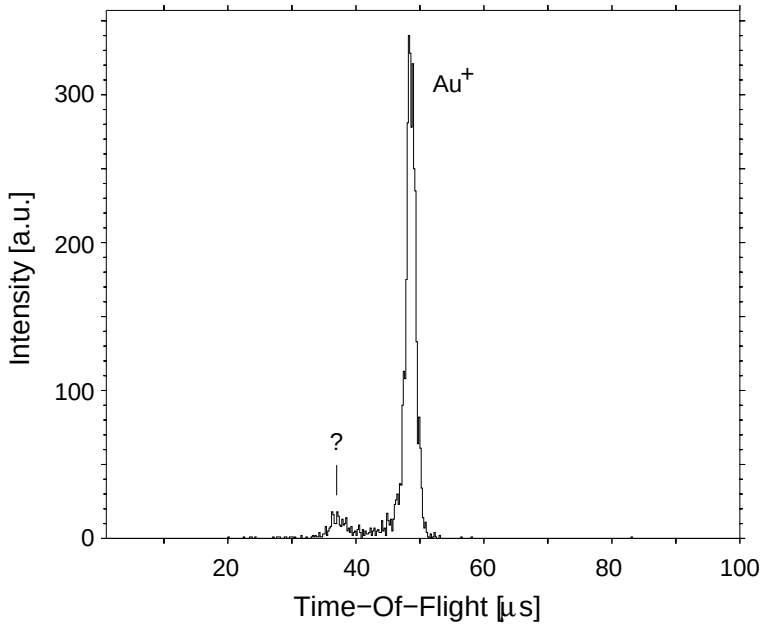

Figure 6.3: Time-of-flight spectrum of gold atoms recorded with detector *CH425D1*.

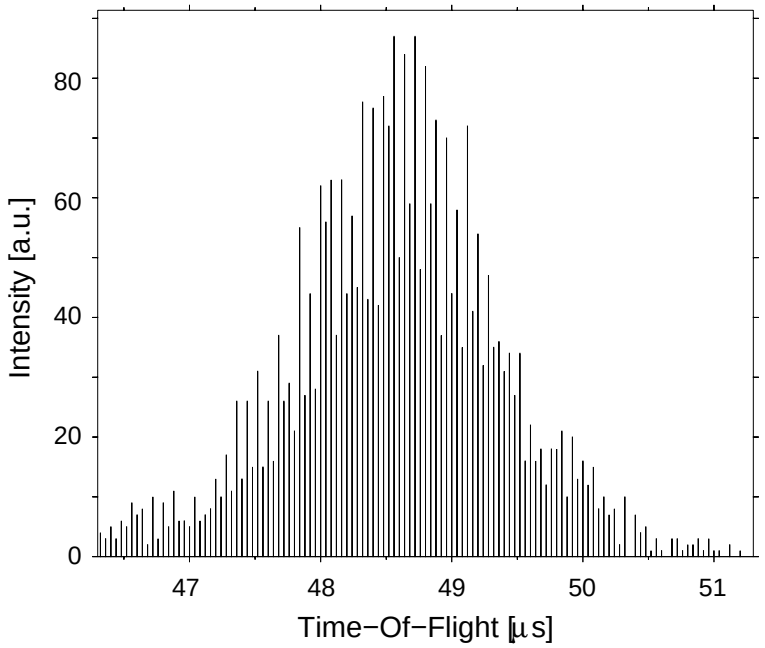

Figure 6.4: Time-of-flight distribution of detector *CH425D1*.

pulses from bad events only two cuts had to be applied to the achieved ensemble of events. Events with an amplitude of more than $\sim 8\,\mathrm{V}$ were discarded. Reasonable signal amplitudes are well below this cut-off. Events for which the analysis program returns a higher amplitude are disturbed by resets of the SQUID circuit ($\sim 10\,\mathrm{V}$), or indicate an error during data analysis. For displaying any other than two-dimensional energy vs. m/z plots (see next section) an amplitude threshold, usually between $0.2\,\mathrm{V}$–$0.3\,\mathrm{V}$ was applied. Below this voltage the mis-interpretation of noise by the analysis program drastically increased as can clearly be seen in the plots in the following section. If not otherwise mentioned, these are the only two cuts applied to all other spectra presented in this chapter.

For the measurement of figure 6.2 about 3500 detector impacts were extracted and are shown. The rise times of the recorded gold pulses are distributed around $2.0\,\mu\mathrm{s}$. For the same ensemble of recorded events a spectrum of the total time-of-flight is plotted in figure 6.3. It shows one dominant peak at $48.8\,\mu\mathrm{s}$ time-of-flight which corresponds to the mass of 197 Da of the gold atoms. A small peak is located at a time-of-flight of $37\,\mu\mathrm{s}$, its origin is unclear.

To investigate the time resolution of detector *CH425D1*, a window of $5\,\mu\mathrm{s}$ width around the gold peak of figure 6.3 is scaled up and shown in figure 6.4. About 3000 events appear in the displayed time-of-flight window centred at $48.8\,\mu\mathrm{s}$. The time-of-flight peak has a width FWHM of $\Delta t = 1.7\,\mu\mathrm{s}$. This represents the absolute time resolution of detector *CH425D1*.

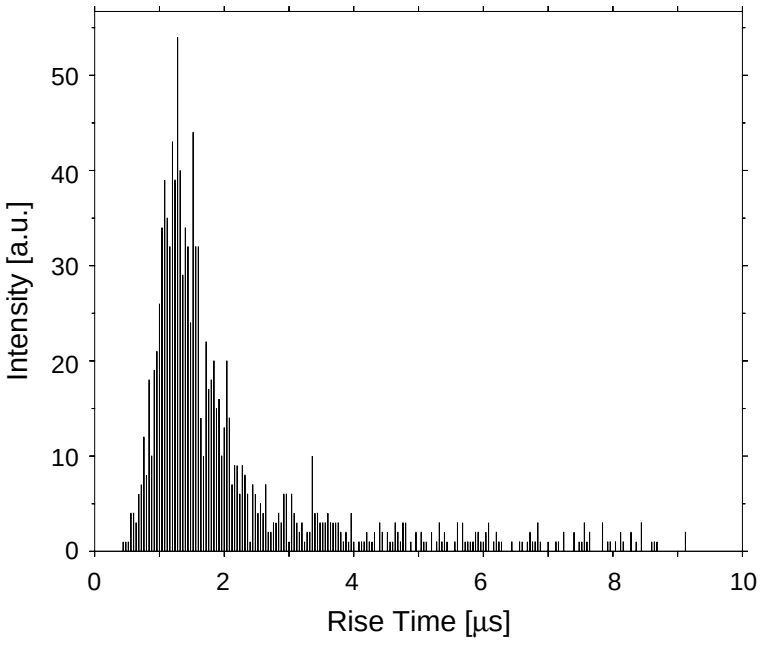

Figure 6.5: Rise time spectrum of detector *CH425C1*. It represents the fastest rise times measured with the detectors developed in this work.

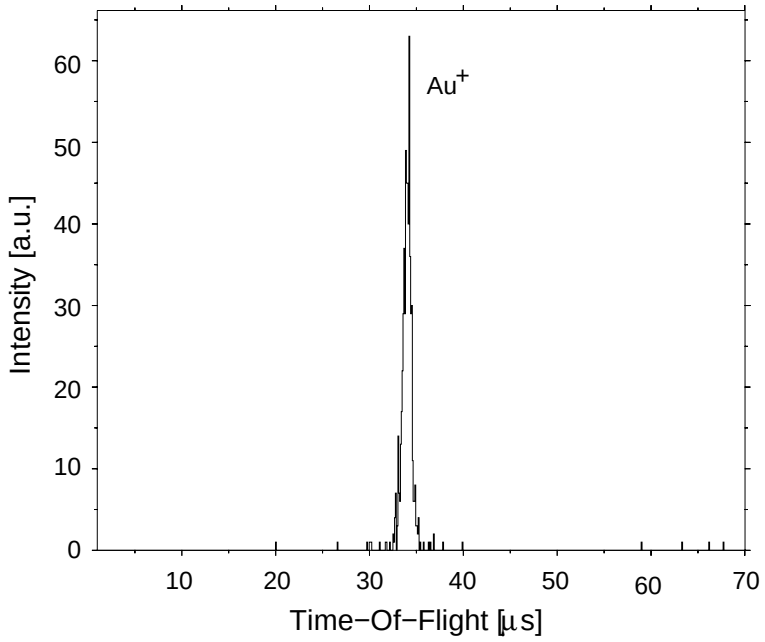

Figure 6.6: Time-of-flight pectrum of gold atoms recorded with detector *CH425C1*.

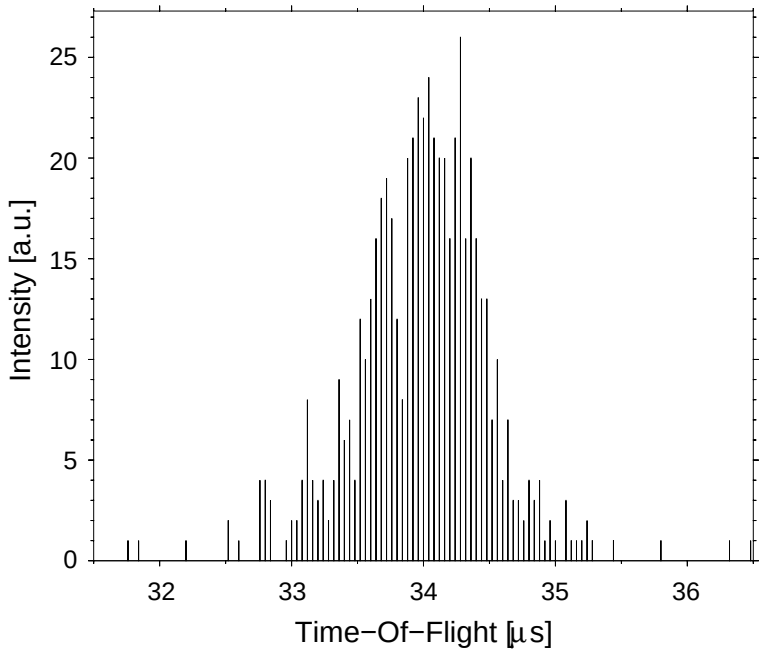

Figure 6.7: Time-of-flight distribution of detector *CH425C1*. The time resolution is slightly better than that of detector *CH425D1*

A slightly better result is shown in the figures 6.5 – 6.7 for detector *CH425C1*. There the signal rise time lies at around 1.3 μs, figure 6.5, and the time resolution at about $\Delta t = 1.1\,\mu$s, figure 6.7. Figure 6.7 is scaled to the same width of 5 μs as figure 6.4 above. The total time-of-flight of the gold atoms of 34.0 μs (figure 6.6) differs from the time-of-flight shown before by a factor of $\sqrt{2}$ as the measurement was done with twice the acceleration voltage (18 keV) as the measurement before.

During the off-line analysis of this measurement run with gold atoms it turned out that in many detected events the SQUID electronic had lost one or more flux quanta Φ_0. This was not obvious at the supervision of the measurement but turned out after signal analysis. The analysis program allows to plot the events versus a parameter called "right-minus-left baseline", which represent the difference between the rightmost and the leftmost recorded data point in an event window. With this parameter one could clearly distinguish bands of events at which the SQUID lost flux quanta, due to the difference of 1.27 V between the bands, which represents one Φ_0. For the spectra shown here all events with flux loss were discarded.

The achieved detector rise times are a satisfying result, the absolute time resolution is still reduced compared to the target value of 0.1 μs, however. This is well-founded in the unexpectedly poor signal-to-noise ratio of the detector pulses[3]. A noise level in the order of $10 - 100\,\mathrm{pA}/\sqrt{\mathrm{Hz}}$ was expected for this type of detectors from other experiments [Ang02, Ben03], whereas noise of up to $1000\,\mathrm{pA}/\sqrt{\mathrm{Hz}}$ was measured here. The source of this ancillary noise is still under investigation. Assuming ten times less noise, the aimed time resolution could be reached.

The influence of the signal-to-noise ratio on the time resolution was confirmed by a short simulation. Different noise signals without any detector pulses on them were recorded and a single pulse, designed after the theoretical model of sec. 2.2.1, was added to the noise. These signals were then treated by the usual pulse-shape analysis. Adding pulses to the noise with an amplitude providing the same signal-to-noise ratio as in the above measurements lead to the same time resolution as achieved in the measurement. Adding pulses with a ten times higher amplitude also lead to an almost ten times better time resolution in the simulation. This result in addition shows that other components in signal treatment, especially the onset-time determination of the pulse-shape analysis, are working satisfactorily and are not the reason of the reduced time resolution.

By comparing the measurements of the two detectors *CH425D1* (Au absorber frames) and *CH425C1* ($3 \times 3\,\mathrm{mm}^2$ full-film), it turned out that the structure, size

[3] A signal rise up to certain signal height U, with a steepness $\eta = \frac{dt}{dU}$, will persist for a time $t = \eta \cdot U$, where t may be identified with a time t_{max} when a voltage U_{max} is reached or an exponential rise time τ_{rise} since they all only differ by a factor close to 1. The same is valid for the error propagation of a voltage noise of amplitude ΔU, $\Delta t = \frac{dt}{dU}\Delta U = \eta \cdot \Delta U$, and thus the signal-to-noise ration S/N becomes $\frac{S}{N} \equiv \frac{U}{\Delta U} = \frac{U \cdot \eta}{\Delta U \cdot \eta} = \frac{n\tau_{rise}}{\Delta t}$, and the time uncertainty Δt caused by the voltage noise is $\Delta t = \frac{n\tau_{rise}}{S/N}$.

and mode of operation (SPT or substrate absorber) of the thermometer film of course affects the signal rise time but the effect is not substantial. Even the most simple approach of detector *CH425C1* with a $3 \times 3 \times 0.5\,\mathrm{mm}^3$ substrate fully covered with a thermometer film, lead to the fastest detector signal of all made measurements.

6.3 Energy Resolution

An advantage of the cryogenic calorimeters compared to conventional detectors is that besides the time of flight they additionally provide energy information. While the time-of-flight measurement only allows the measurement of the m/z value the molecule had at the moment when it left the MALDI source, the amplitude of the calorimeter signal is a measure for the true impact energy of the particle detected. This enables one to distinguish different charge states, masses and fragmentations.

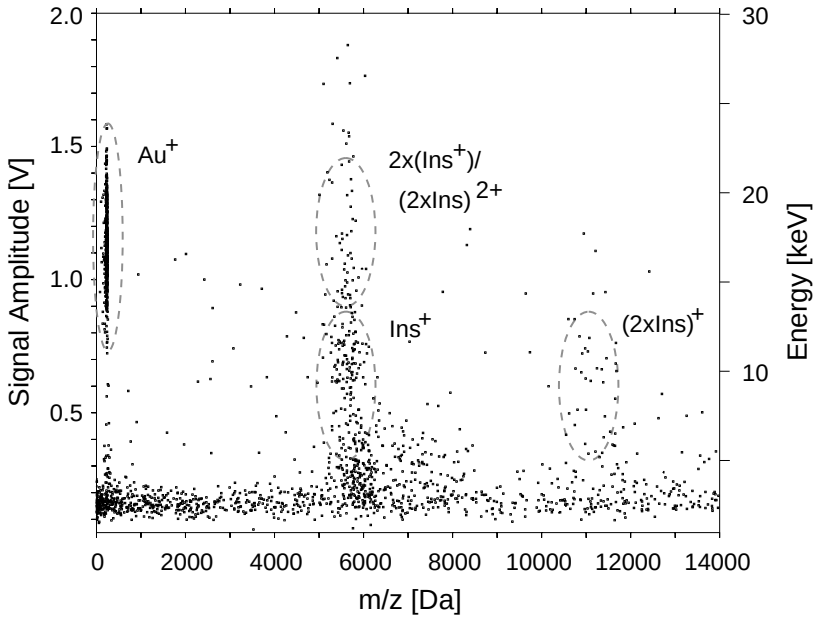

Figure 6.8: 2D scatter plot of detector impact energy vs. ion m/z of gold atoms and insulin molecules. The left ordinate is amplitude of SQUID output, the right ordinate is energy scaled by an X-ray calibrating source.

Figure 6.8 displays a scatter plot of the peak amplitude of the detector signal versus the molecule m/z, measured by time-of-flight, for a measurement with insulin molecules and gold ions, done with detector *CH425C1*. Each dot represents one detected event. The gold peak of this measurement was investigated in sec. 6.2 for measuring the time resolution. As already mentioned, a lot of

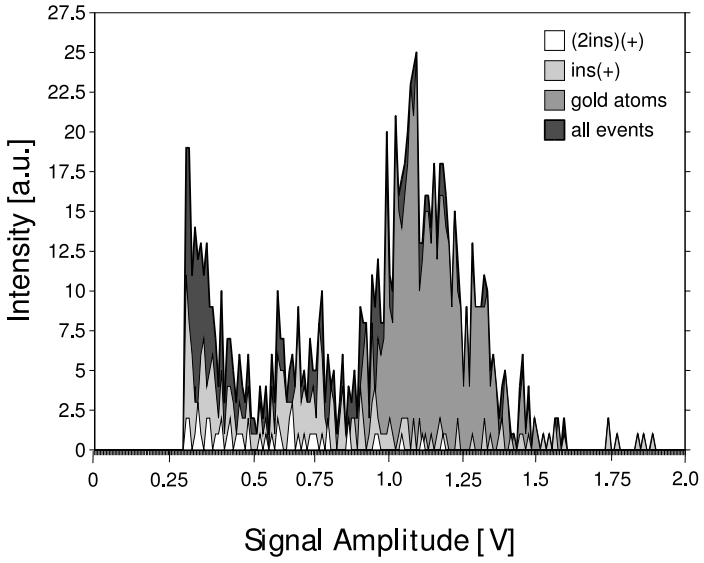

Figure 6.9: Detector amplitude spectrum. The amplitude of the $(\text{insulin})^+$ and $(2 \times \text{insulin})^+$ ion (white and light grey) signals is reduced compared to the amplitude of the gold ions (dark grey). The black curve shows the total spectrum over all recorded events.

noise is visible in the plot at signal amplitudes below 0.3 V. Thus, when plotting one-dimensional spectra usually an amplitude threshold was set to remove these events.

The m/z scaling of the abscissa was applied heuristically. $(\text{Insulin})^+$ions were identified at a time-of-flight of $t = 166\,\mu$s and the abscissa was scaled to the mass of insulin of 5734 Da by $m[\text{Da}] = 0.2081 \cdot t[\mu\text{s}]^2$. It is a common approach to calibrate TOF-MS by the time-of-flight of calibration molecules of known masses. The time-of-flight calculated by the geometry of a TOF-MS always is afflicted with a too large uncertainty. It only holds as a clue for a first identification of the calibration molecules.

The energy axis at the right ordinate was scaled by a measurement of the 5.9 keV X-ray line of a ^{55}Fe source. This line could be measured with an energy resolution $E/\Delta E_{FWHM} \approx 2.7$, which indicates that the energy resolution of the detector is sufficient to distinguish ions in different charge states. The amplitude scale at the left ordinate is volts output voltage of the SQUID electronics. It represents the SQUID current signal in microamperes as $1.27\,\text{V} \widehat{=} 1\Phi_0 \widehat{=} 0.204\,\mu\text{A}$.

The acceleration voltage used for the shown measurement was 18 keV. The gold ions at $m/z = 197$ Da are located in the scatter plot around 18 keV impact energy, compatible with the calibration of the energy scale by the ^{55}Fe X-ray source. The singly charged $(\text{insulin})^+$ ions are located at a lower impact energy

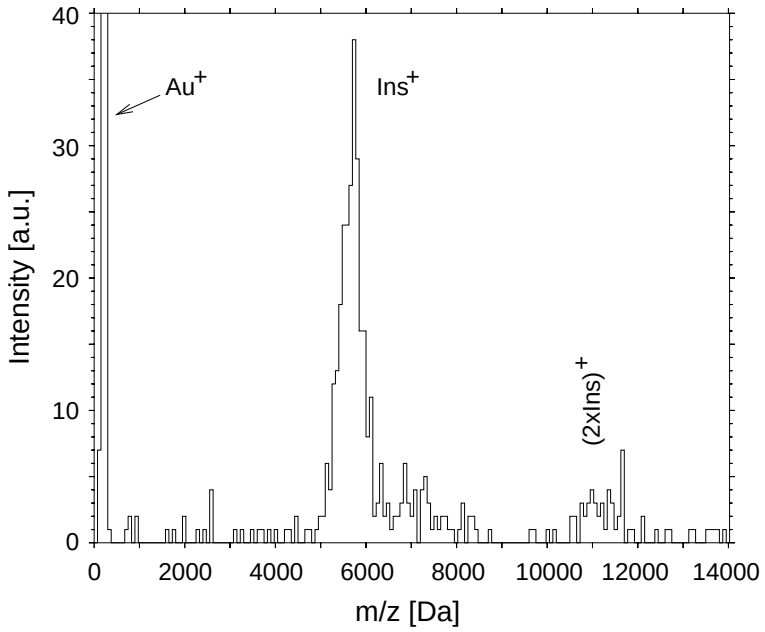

Figure 6.10: Ion m/z spectrum of insulin and gold atoms.

around $\sim$ 12 keV. This loss of impact energy with increasing molecule mass is in agreement with observations of [Rab01] or [Hil98]. At 11.5 kDa singly charged dimers $(2 \times \text{insulin})^+$ were detected with also reduced impact energy. The tail to higher impact energies at the $(\text{insulin})^+$ cloud may indicate the simultaneous arrival of two or more $(\text{insulin})^+$ ions at the same laser shot or, rarely, even doubly charged dimers $(2 \times \text{insulin})^{2+}$.

The energy loss of the insulin molecules is also shown in figure 6.9. It shows the amplitude of all recorded impact events (black curve), events in a window around the gold ion mass (dark grey) and events in windows around the insulin$^+$(light grey) and $(2 \times \text{insulin})^+$ (white curve). Again it can be seen that the gold ions appear with their full acceleration energy at a signal height of $\sim$ 1.2 V whereas the insulin ions appear with a reduced impact energy.

Finally the discussed measurement is presented in a conventional m/z spectrum in figure 6.10. The $(\text{insulin})^+$, $(2 \times \text{insulin})^+$ and $(\text{gold})^+$ peaks are labelled. Since the number of detected events per unit m/z is usually quite low, neighbouring m/z values were added up (binned) making the spectrum look like having a low mass resolution. The peaks of the insulin ions are broader than this binning, thus their mass resolution is not affected.

Also the presence of doubly charged ions at twice the acceleration energy has been demonstrated. Their appearance in MALDI mass spectra strongly depends on the conditions in the ion source. Initially, the ions are multiply charged but loose excess charges by processes like electron capture. Neutrals, singly charged and multiply charged ions remain with a certain distribution, the maximum of

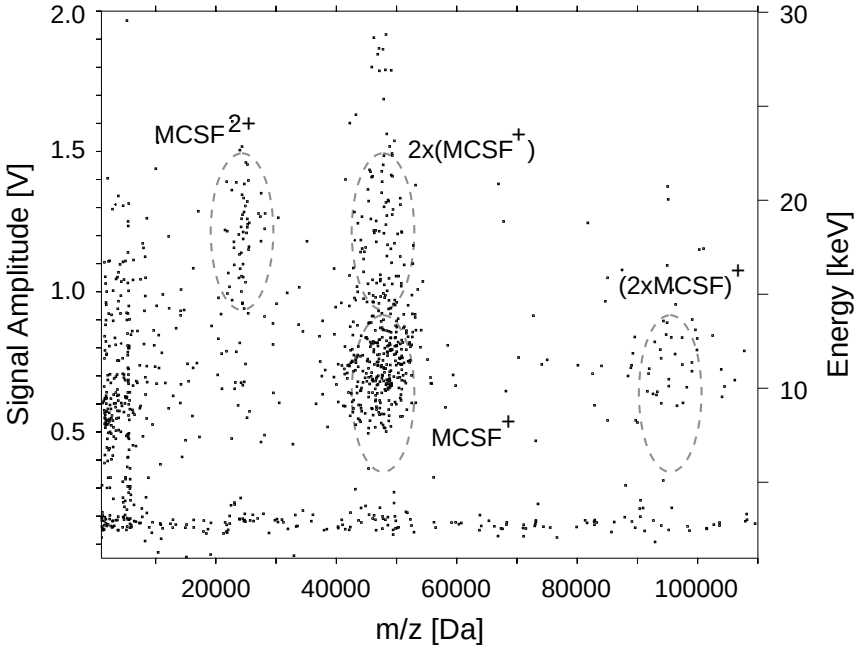

Figure 6.11: 2D scatter plot of detector impact energy vs. ion m/z of protein MCSF.

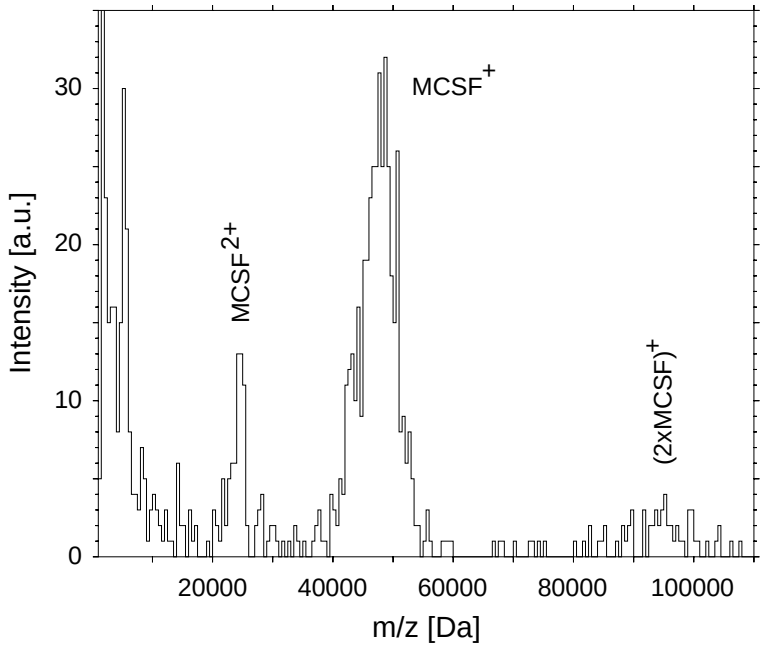

Figure 6.12: Ion m/z spectrum of protein MCSF.

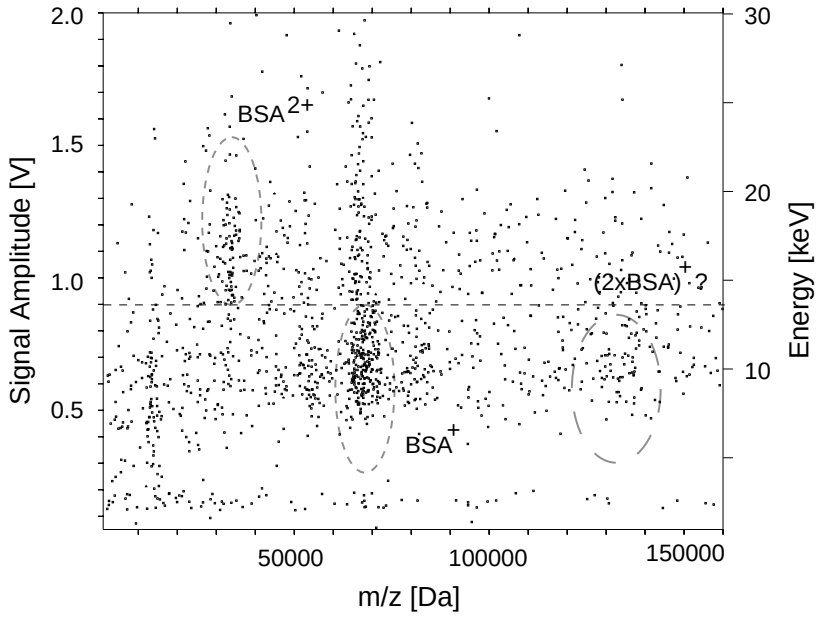

Figure 6.13: Detector impact energy vs. ion m/z of protein BSA.

which is located between neutrals and singly charged ions. The intensity of the signal of multiply charged ions in the mass spectrum varies with the sample preparation and the laser power [Kar00].

Figure 6.11 displays the 2D plotted m/z spectrum of protein MCSF (Macrophage Colony-Stimulating Factor)[4]. Its energy axis is scaled equivalently to that of figure 6.8. It again shows the ions $MCSF^+$and $(2 \times MCSF)^+$ at identical, but compared to the gold atoms reduced impact energy, and simultaneous impacts of two ($MCSF^+$) at twice the single impact energy. In addition doubly charged ions $(MCSF)^{2+}$ are present in the spectrum at half the m/z value, and the impact energy indicates that the ion $(MCSF)^{2+}$ carries twice the energy of the singly charged ion. The plume of events at low masses are some sort of fragmentation noise, while the events at 0.2 V pulse amplitude are noise triggers. Figure 6.12 shows the conventional m/z spectrum of this measurement of protein MCSF, with the distinct peaks labelled.

6.4 Other Protein Measurements

A 2D scatter plot of a measurement of the protein BSA is shown in figure 6.13. The clouds of the singly charged ion $(BSA)^+$ and doubly charged ion $(BSA)^{2+}$ are clearly visible. A cloud of $(2 \times BSA)^+$ at 132 kDa may be visible as well, though

[4] An especially purified sample of protein MCSF was provided by the Proteom Centre Rostock, Germany.

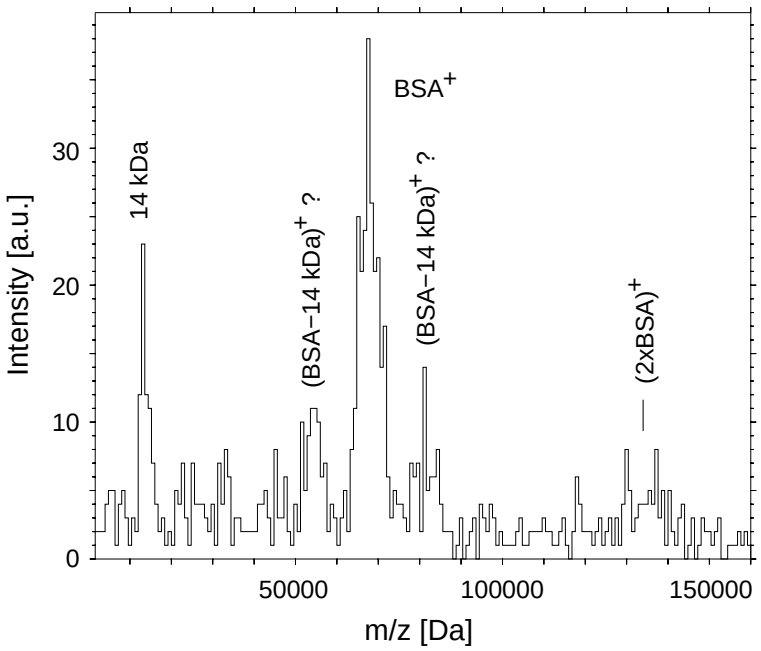

Figure 6.14: Ion m/z spectrum of BSA. Events with an amplitude $< 0.9\,\mathrm{V}$ were selected. The spectrum shows several fragments of the ion $(\mathrm{BSA})^+$ and the dimer $(2 \times \mathrm{BSA})^+$ at 132 kDa.

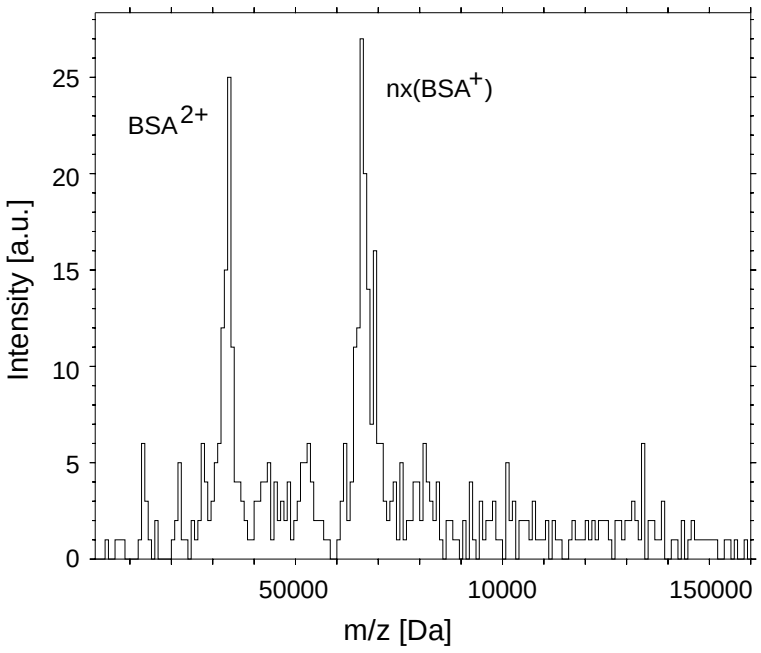

Figure 6.15: Ion m/z spectrum of BSA. Events with an amplitude $> 0.9\,\mathrm{V}$ were selected. The spectrum shows mainly the doubly charged $(\mathrm{BSA})^{2+}$ and the simultaneous detection of multiple $n \times (\mathrm{BSA})^+$.

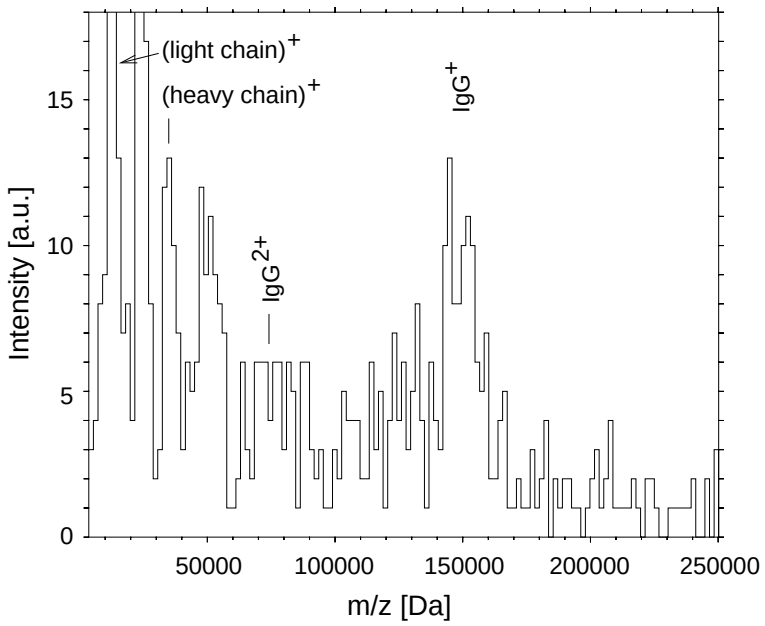

Figure 6.16: Ion m/z spectrum of IgG which was the protein of highest mass measured.

it is not too clear in the scatter noise of the plot.Since the ion yield per laser shot was quite low for this measurement, a higher number of laser shots has been applied. However the signal is of comparable quality as spectra of Human Serum Albumin recorded with cryogenic detectors and published elsewhere [Ben97].

Some of the dots that look like noise are related to a diversity of fragmentations and charge states. This is apparent in the m/z spectrum of BSA. To demonstrate the capability of cryogenic detectors of generating energy sensitive m/z spectra, the data of figure 6.13 is split in two amplitude bands, below and above 0.9 V, corresponding to an energy of 13.5 keV. They are shown in the figures 6.14 and 6.15. The low-energetic m/z spectrum figure 6.14 shows the peaks of the singly charged ions $(\mathrm{BSA})^+$, two fragments of BSA of $(14\,\mathrm{kDa})^+$ and $(\mathrm{BSA} - 14\,\mathrm{kDa})^+$, and a compound at $(\mathrm{BSA} + 14\,\mathrm{kDa})^+$. The dimer $(2 \times \mathrm{BSA})^+$ is much clearer now. The high-energetic m/z spectrum figure 6.15 shows the detection of the doubly charged $(\mathrm{BSA})^{2+}$ and multiple $n \times (\mathrm{BSA})^+$. Other, singly charged molecules are quite suppressed in this spectrum.

The last protein measurement presented is a measurement of IgG with a mass of 150 kDa. It is the heaviest protein measured with our mass spectrometer up to now. The interpretation of the presented spectra is not entirely settled, however they show the capabilities and current limits of our MS.

Figure 6.16 shows the measured m/z spectrum of IgG where the statistics is not very good and which looks quite washy. The $(\mathrm{IgG})^+$ peak at 150 kDa is visible, though. This time, the 2D scatter plot of figure 6.17 is probably more instructive.

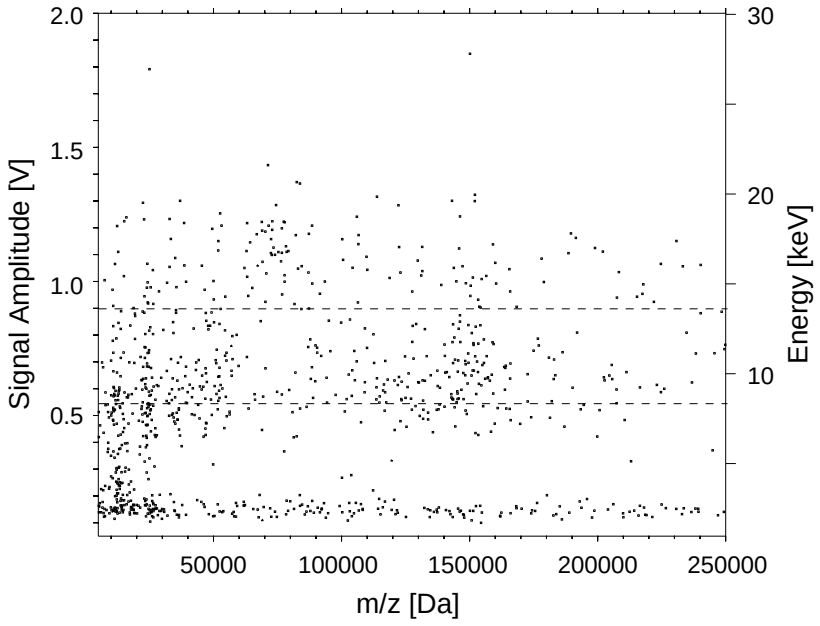

Figure 6.17: 2D scatter plot of IgG. For description, see text

The $(IgG)^+$ ion is visible here as well. Left to it is a cloud of dots which could belong to fragments of $(IgG)^+$. An accumulation of events at $m/z = 75\,kDa$ with twice the energy are likely to be $(IgG)^{2+}$ ion. The peaks at 50 kDa and 25 kDa are related to subunits of the IgG protein. IgG consists of two of these "heavy chains" and "light chains". Below an m/z value of $\sim 50\,kDa$ the background seems to increase. These events are likely to be a diversity of fragments. It was observed during various measurements that, if the main ion peak did not show up clearly, a lot of such fragments appear in the spectrum with the intensity increasing with their decreasing mass. They indicate a destruction of the proband ions during sample preparation or in the MALDI source.

If another cut is applied to the spectrum, also an indication to the presence of the dimer $(2 \times IgG)^+$ can be seen. Selecting an amplitude band between 0.55 V and 0.90 V selects singly charged ions only and removes noise with higher or lower amplitude. An m/z spectrum with an enlarged m/z axis is shown in figure 6.18. In this spectrum an accumulation of events is visible around 300 kDa. It may be related to the $(2 \times IgG)^+$ion. The $(IgG)^+$ peak with its fragments to lower m/z values is clearer than above since the probable $(IgG)^{2+}$ cloud at 75 kDa is removed by the amplitude cut. The $(2 \times IgG)^+$ dimer at 300 kDa would be the protein of highest mass detected with our MS.

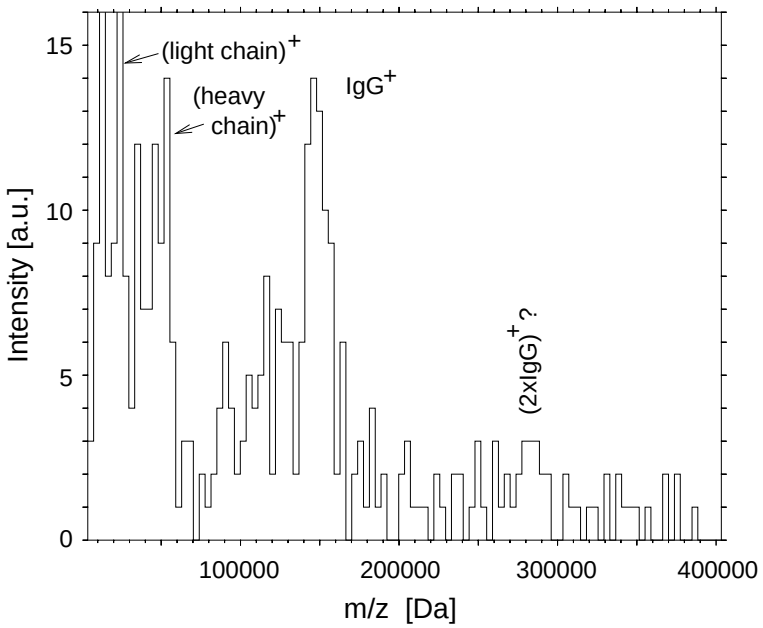

Figure 6.18: Ion m/z spectrum of selected event of the measurement of IgG, with an amplitude between 0.55 V and 0.90 V. The $(\mathrm{IgG})^+$ ion at 150 kDa is clearer now. The accumulation of events at 300 kDa is probably related to the $(2 \times \mathrm{IgG})^+$ ion.

6.5 Measurement of other Heavy Molecules

Proteins are not the only class of macromolecules for which a legitimate interest of obtaining the accurate molecule mass exists. Another big group of macromolecules are polymers. Up to now, TOF-MS is used in this field only for the investigation of monomers and polymers of relatively low molecular weight (several 10 kDa). In this range it can provide information about individual oligomers, repeat units, end groups, and their distribution. With increasing polymer size, conventional TOF-MS becomes more and more questionable due to its decrease of sensitivity. Traditional methods of molecular weight determination for larger polymers are for example gel permeation chromatography (GPC), intrinsic viscometry (IV), membrane osmometry (MO), and laser light scattering (LLS) [Sch96]. In comparison, the main advantage of TOF-MS is a direct measurement of the molecule mass, and a short measurement time.

In this work, some polystyrenes of different molecular weight have been measured to investigate the applicability of the developed MS with cryogenic detector for molecular weight determination of polymers. The polystyrenes were provided by the Max-Planck Institute for Polymer Research in Mainz, Germany.

The preparation of MALDI targets out of polymers widely differs from that of proteins. Almost all polymers need to be cationised since their intrinsic ionisation

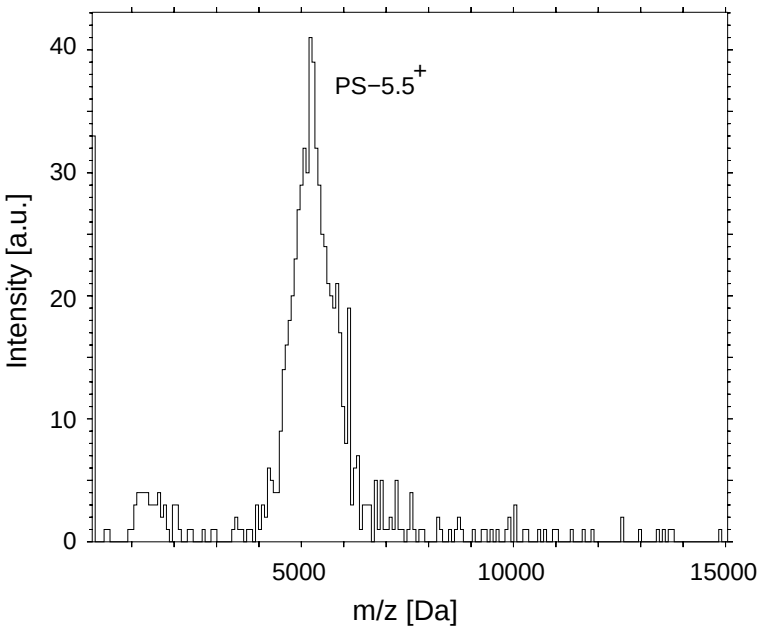

Figure 6.19: m/z spectrum of a light polystyrene.

capabilities are quite poor. This is mainly done by the addition of metal ions, for example Ag^+. Furthermore, the application of the proband on the sample disc is crucial. The development of a thin film and a quick evaporation of the solvent are essential. The procedure of sample preparation used for our measurements follows [Rae02]. Similar procedures are utilised by other groups [Sch96].

Analyte and matrix were dissolved in the solvent tetrahydrofuran (THF). The used matrix was vitamin-A acid (tretinoin). The solutions were mixed in a ratio analyte:matrix according to Table 6.3. Then in THF dissolved silver-trifluoric acetate (CF_3CO_2Ag) was given to the solution, in a molar ratio of 20 parts silver-trifluoric acetate to 1 part analyte. 1 μl of the mixture were pipetted on the sample disc and quickly dried, usually using a heat gun. Quick droplet drying was experienced to improve the quality of the measurement. It is notable that the mixing ratio does not go linearly with molecule weight. With higher molecular weight, the excess of matrix molecules for each analyte molecule needs to be strongly increased.

The smallest polystyrene measured had a mean mass of 5.50 kDa. A measured mass spectrum of it is shown in figure 6.19. Due to the reduced relative mass resolution of the cryogenic detector at low masses, the spectrum shows only one broad peak. Utilising a conventional channel plate detector, it is possible to separate distinct polymer chains with different numbers of monomers [Rae02]. They differ by 105 Da. The peak shown in figure 6.19 represents the envelope of the distribution of these polymers.

Measured mass spectra of a polystyrene of 92 kDa mass and one of 191 kDa

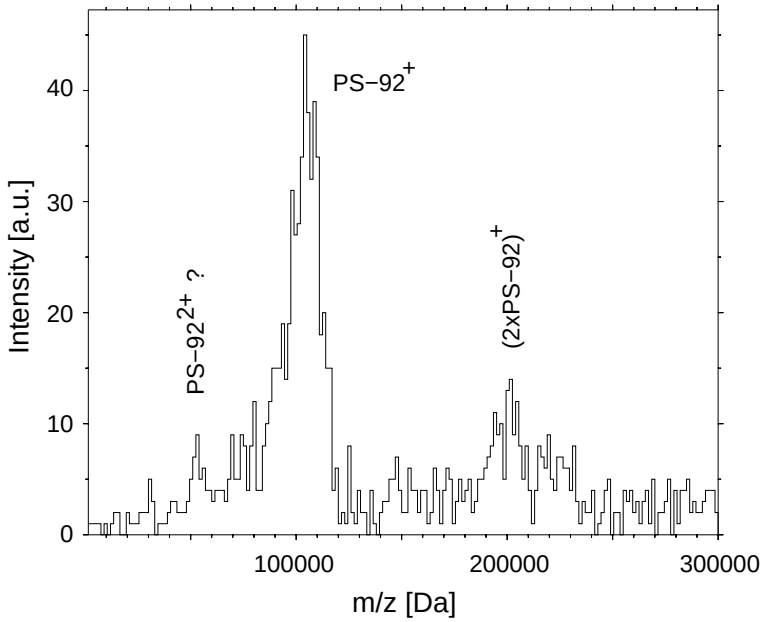

Figure 6.20: m/z spectrum of a polystyrene with a nominal average molecular weight of 92 kDa.

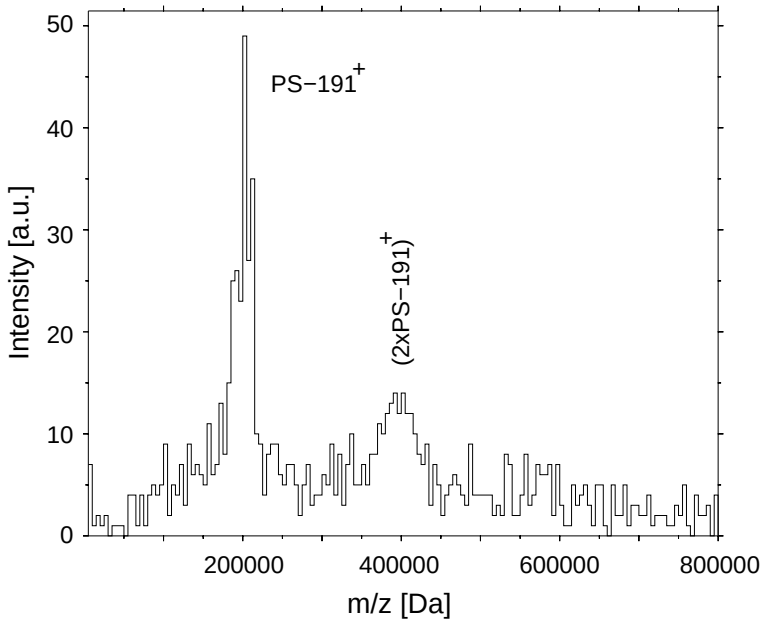

Figure 6.21: m/z spectrum of a polystyrene with a nominal average molecular weight of 191 kDa.

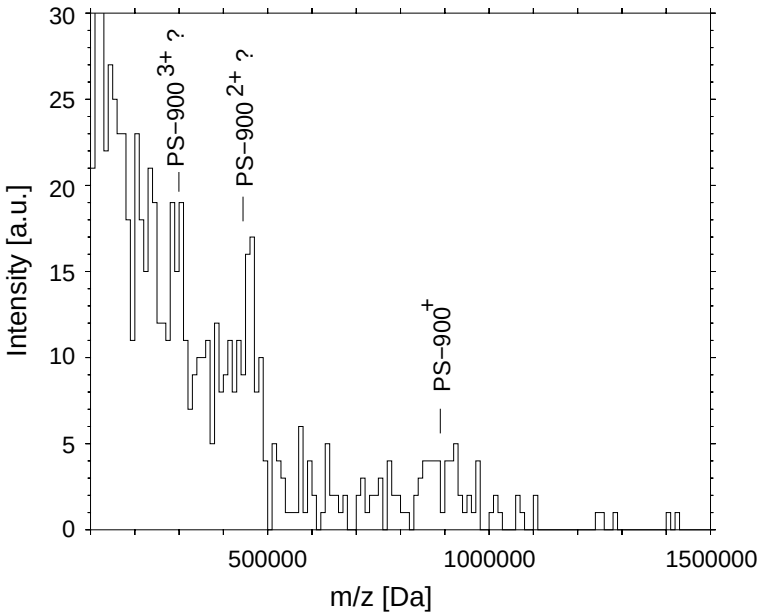

Figure 6.22: m/z spectrum of a polystyrene with an approximate mass of 900 kDa. It is the most massive molecule measured with the TOF-MS with cryogenic detector.

mass are shown in the figures 6.20 and 6.21, respectively. Clearly observable are the $(\text{ion})^+$ peaks. Peaks of the dimers $(2 \times \text{ion})^+$ are also visible, a little bit more clearly for the 92 kDa polystyrene. Figure 6.20 in addition shows a small peak which may be related to the doubly charged polystyrene.

Surprisingly, opposed to other measurements [Sch96, Rae02], no or only weak signals of doubly charged ions are observed. Due to the size of the large molecules it could be reasonable for them to have more than one charge on a molecule. Instead, dimers are observed. The reason for both could eventually be based in the sample preparation. Probably only very few silver ions were built into the polymers. This is supported by the observation that the polymer and the silver-trifluoric acetate on the sample disc start separating immediately. If the sample is not dried very quickly, no silver adducts of the polymer will be present. Thus the chance of multiple ionisation is largely suppressed. On the other hand, probably the sample droplet dried out in too thick a layer with too high a polymer concentration, which assist the formation of dimers.

The polymer with the highest molecular weight currently measured is a polystyrene of approximately 900 kDa mass. Its mass spectrum is shown in figure 6.22.

The spectrum is not as nice as for the lighter polymers, however this polymer is the molecule with the highest mass tested and detected in the developed MS with cryogenic detector. The singly charged $(\text{ion})^+$ is just visible at an m/z value

of 900 kDa. The broad distribution of events below 500 kDa is likely to consist mainly of fragmented molecules. It can as well contain multiply charged ions like $(\text{ion})^{2+}$ (450 kDa) or $(\text{ion})^{3+}$ (300 kDa) as the structure in the distribution may indicate. These have been identified by [Sch96].

Analyte	Mass	Mixing ratio
Polymer 1	5.5 kDa	1 : 200 : 20
Polymer 2	92 kDa	1 : 3500 : 20
Polymer 3	191 kDa	1 : 30000 : 20
Polymer 4	900 kDa	$1 : 10^6 - 10^7 : 20$

Table 6.3: Molar mixing ratios analyte:matrix:cation-agent for the MALDI sample preparation of four measured polystyrenes

6.6 Present Detection Limit

An important characteristic of any mass spectrometer is its detection limit. It is defined as the minimum amount of a proband material which is needed to verify its presence in a sample. Usually it is given in mole. As a first test of the detection limit of the MS with cryogenic detector of this work a dilution test series was carried out with insulin. This protein was chosen because its preparation is uncritical; furthermore it was the primary aim to test the MS setup without the danger of a varying quality of our sample preparation.

Insulin in addition is a quite small ion compared to the mass range which shall predominantly be covered by the developed MS. Thus the measurement can only show a first hint on the general detection limit, and the real limit in the higher mass range will as well be influenced by factors like the focusing properties of the ion optics or the reflection efficiency of the ion mirrors which both may have a certain dependence on the ion mass. On the other hand this is the mass range where the result can be compared with other, commercial MS systems.

For the dilution series, a stock solution with a concentration of 1 pmol/μl insulin was prepared. Since exactly 1 μl of stock solution (together with 2 μl of saturated matrix solution) was applied to the sample disc this corresponds to an amount of the proband of 1 pmol for the first measurement. The achieved mass spectrum is shown in the uppermost left plot of figure 6.23.

The stock solution was then subsequently diluted with solvent reducing the insulin concentration by one order of magnitude in each step. Measurements were taken down to an insulin amount of below 0.1 amol. However the 0.1 amol measurement is the last one shown since insulin could not be identified on the measurements with lower insulin amount.

Figure 6.23 shows a measured dilution series, with the highest insulin amount on top left and the lowest amount on bottom right. The insulin peaks taken

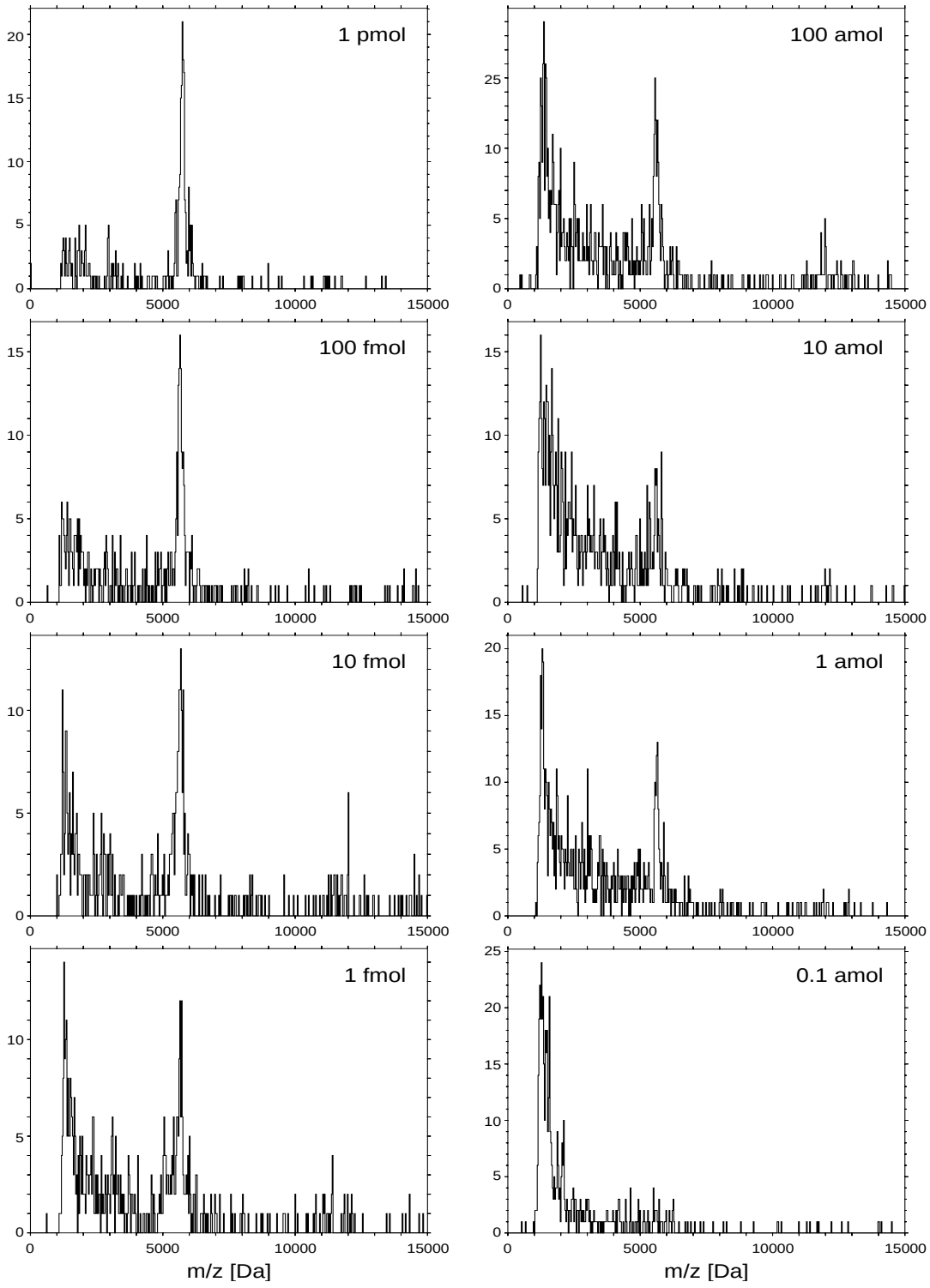

Figure 6.23: Dilution series measurement of insulin. It is clearly proved down to an amount of 1 amol material inserted into the mass spectrometer.

at 1 pmol, 100 fmol and 10 fmol are clearly visible. Although the amount of substance decreases by two orders of magnitudes from the former to the latter measurement, the peak amplitude in the spectra does not change correspondingly. However during the measurements the difficulty of finding "good" spots on the sample increased with decreasing amount of substance. A certain spot has to be found on the sample which shows an insulin signal in a number of subsequent laser shot (so-called "nice spot"). After a number of laser shots onto a certain spot, the insulin signal is not present at each laser shot any more and by and by entirely vanishes. Then a new nice spot needs to be found. When reducing the amount of substance, these nice spots become rarer and harder to find. In addition they do not last for as many laser shots any more and need to be changed more often. In the end, the amplitude of the signal is influenced a lot by the patience of the operator taking the measurement.

The insulin peak of the 1 fmol measurement shows a broadening towards lower masses. This may be due to the loss of some fragments of the insulin ion. The 100 amol measurement shows a clear insulin peak again. The insulin peak in the 10 amol measurement is quite faint. Astoundingly this was also the case in another dilution series taken earlier.

The insulin peak at 1 amol amount of substance is again clearly visible. The signal-to-noise ratio indeed is reduced compared to measurements with a higher amount of substance.

The measurement at an amount of substance of 0.1 amol does not contain a signal which could be assigned to insulin any more. Thus the detection limit of our MS for insulin is at present at an amount of substance of 1 amol. Commercial MS have a detection limit in the range of fmol. This shows that cryogenic detectors are able to enhance the sensitivity of MS significantly.

Chapter 7

Conclusions and Outlook

7.1 Status of the Developed Mass Spectrometer

The project of developing a TOF-MS with a cryogenic detector within the PROTEOM Leitprojekt of the German BMBF is in its fourth year now and is going to be financed for another 1 1/2 years. The TOF-MS, the newly developed cryogenic calorimeter, and an appropriate ADR cryostat providing the operating temperature for the detector, is assembled. The completed setup proved to work reasonably and has undergone initial characterisation.

The major part of the current work was to develop cryogenic detectors such that they are sufficiently fast to be used in TOF-MS. Initially, the parameters that influence the time resolution were characterised. Detectors were designed to be used in the TOF-MS setup. These detectors reached a rise time of down to $\tau_{rise} = 1.3\,\mu$s which is already close to the aimed value of $1.0\,\mu$s. The sensitive detection area is $3.0 \times 3.0\,\mathrm{mm}^2$ while still showing a uniform signal rise over the whole area. The detector is smaller than a conventional MCP detector ($\sim 5\,\mathrm{cm}^2$), however much larger than detectors based on tunnel junctions [Boo97, Twe01, Wes99].

With the TOF-MS, measurements were done determining the time resolution, energy resolution and detection limit of the whole setup. The best time resolution obtained was $\Delta t = 1.1\,\mu$s. This is about ten times worse than estimated due to an unexpected high noise level. The poor signal-to-noise ratio interfered with the determination of the onset time from the detector signals. The energy resolution was measured to be $E/\Delta E = 2.7$, which is sufficiently good to distinguish ions with different charge states.

Different biomolecules with a molecular weight of up to $m = 150\,\mathrm{kDa}$ were measured. In addition, polymers of $m = 900\,\mathrm{kDa}$ could be detected. The detection limit of insulin was determined to be 1 amol.

7.2 Near Future of the Detector Development

The developed cryogenic detectors achieved satisfying and expected properties except for the actual time resolution in the TOF-MS device. The signal rise time is short enough, though, the signal-to-noise ratio still gives room for improvement. The influence of the latter on the time resolution was already proved by a simulation as mentioned in sec. 6.2.

With future detectors the signal amplitude should be increased. For example an SPT film with a relatively steeper transition curve would cause a larger resistance change at a given particle energy. However such a film saturates earlier. The probability for pile-ups to saturate the detector would increase. To find the optimal steepness of the transition curve, many SPT films need to be evaporated, and many detectors need to be characterised. This is a time consuming process, but helps as well to increase the reproducibility of the SPT films.

The limitation of the signal-to-noise ratio is not yet understood. This noise appears in the transition and is dominating. Decreasing this noise would increase the time resolution accordingly. Up to now it was found that this noise is not due to direct illumination of the detector with infrared radiation or hot rest gas atoms from the TOF-MS, since it persists when the detector is shadowed by a closed aperture. A close investigation of this noise needs to be done. The investigation of the noise as well as the increase of the detector signal amplitude is very elaborate.

In sec. 4.6.2 it was already discussed that the L/R time constant of the readout loop might limit the measured rise time of the detector signal. Lowering this time constant would assure that future measurements give the true rise time of the detector. The inductance L is fixed by the SQUID input coil and the cabling. A significant decrease of L would afford an exchange of the SQUID. A low-inductance SQUID sensor has other drawbacks like reduced current sensitivity. To decrease L/R it is more promising to increase R, as for example by engineering the current path in the film. The current path could be made meander-like such that the cross section of the SPT is reduced but its length is increased.

7.3 The TOF-MS in the PROTEOM Network

Improvement and application of the developed TOF-MS with cryogenic detector is continuing within the scope of the PROTEOM Leitprojekt of the German BMBF. As the TOF-MS is running reliably, it should be integrated in real-life measurements of substances provided by other groups of the PROTEOM project. Measurements of proteins, protein clusters and massive cell components like ribosomes line up for the near future.

Through these and other calibration measurements, the characterisation of the TOF-MS setup will continue. It is an enduring task to specify and improve

properties like mass resolution, charge state separation or mass separation. The latter for example may be tested by measuring mixtures of different proteins. In such measurements the properties in question are the mass separation as well as the continuous reproducibility of the ratio of concentration of different proteins in one sample.

The measurement of the barely visible polystyrene #4 with a mass of 900 kDa (figure 6.22) showed a high fragmentation. This indicates problems during sample preparation or in the MALDI source. Further improvements of the TOF-MS setup, the sample preparation, and more experience in the operation of the ion source may help solving these problems. Heavy polymers and proteins provided by other groups, could be used as test samples. Up to now the mass limit of our TOF-MS setup itself seems not to be reached yet. The range of accessible molecule masses may still be expanded.

Appendix A

Measuring the SPT Film Resistance at its Operating Point

A transition curve is usually recorded with every cryogenic calorimeter to characterise the superconducting film. For this, the measurement current is switched from $+I_{tot}$ to $-I_{tot}$ and the resulting change ΔU_{SQUID} of the SQUID output is recorded. The resistance of the SPT film is given by

$$R_{Film} = R_{Shunt}\frac{I_S}{I_{tot} - I_S}\,. \tag{A.1}$$

$I_S = \frac{1}{2}\Delta U_{SQUID}\cdot(\delta I/\delta\Phi)/(\delta U/\delta\Phi)$ calculates from the SQUID output signal. By sweeping the temperature of the SPT, its transition curve $R_{Film}(T)|_{I_{tot}}$ can be measured.

This works well until the SQUID output voltage exceeds the maximum voltage of the amplifier electronics which is usually 10 V. Then the electronic will reset. For our detectors the measurement current I_{tot} in usual detector operation is that high that it is not possible to record the transition curve $R_{Film}(T)|_{I_{tot}}$. This means that with the mentioned method it is only possible to observe the transition curve for much lower current but not under real operating conditions.

Nevertheless $R_{Film}(T)|_{I_{tot}}$ can be measured at a distinct operating temperature T and current I_{tot}. To do so, a very slow triangular curve of ~ 0.05 Hz is applied to the current source, with an amplitude which corresponds to a current I_{tot}. So the measurement current is continuously sweeped to its maximum value and back to its negative maximum value. During this, the current through the SQUID branch of the readout circuit is sweeped as well. As the current is much too high for the SQUID amplifier, the SQUID output voltage will increase, following the measurement current, until it reaches its limit at 10 V, and then reset and restart at 0 V.

So the total SQUID output voltage can be added up by counting the number of resets within one half-period of the triangular curve with a digital oscilloscope. Then the SPT film resistance is calculated as usual. The uncertainty in this crude

method lies in the fact that the last, incomplete step may only be read from the oscilloscope screen as a coarse fragment of the total voltage of 10 V.

Bibliography

[Alt97] M. Altmann et al., *Proceedings of the* 4^{th} *International conference on Solar Neutrinos*, Heidelberg (1997), ed. W. Hampel, ISBN 3-00-002064-0 (1997), 183

[And81] A. C. Anderson, *Nonequilibrium Superconductivity, Phonons and Kapitza Boundaries,* ed. K. E. Gray, Plenum New York (1981)

[Ang01] G. Angloher el al., in [LTD01] 227-230

[Ang02] G. Angloher et al., *Astroparticle Physics* 18 (2002) 43-55

[Ash76] N. Ashcroft, D. Mermin; *Solid State Physics,* Saunders (1976), ISBN 0-03-049346-3

[Bar97] D. C. Barbacci et al., *Int. J. Mass Spectrom. Ion Proc.* 165/166 (1997) 221-235

[Bar57] J. Bardeen, et al., *Phys. Rev.* 108 (1957) 1175-1204

[Ben97] W. H. Benner et al., *J. Am. Soc. Mass Spectrom.* 8 (1997) 1094-1102

[Ben03] A. Bento, *PhD thesis*, University of Oxford, (2003)

[Ber01] W. M. Bergmann Tiest et al., in [LTD01] 199-202

[Ber97] S. Berkenkamp et al., *Rapid Comm. Mass Spectrom.* 11 (1997) 1399-1406

[Boo97] N. E. Booth, *Rapid Comm. Mass Spectrom.* 11 (1997) 171-174

[Bro00] K. Brown, The human genome business today, K. Howard, The bioinformatics gold rush, C. Ezzell, Beyond the human genome, *Scientific American* July (2000) 40-57

[Bru93] M. Bruckmayer et al., *The CRESST Dark Matter Search Proposal to the Gran Sasso Laboratory*, Publication of the German Max-Planck Society MPI-PhE/93-29, Munich, (1993)

[Boe92] U. Boesl et al., *Int. J. Mass Spectrom. Ion Proc.* 112 (1992) 121-166

[Bru99] M. Bruckmayer*, PhD Thesis*, University of Oxford (1999) 27-32

[Bru00] M. Bruckmayer et al., *Physica B* 284-288 (2000) 1998-1999

[Cab96] B. Cabrera, *Nucl. Instr. Meth. A* 370 (1996) 150-156

[Cab98] B. Cabrera et al., *App. Phys. Lett.* 73 (1998) 735-737

[Cho00] D. T. Chow et al., *Nucl. Instr. Meth. A* 444 (2000), 196-200

[Cor56] W. S. Corak, C. B. Satterthwaite, *Phys. Rev.* 102 (1956), 662-666

[Deb12] P. Debye, *Ann. Phys.* 39 (1912) 789

[Dor90] A. VanDorsselaer et al., *Biomed. Environ. Mass Spectrom.* 19 (1990) 692-704

[Eck97] C. Eckerskorn et al., *Anal. Chem.* 69 (1997) 2888-2892

[Fis36] J. Fischer, *Einführung in die klassische Elektrodynamik*, Julius Springer Verlag Berlin (1936)

[Fra93] M. Frank; *PhD Thesis*, TU-München (1993)

[Fra94] M. Frank et al., *Nucl. Instr. Meth. A* 345 (1994) 367-378

[Fra99] M. Frank et al., *Mass Spectrom. Rev.* 18 (1999) 155-186

[Fra00] M. Frank, *Nucl. Instr. Meth. A* 444 (2000) 375-384

[Fra97] J. Franzen, *Int. J. Mass Spectrom. Ion Proc.* 164 (1997) 19-34

[Fuc-38] K. Fuchs, *Proc. Cambridge Phil. Soc.* 34 (1938) 100-108

[Fue95] S. D. Fürstenau, W. H. Benner, *Rapid Comm. Mass Spectr*om. 9 (1995) 1428-1538

[Ger00] G. Gervasio et al., *Nucl. Instr. Meth. A* 444 (2000) 389-394

[Glo00] M. Glocker, M. Bantscheff, Proteome Center Rostock, private note (2000)

[Gou84] P. Goupillaud et al., *Geoexploration* 23 (1984/85) 85-102

[Gup99] D. Gupta, A. M. Kadin, *IEEE Trans. Appl. Supercond.* 9 (1999), 4487-4490

[Hil98] G. C. Hilton et al., *Nature* 391 (1998) 672-675

[Hoe98] J. Höhne, *PhD Thesis*, TU-München (1998)

[IHG01] International Human Genome Sqeuencing Consortium, *Nature* 409, 860 - 921 (2001)

[Irw96] K. D. Irwin et al., *Nucl. Instr. Meth. A* 370 (1996) 177-179

[Irw98] K. Irwin et al., *J. App. Phy.* 83 (1998) 8, 3978-3985

[Jul97] A. Juillard et al., *Proceedings of the* 7^{th} *International Workshop on Low Temperature Detectors (LTD-7),* ed. S. Cooper, Publication of the Max-Planck-Institute of Physics, Munich (1997), ISBN 3-00-00226-X, 137

[Kad96] A. M. Kadin, M. W. Johnson, *App. Phys. Lett.* 69 (1996) 3938-3940

[Kai94] G. Kaiser, A friendly guide to wavelets, Birkhäuser, Boston (1994) ISBN 3-7643-3711-7

[Kar87] M. Karas et al., *Int. J. Mass Spectrom. Ion Proc.* 78 (1987) 53-68

[Kar88] M. Karas, F. Hillenkamp, *Anal. Chem.* 60 (1988) 2299-2301

[Kar89a] M. Karas et al., *Int. J. Mass Spectrom. Ion Proc.* 92 (1989) 231-242

[Kar89b] M. Karas et al., *Angew. Chem.* 101 (1989) 805-806

[Kar89c] M. Karas et al., *Biomed. Env. Mass Spectrom.* 18, (1989) 841-843

[Kar00] M. Karas et al., *J. Mass Spectrom.* 35 (2000) 1-12

[Kar72] V. I. Karataev et al., *Sov. Phys. - Technical Physics,* 16 (1972) 1177-1179

[Kaz86] D. V. Kazakovtsev, Y. B. Levinson, *Phys. Stat. Sol. (b)* 136 (1986) 425

[Kit80] C. Kittel, Einführung in die Festkörperphysik 5. Auflage, R. Oldenburg Verlag München (1980), ISBN 3-486-32765-8, p. 190

[Leh96] W. D. Lehmann, Massenspektrometrie in der Biochemie, Spektrum Verlag Heidelberg (1996), ISBN 3-86025-094-9

[LTD01] F. S. Porteret al., *Low Temperature Detectors* 9, Proceedings of the 9^{th} international workshop on low temperature detectors, Madison, Wisconsin 2001, AIP Proceedings New York (2001) ISBN 0-7354-0049-0

[Mam73] B. A. Mamyrin et al., *Sov. Phys. - JEPT,* 37 (1973) 45-48

[Mar90] H. J. Maris, *Phys. Rev. B* 41 (1990) 9736

[Mas95] Yu. Maslennikov et al., *IEEE Trans. App. Supercond.* 5 (1995) 3241-3243

[Maw01] Y. Mawatari, J. R. Clem, *Phys. Rev. Lett.* 86 (2001) 2870-2873

[Max54] J. C. Maxwell, A Treatise on Electricity and Magnetism, 3^{rd} edition, reprinted by Dover, New York (1954), Vol. 1, p. 440

[Men99] C. Menzel et al., *Rapid Comm. Mass Spectrom.* 13 (1999) 26-32

[Moo81] M. V. Moody, J. L. Paterson, *Phys. Rev. B* 23 (1981) 133-142

[Nag94] U. Nagel et al., *J. Appl. Phys.* 76 (1994) 4262

[Nav01] X-F. Navick et al., in [LTD01] 489-492

[Per01] T. A. Perera et al., in [LTD01] 485-488

[Pip55] A. Pippard, *Phil. Mag.* 46 (1955) 1104

[Pob96] F. Pobell, Matter and Methods at Low Temperatures 2^{nd} edition, Springer-Verlag Berlin Heidelberg New-York (1996), ISBN 3-540-58572-9

[Por01] F. S. Porter et al., in [LTD01] 421-424

[Pre00] "President Clinton announces the completion of the first survey of the entire human genome", U. S. White House press release, 25 June (2002)

[Pro95] F. Pröbst et al., *J. Low Temp. Phys.* 100 Nos. 1/2 (1995) 69ff

[Rab01] M. W. Rabin et al., *J. Am. Soc. Mass Spectrom.* 12 (2001) 826-831

[Rae02] H. J. Räder, K. Martin, private communication, Max-Planck Institute for Polymer Research Mainz, Germany (2002)

[Rho62] E. H. Rhoderick, E. M. Wilson, *Nature* 194 (1962) 1167-1168

[Rou85] M. L. Roukes et al., *Phys. Rev. Lett.* 55 (1985) 422-425

[Sch96] D. C. Schriemer, Liang Li, *Anal. Chem.* 68 (1996) 2721-2725

[Sis97] M. Sisti, et al., *Proceedings of* 7^{th} *International Workshop on Low Temperature Detectors (LTD7),* Munich, Jul 27-Aug 2 (1997), ed.: S. Cooper, F. Pröbst and W. Seidel, MPI Physik Munich (1997), ISBN 3-00-002266-X, 232-236

[Sis99] M. Sistis, *PhD Thesis*, TU-München (1999)

[Sta00] M. Stark, *Master's Thesis*, TU-München (2000)

[Str94] K. Strupat et al., *Anal. Chem.* 66 (1994) 464-470

[Tam95] S. Tamura, *Phys. Rev. B* 31 (1985)

[Tan88] K. Tanaka et al., *Rapid Comm. Mass Spectrom.* 2 (1988), 151-153

[Twe96] D. Twerenbold, *Nucl. Instr. Meth. A* 370 (1996) 253-255

[Twe96a] D. Twerenbold et al., *Appl. Phys. Lett.* 68 (1996) 3503-3505

[Twe01] D. Twerenbold et al., *Proteomics* (2001), 1, 66-69

[Uch98] S. Uchaikin, *J. Phys. IV France* 8 (1998) Pr3-221-Pr3-224

[Uch01] S. Uchaikin et al., *Physica C* 350 (2001) 177-179

[Uch02] S. Uchaikin et al., *Physica C* 367 (2002) 295-297

[Ull00] J. N. Ullom et al., *Nucl. Instr. Meth. A* 444 (2000) 385-388

[Urb89] A. Urban, *PhD Thesis*, TU-München (1989) 32-36

[Wes99] G. Westmacott et al., *48th ASMS Conference June 13-17 Dallas, Texas (1999)*

[Wil55] W. C. Willey, I. H. McLaren, *Rev. Sci. Instr.* 26 (1955) 1150-1157

[Zen98] R. Zenobi, R. Knochenmuss, *Mass Spectrom. Rev.* 17 (1998), 337-366

Acknowledgements

Mein Dank gilt allen, die am Gelingen dieser Arbeit mitgewirkt haben. Besonders erwähnen möchte ich die direkt beteiligten Personen:

Prof. Dr. Norbert Schmitz für die Möglichkeit, meine Doktorarbeit am Max-Planck-Institut für Physik anfertigen zu können.

Dr. Franz Pröbst, immer ansprechbar und bereit, jedes erdenkliche Problem zu lösen. Für sein tiefes Wissen rund um die Tieftemperatur-Physik und unsere Kryodetektoren.

Dr. Wolfgang Seidel, kompetent in allen technischen Fragen, sei es nun ein Kryostat oder ein Auto. Und für seine aufschlussreichen Einblicke in die Vorgänge hinter und neben der Physik.

Dr. Peter Christ für die gute Zusammenarbeit direkt am Projekt. Ohne ihn wäre so manche Messung nicht so schön wie sie jetzt ist. Und für seine Auftritte in diversen Lokalen in der Münchener Soul-Jazz Szene.

Dr. Manfred Bruckmayer für sein Wissen rund um die Tieftemperatur-Physik und seine Einweisung in das Geschäft des "kalt machens".

Die Buam:

Dr. Godehard Angloher für sein unerschöpfliches Wissen, die Helium-Organisation, und die Fähigkeit, neben dem Tagesgeschäft innerhalb weniger Stunden halbe Doktorarbeiten korrektur zu lesen.

Dr. Antonio Carlos Sena Sao Miguel Bento für den Beistand im Büro und für seine zahlreichen sinnvollen, sinnlosen und unsinnigen Diskussionen.

Dr. Torsten Frank unter anderem für das Voraus Gehen auf dem Pfad der Promotion, speziell in puncto Formalia. Er konnte mich vor einigen Stolpersteinen warnen.

Dr. Philippe di Stefano für seine weisen Ratschläge und die angenehmen Unterhaltungen.

Dr. Sergey Uchaikin für seinen unermüdlichen Kampf mit dem achtarmigen Ungeheuer, dem SQUID.

Die Mädels:

Federica Petricca für die Betreuung des Reinraums und für die gute Gesellschaft im Büro.

Jelena Doncev für ihr Wissen um radioaktive Quellen und Verunreinigungen. Auch ihr Dank für die gute Gesellschaft im Büro.

Dr. Cristina Cozzini für ihr Wissen um die Datenauswertung. Und für ihre Geduld mit dem installierten OS auf ihrem Rechner.

Dieter Hauff und Hans Seitz, stets bereit die Probleme des Alltags zu lösen. Würden sie die Anlagen und Kryostaten nicht in Schuss halten, wer weiss ob sie überhaupt noch funktionieren würden.

Dr. Michael Altmann für die immer frischen Informationen aus den höheren Etagen des Instituts. Und für die Erfindung des Ringberg-Seminars.

Die Garchinger:

Michi Stark für die Einweisung ins und die Hilfe beim "Dampfen".

Mike Huber für die gute Unterhaltung und zahlreichen Diskussionen bei E15.

Doreen Wernicke, Garchingerin im weiteren Sinne, für lustige Stunden an der Aufdampfanlage.

Die Rostocker, unter anderen **Dr. Markus Bantscheff, Prof. Dr. Michael Glocker, Dr. Cornelia Koy** und **Prof. Dr. Hans-Jürgen Thiesen** für die tatkräftige und formale Unterstützung.

Ana Dubak, Ringaile Placakyte, Biljana Vujicic und Ludger Janauschek von der H1 Gruppe für die Pausen an der Kaffeemaschine.

Nicht zuletzt gilt mein Dank **meinen Eltern**. Meiner Mutter, die mich immer unterstützt hat, und meinem Vater, der meine Doktorarbeit leider nicht mehr miterleben konnte.